Electromagnetic Fields in MRI

Analytical Methods and Applications

Fuchs, P.S.

DOI
10.4233/uuid:78d96af2-fb96-4a6e-a51e-ea4236fdf2d7

Publication date
2020

Document Version
Final published version

Citation (APA)
Fuchs, P. S. (2020). *Electromagnetic Fields in MRI: Analytical Methods and Applications*. [Dissertation (TU Delft), Delft University of Technology]. https://doi.org/10.4233/uuid:78d96af2-fb96-4a6e-a51e-ea4236fdf2d7

ELECTROMAGNETIC FIELDS IN MRI

Analytical Methods and Applications

Patrick Stefan Fuchs

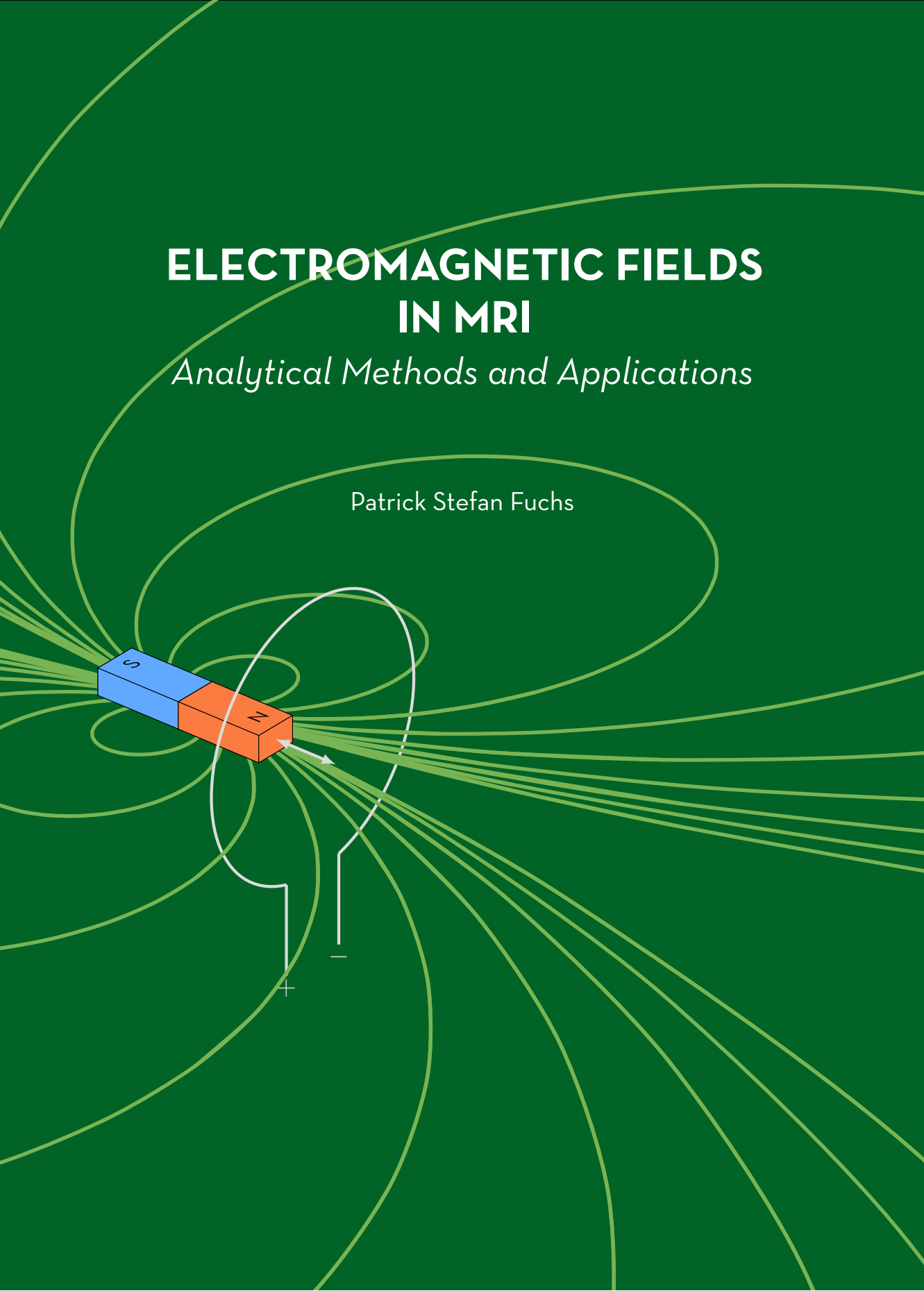

Electromagnetic Fields in MRI

Analytical Methods and Applications

Electromagnetic Fields in MRI

Analytical Methods and Applications

Proefschrift

ter verkrijging van de graad van doctor
aan de Technische Universiteit Delft,
op gezag van de Rector Magnificus prof. dr. ir. T. H. J. J. van der Hagen,
voorzitter van het College voor Promoties,
in het openbaar te verdedigen op
dinsdag 22 december 2020 om 15:00 uur

door

Patrick Stefan FUCHS

Elektrotechnisch Ingenieur, Technische Universiteit Delft, Nederland
geboren te Meyrin, Zwitserland.

Dit proefschrift is goedgekeurd door de promotoren.

promotor: Dr. ir. R. F. Remis
promotor: Prof. dr. ir. G. J. T. Leus
promotor: Prof. dr. K. V. S. Hari

Samenstelling promotiecommissie:

Rector Magnificus,	voorzitter
Dr. ir. R. F. Remis	Technische Universiteit Delft, *promotor*
Prof. dr. ir. G. J. T. Leus	Technische Universiteit Delft, *promotor*
Prof. dr. K. V. S. Hari	Indian Institute of Science, India, *promotor*
Onafhankelijke leden:	
Prof. dr. A. Webb	Technische Universiteit Delft en Leiden Universitair Medisch Centrum
Prof. dr. ir. C. A. T. van den Berg	Universitair Medisch Centrum Utrecht
Prof. dr. ir. M. C. van Beurden	Technische Universiteit Eindhoven
Dr. R. Lattanzi	New York University. U. S. A.
Prof. dr. ir. A. J. van der Veen	Technische Universiteit Delft, *reservelid*

Keywords: MRI, electromagnetism, scattering, electric properties, inversion

Printed by: Ridderprint | www.ridderprint.nl

Front & Back: A magnet and coil combination to illustrate Faradays' law. Inspired by a figure in ch. 7 of Magnetic Resonance Imaging – Physical Principles and Sequecne Design by Brown et. ali. Tikz code adapted from Cyril Langlois "Dipolar Magnetic Field" example by Patrick Fuchs.

ISBN 978-94-6416-342-1

An electronic version of this dissertation is available at the TU Delft online repository https://repository.tudelft.nl/.

Contents

Summary

Electrical properties, the conductivity and permittivity of tissue, are quantities that describe the interaction of an object and electromagnetic fields. These properties influence electromagnetic fields and are influenced themselves by physiological phenomena such as lesions or a stroke. Therefore, they are important in identifying or diagnosing the severity of pathologies, and they are essential in magnetic resonance imaging (MRI) safety and efficiency by determining tissue heating or sensitivity to excitation pulses and antenna designs.

In two-dimensional electromagnetic fields, which occur in specific measurement geometries, it is possible to simplify the relationship between electromagnetic fields and electrical properties, and reconstruct these properties using essentially a forward operation, foregoing a full inversion scheme. These insights also help to find, and explain, the cause of specific artefacts, such as those caused by mismatches in incident field used in the computation of the full electromagnetic fields.

The two-dimensional field assumption necessary for the simplified relationship described above is subsequently tested, and it is shown that this assumption does not hold when the object is sufficiently translation variant in the longitudinal direction. That is, even if the fields for a translation invariant object would be two-dimensional, they become three-dimensional through the interaction of the tissue parameters with the fields, which cause out of plane current and field contributions.

Another interesting application of closed form expressions between currents and fields is the target field method, which solves the inverse source problem between electric currents and static magnetic fields in a regularised manner by constraining their relationship to a cylindrical geometry. This method is adapted for transverse oriented magnetic fields to be used with Halbach type magnet arrays, and an open source tool is developed to make the method easy to apply for various design considerations.

Moving away from constraints on the field or current structure, we show the intricate relationship between electrical properties and the measured signal in an MRI scanner. This is done by deriving the electro- (and magneto-) motive force for a typical MRI scenario without any assumptions on the object or electro-magnetic fields. This model can then even be used to reconstruct electrical properties from the simplest MRI signal, namely the free induced decay (FID) signal.

To round off our investigation of tissue properties we take a small detour to the magnetic tissue property, the permeability or magnetic susceptibility. For reconstructing this tissue property a dipole deconvolution is required, where the dipole convolution loses information of the original object through the zeros of the dipole kernel. A new machine learning based approach to reconstruct the lost information is investigated in the final chapter of this thesis.

Samenvatting

De elektrische eigenschappen, de geleidbaarheid en permittiviteit zijn grootheden die de interactie tussen een object en elektromagnetische velden beschrijven. Ze beïnvloeden elektromagnetische velden, maar worden zelf beïnvloed door fysiologische verschijnselen zoals laesies of een beroerte. Daarom zijn ze belangrijk bij het identificeren of diagnosticeren van de ernst van pathologieën en essentieel voor de veiligheid en efficiëntie van een MRI scan, door het bepalen van weefselverwarming of gevoeligheid voor excitatiepulsen en antenneontwerpen.

In tweedimensionale elektromagnetische velden welke voorkomen in specifieke meetgeometrieën, is het mogelijk om de relatie tussen elektromagnetische velden en elektrische eigenschappen te vereenvoudigen, en deze eigenschappen te reconstrueren met behulp van in wezen een voorwaartse bewerking, waarbij een volledig inversieschema kan worden vermeden. Deze inzichten hebben ook geholpen bij het vinden en verklaren van de oorzaak van specifieke beeld-artefacten in reconstructies, zoals die worden veroorzaakt door fouten in het invallende veld dat wordt gebruikt om de volledige elektromagnetische velden te berekenen.

De tweedimensionale veldaanname die nodig is voor de hierboven beschreven vereenvoudigde relatie wordt op de proef gesteld in het derde hoofdstuk, en er wordt aangetoond dat deze aanname niet opgaat als het object in de lengterichting niet voldoende invariant is. Dat wil zeggen, zelfs als de velden voor een invariant object tweedimensionaal zouden zijn, worden ze drie dimensionaal door de interactie van de weefselparameters met de velden welke stromen induceren die aan veldcomponenten bijdragen buiten het tweedimensionale vlak.

Een andere interessante toepassing van gesloten uitdrukkingen tussen stromen en velden is de doelveld methode, die het inverse bronprobleem tussen elektrische stromen en statische magnetische velden regulariseerd door hun relatie tot een cilindrische geometrie te beperken. Deze methode is aangepast voor transversaal georiënteerde magnetische velden die gebruikt worden met Halbachmagneet opstelling, en er is een open source tool ontwikkeld om de methode eenvoudig toe te passen voor verschillende ontwerpoverwegingen.

Door weg te gaan van de beperkingen van de veld- of stroomstructuur, tonen we de ingewikkelde relatie tussen elektrische eigenschappen en het gemeten signaal in een magnetic resonance imaging (MRI) scanner. Dit wordt gedaan door het afleiden van de electro- (en magneto-) motorische kracht voor een typisch MRI scenario zonder enige aannames over het object of de electro-magnetische velden. Dit model kan dan zelfs worden gebruikt om elektrische eigenschappen te reconstrueren uit het meest eenvoudige MRI-signaal, de free induced decay (FID).

Om ons onderzoek naar elektrische eigenschappen af te ronden maken we een kleine omweg naar de magnetische weefseleigenschap, de permeabiliteit of de magnetische gevoeligheid. Voor de reconstructie van deze weefseleigenschap is een dipooldeconvolutie nodig, waarbij je door de dipoolconvolutie door de nullen van de dipoolkern informatie van het oorspronkelijke object verliest. In het laatste hoofdstuk

van dit proefschrift wordt een nieuwe, op machinaal leren gebaseerde aanpak onderzocht om de verloren informatie te reconstrueren.

Zusammenfassung

Elektrische Eigenschaften, die Leitfähigkeit und Permittivität von Gewebe sind Größen, die die Wechselwirkung zwischen einem Objekt und elektromagnetischen Feldern beschreiben. Sie beeinflussen elektrisch-magnetische Felder, werden aber selbst durch physiologische Phänomene wie Läsionen oder einen Schlaganfall beeinflusst. Daher sind sie wichtig für die Identifizierung oder Diagnose des Schweregrads von Pathologien sowie wesentlich für die Sicherheit und Effizienz der MRT durch die Bestimmung der Gewebeerwärmung oder der Empfindlichkeit gegenüber Erregungsimpulsen.

Bei zweidimensionalen elektromagnetischen Feldern, die in spezifischen Messgeometrien auftreten, ist es möglich, die Beziehung zwischen elektromagnetischen Feldern und elektrischen Eigenschaften zu vereinfachen und diese Eigenschaften im Wesentlichen durch eine Vorwärtsoperation zu rekonstruieren, wobei auf ein vollständiges Inversionsschema verzichtet wird. Diese Erkenntnisse haben auch dazu beigetragen, die Ursache für bestimmte Artefakte zu finden und zu erklären, z.B. die getroffenen Feld- oder Objektannahmen.

Mit zweidimensionalen Magnetfeldgleichungen ist es auch möglich, die Beziehung zwischen elektrischen Strömen (durch die elektrische Stromdichte) und dem Magnetfeld mit Hilfe eines Ausdrucks in geschlossener Form zu beschreiben, der, wenn er auf eine zylindrische Geometrie beschränkt ist, auf einfache Weise invertiert werden kann. Dies wird als Zielfeldmethode bezeichnet und wird seit den 1980er Jahren für den Entwurf von Gradientenspulen verwendet. Wir haben die Gleichungen für ein transversal orientiertes Magnetfeld, wie es von einem Halbach-Array erzeugt wird, angepasst, um Gradienten für den Niederfeld-Scanner des Leiden university medical center (LUMC) zu entwickeln.

Weg von den zweidimensionalen Annahmen über Geometrie und Feldkomponenten zeigen wir die komplizierte Beziehung zwischen elektrischen Eigenschaften und dem gemessenen Signal in einem MRT-Scanner. Dies geschieht durch Ableitung der elektro- (und magneto-)motorischen Kraft für ein typisches MRT-Szenario ohne Annahmen über das Objekt oder elektromagnetische Felder. Dieses Modell kann dann sogar verwendet werden, um elektrische Eigenschaften aus dem einfachsten MRT-Signal, dem free induced decay (FID), zu rekonstruieren.

Abgerundet wird die Untersuchung der elektrischen Eigenschaften durch einen kurzen Abstecher zur magnetischen Gewebeeigenschaft, der Permeabilität oder magnetischen Suszeptibilität. Zur Rekonstruktion dieser Gewebeeigenschaft ist eine Dipoldevolution erforderlich, bei der die Dipolfaltung durch die Nullstellen des Dipolkerns Informationen des ursprünglichen Objekts verliert. Ein neuer, auf maschinellem Lernen basierender Ansatz zur Rekonstruktion der verlorenen Information wird im letzten Kapitel dieser Arbeit untersucht.

Preface

This thesis is part of a collaboration between the Indian institute of science (IISC) and the Delft University of Technology. The collaboration aims to bring together researchers to work on signal processing for magnetic resonance imaging (MRI) in a low resource setting. Low resource setting relates here both to the cost of the MRI scanner and the siting requirements and robustness of the apparatus.

This resulted in a dual PhD exchange between myself and Shubham Sharma at the IISC. While my colleague from the IISC looked at possible measurement trajectories to speed up measurements and most optimally collect data, my research and this thesis looks at a more fundamental side of the signal acquisition in MRI. In doing so we aimed to provide the groundwork for a shift in acquisition strategies.

I would like to invite you to take a read of these past four years of research and hope you can enjoy it just as much as I have enjoyed writing and working on it. Many hot days in India and cold summers in Delft have been spent figuring out the intricacies of electrical properties and currents in an MRI setting, but not all secrets will be lifted in this work, so stay tuned for more!

Patrick Stefan Fuchs
London, November 2020

1

Introduction

Die Praxis sollte das Ergebnis des Nachdenkens sein, nicht umgekehrt.

Herman Hesse

Where else can you go to Tim Hortons and get a latte, put it in an MRI machine and say "You know what, I'm looking at a quantum mechanical system. I can manipulate a quantum mechanical system."

Andrew Webb

In the summer of 2019, during the annual meeting of the International Society for Magnetic Resonance in Medicine (ISMRM), professor Webb spoke on "Disruptors in the way we gather data".[1] In this presentation he spoke about how we *used to* gather data, how we *are*, how we *should*, and how we *could* gather data. In this work I will present my own take on how we *should* gather data, and an expectation of how we *will* gather data. But first some background on how we *are* gathering data at the moment.

The biggest driving force behind novel signal acquisition strategies in magnetic resonance imaging (MRI) for the past decade is without a doubt the application of compressive sensing techniques. Compressive sensing relies on the fact that the amount of samples needed to reconstruct an image is not dependent on the bandwidth of the signal, but rather on the information content. This is realised by exploiting the sparsity of a signal to recover the underlying process. In MRI this means that, given the right sampling strategy, the amount of measurements or samples that are needed to reconstruct an anatomical image is much smaller than the entire measurement space. This leads to faster scans for images with comparable quality. Ever since the first demonstration of this concept by Lustig et al., it has become a tool we cannot do without anymore.

[1] `https://www.ismrm.org/19/program_files/Plenary01.htm` with the presentation available to the public at `https://youtu.be/EsIwYUZ-99E?t=3510`

Another big development of the last decade in signal processing in general is the use of machine learning tools and neural networks for image processing. These tools as well as the necessary computational hardware have matured immensely, and the MRI community has picked them up and applied them with great success. Sometimes even leading to machine learning development from solutions developed by the MRI community. Now, the hype of machine learning has started to wane and it has acquired its own corner in MRI development as a respectable area of research with known pitfalls, challenges, opportunities, and applications.

All of these developments lead to new acquisition strategies for existing MRI scanners, and allow for the development of new MRI hardware. In acquisition, the new capabilities brought forth from these advanced signal processing concepts lead to new ways of diagnosing diseases and tissue in general. On the other hand, in MRI hardware the developments allow for big opportunities in high field MRI, where the increase in signal strength can lead to exponentially faster scanning when utilised correctly, and at the low end of the spectrum stronger computational power allows cheaper hardware to still perform critical imaging tasks with increasing applications.

For both of those disciplines a good understanding of the underlying processes and reliable (and accurate) models of the physics and biological processes is paramount in evaluating new processes and methods and pinpointing where the most room for improvement is as well as potential pitfalls and gaps in our understanding and knowledge on these subjects.

1.1. MRI Diagnostics

In the history of MRI, clinical diagnosis of scan results have almost always been done using *qualitative* images and by expert radiologists. These radiologists have been trained for years to know which type of weighting (T_1, T_2 or tissue density) sequence gives them which contrast between the different types of tissues or pathologies that they are interested in. They then use this contrast, or difference in signal intensity, to perform their diagnosis. However, since the image is always qualitative (or relative) and does not contain absolute values the specific intensity of for example a tumor does not necessarily correspond to its severity or aggressiveness. In addition, when a patient comes back for a checkup at a later date, even if this is performed using the same exact scanner, it is difficult to compare the images in terms of intensity.

Therefore, nowadays there is an increasing push to *quantitative* imaging, enabled by more advanced signal processing as well as hardware improvements. That is, the goal of imaging is not necessarily to get a good contrast between the different tissues under consideration, but rather to accurately reconstruct the actual tissue parameters, which can then be used to give various weights or contrast to an image. Some recent approaches that do just this reconstruction, based on the magnetisation properties, are the dictionary based magnetic resonance fingerprinting (MRF) and the model based magnetic resonance spin tomography in time-domain (MR-STAT) approach. In this work we mostly consider the electrical properties rather than the magnetisation properties, as these directly influence the electromagnetic fields, and lead to induced currents inside the object. Their influence on pathologies is less well understood, but this is also due to the use of electrical properties in clinical diagnostics being in

its infancy. Reliable reconstruction algorithms are essential to bring these properties into clinical relevance and their development is one of the aims of this work.

1.2. MRI Hardware

As MRI scanners with increasing field strengths are being engineered and built it sometimes seems that this is the biggest area of hardware development, as it requires most funding and large groups of engineers and scientists. Besides these high field developments there are also significant advances at low field strengths, in the development of cheaper, smaller and more portable MRI scanners for point of care or developing nations. In these scanners the emphasis is not so much on being able to control the electromagnetic fields inside the scanner precisely, but rather on being able to do this just well enough to be able to get an acceptable image using sophisticated signal processing strategies. This is necessary to bring the advanced medical diagnostics capabilities of MRI to the masses, as currently around 70% of the world has no access to MRI scans, which is mostly because of the prohibitive siting (power, shielding) requirements and cost of the scanners.

One of such devices is being developed by a team at the Leiden university medical center (LUMC) and Delft university of technology (TU Delft). For this device the target field method for gradient design has been extended, which provides a rigorous physics based approach to relate generated magnetic fields to cylindrical current distributions. These low field scanners will bring about a shift in the way people think about MRI, from expensive hospital visits to point of care diagnostics enabling healthcare wherever it is needed, and bringing the power of MRI developments to a much broader population than previously thought possible.

1.3. Thesis Contributions and Outline

The main contributions of this thesis can be summarised as follows:

1. Providing a means to exploit field structure to perform electrical properties tomography in a two-dimensional field setting, essentially showing that the inverse problem reduces to a forward one when the fields can be decoupled. [A]

2. Investigation of the influence of a two-dimensional field assumption on the reconstruction of electrical properties as well as its validity using a contrast source formulation. [B]

3. Development of a fast and efficient design methodology for transverse oriented gradient fields using the target field method. [C]

4. Derivation of a new comprehensive signal model for MRI, which includes the scattering contribution of tissue that can be used to investigate its influence on MRI measurements. [D]

5. Application of a proximal gradient approach to simplify quantitative susceptibility mapping. [Ch. 6]

After this introduction, electrical properties tomography is the first subject we delve into. Starting off with the Maxwell equations in two dimensions which lead to the first order induced current imaging method, after which this two-dimensionality assumption is put to the test using the contrast source inversion framework in Chapter 3. After this we take a closer look at magnetic fields, specifically magnetostatic gradient design using the target field method for a transverse oriented magnetic background field in Chapter 4. The third part of this thesis takes a closer look at the full Maxwell equations, investigating the contribution of scattering on the measured signal and showing ways to reconstruct electrical properties by incorporating these in the signal model in Chapter 5. To round off our investigation of electromagnetic fields and tissue properties Chapter 6 investigates reconstructing the permeability or magnetic tissue property. This tissue property is related to iron deposits in the body and is especially relevant for brain imaging applications. In this thesis it provides a great application to investigate combining machine learning tools and physical model based knowledge for reconstructions.

List of Peer Reviewed Publications

[A] Patrick Fuchs, Stefano Mandija, Peter Stijnman, Wyger Brink, Nico van den Berg, and Rob Remis, *"First-Order Induced Current Density Imaging and Electrical Properties Tomography in MRI"*, IEEE Transactions on Computational Imaging, 4(4), (2018), pp. 624–631.

[B] Reijer Leijsen†, Patrick Fuchs†, Wyger Brink, Andrew Webb, and Rob Remis, *"Developments in Electrical Properties Tomography Based on the Contrast Source Inversion Method"*, Journal of Imaging, 5(2), (2019).

[C] Bart de Vos*, Patrick Fuchs, Thomas O'Reilly, Andrew Webb, and Rob Remis, *"Gradient Coil Design and Realization for a Halbach-Based MRI System"*, IEEE Transactions on Magnetics, 56(3), (2020).

[D] Patrick Fuchs, and Rob Remis, *"Generalized Signal Models and Direct FID-Based Dielectric Parameter Retrieval in MRI"*, IEEE Transactions on Antennas and Propagation, 2020, *submitted*.

[E] Peter Stijnman*, Stefano Mandija, Patrick Fuchs, Nico van den Berg, and Rob Remis, *"Transceive Phase Corrected 2D Contrast Source Inversion-ElectricalProperties Tomography"*, Magnetic Resonance in Medicine, (2020).

†: Authors contributed equally.
*: Under supervision by author.

List of Conference Proceedings and Talks

[a] Patrick Fuchs, and Rob Remis, *"A first order induced current density imaging and electrical properties tomography method in MRI"*, International Society for Magnetic Resonance in Medicine (ISMRM) Benelux Chapter 9th Annual Meeting, Tilburg, Netherlands, Jan. 2017.

[b] Rob Remis, Stefano Mandija, Reijer Leijsen,Patrick Fuchs, Peter Stijnman, and Nico van den Berg, *"Electrical properties tomography using contrast source inversion techniques"*, International Conference on Electromagnetics in Advanced Applications (ICEAA), Verona, Italy, Sep. 2017.

[c] Patrick Fuchs, Stefano Mandija, Peter Stijnman, Wyger Brink, Nico van den Berg, and Rob Remis, *"A Fast and Dedicated First-Order Differencing EPT Reconstruction Method"*, International Society for Magnetic Resonance in Medicine (ISMRM) Benelux Chapter 10th Annual Meeting, Antwerpen, Belgium, Jan. 2018.

[d] Patrick Fuchs, Stefano Mandija, Peter Stijnman, Wyger Brink, Nico van den Berg, and Rob Remis, *"A Fast and Dedicated First-Order Differencing EPT Reconstruction Method"*, International Society for Magnetic Resonance in Medicine (ISMRM) 26th Annual Meeting and Exhibition, Paris, France, June 2018.

[e] Peter Stijnman, Stefano Mandija, Patrick Fuchs, Rob Remis, and Nico van den Berg, *"Transceive Phase Correced Contrast Source Inversion-Electrical Properties Tomography"*, International Society for Magnetic Resonance in Medicine (ISMRM) 26th Annual Meeting and Exhibition, Paris, France, June 2018.

[f] Patrick Fuchs, Reijer Leijsen, and Rob Remis, *"Limitations of 2-D Field Structure Assumptions in Electrical Properties Tomography and its 3-D CSI-EPT Solution"*, International Society for Magnetic Resonance in Medicine (ISMRM) Benelux Chapter 11th Annual Meeting, Leiden, Netherlands, Jan. 2019.

[g] Patrick Fuchs, and Rob Remis, *"Two-Dimensional Electrical Properties Tomography Using a Simplified Contrast-Source Inversion Approach"*, international applied computational electromagnetics society (ACES) Symposium, Miami, USA, Apr. 2019.

[h] Patrick Fuchs, Reijer Leijsen, and Rob Remis, *"Limitations of 2-D Field Structure Assumptions in Electrical Properties Tomography and its 3-D CSI-EPT Solution"*, International Society for Magnetic Resonance in Medicine (ISMRM) 27th Annual Meeting and Exhibition, Montreal, Canada, May 2019.

[i] Patrick Fuchs, and Rob Remis, *"Analytical Full-wave Free Induction Decay Signal Model for MRI"*, International Conference on Electromagnetics in Advanced Applications (ICEAA), Granada, Spain, Sep. 2019.

[j] Bart de Vos, Patrick Fuchs,Thomas O'reilly, Andrew Webb, and Rob Remis, *"Gradient design for a low-field Halbach array using the Target Field Method"*, International Society for Magnetic Resonance in Medicine (ISMRM) Benelux Chapter 12th Annual Meeting, Arnhem, Netherlands, Jan. 2020.

[k] Bart de Vos, Patrick Fuchs,Thomas O'reilly, Andrew Webb, and Rob Remis, *"Gradient design for a low-field Halbach array using the Target Field Method"*, International Society for Magnetic Resonance in Medicine (ISMRM) 28th Annual Meeting and Exhibition, Sydney, Australia, August. 2020 (online due to COVID-19).

2

First-Order Induced Current Density Imaging and Electrical Properties Tomography in MRI

Patrick Fuchs
Stefano Mandija
Peter Stijnman
Wyger Brink
Nico van den Berg
Rob Remis

ABSTRACT– *In this paper, we present an efficient dedicated electrical properties tomography algorithm (called* first-order current density EPT*) that exploits the particular radio frequency field structure, which is present in the midplane of a birdcage coil, to reconstruct conductivity and permittivity maps in this plane from* $\tilde{B}_1^+$ *data. The algorithm consists of a current density and an electrical properties step. In the current density reconstruction step, the induced currents in the midplane are determined by acting with a specific first-order differentiation operator on the* $\tilde{B}_1^+$ *data. In the electrical properties step, we first determine the electric field strength by solving a particular integral equation, and subsequently determine conductivity and permittivity maps from the constitutive relations. The performance of the algorithm is illustrated by presenting reconstructions of a human brain model based on simulated (noise corrupted) data and of a known phantom model based on experimental data. The method manages to reconstruct conductivity profiles without model related boundary artefacts. Additionally, it is more robust to noise because only first-order differencing of the data is required as opposed to second-order data differencing in Helmholtz-based approaches. Moreover, reconstructions can be performed in less than a second, allowing for essentially real-time electrical properties mapping.*

Appeared in:
IEEE Transactions on Computational Imaging **4**, *4, pp. 624–631, December 2018*
doi: 10.1109/TCI.2018.2873407

2.1. Introduction

The main objective of electrical properties tomography (EPT) is to retrieve the conductivity and permittivity of tissue from $\tilde{B}_1^+$ data as measured by an magnetic resonance imaging (MRI) scanner. Knowledge about these parameters is extremely important in a wide variety of clinical applications. Permittivity especially of interest at high field MRI where it can have a significant influence on the (radio frequency (RF)) field distributions. The conductivity is of potential importance as an endogenous biomarker in oncology [1] and acute stroke imaging [2, 3], for example, and the conductivity along with the electric field strength is also required to determine the specific absorption rate (SAR) inside the human body [4] – [5].

Many different EPT methods have been developed over the years ranging from local differential equation approaches (see [6] – [7], for example) to methods that use global integral Green's tensor field representations in an optimization setting to find the dielectric tissue maps at the Larmor frequency of operation [8, 9]. The local differential-based EPT methods are direct non-iterative reconstruction methods, often based on the Helmholtz equation for the RF magnetic field. Standard Helmholtz-based EPT (magnetic resonance (MR)-EPT) [10] requires a constant dielectric profile and second-order spatial differentiation of the data. Care must be taken when implementing this differentiation operation to mitigate noise amplification [3, 11, 12]. On the other hand, in the global integral-based approach the dielectric tissue parameters are determined in an iterative manner by minimizing an objective function. Here, integral operators act on the data, which makes the method more robust to noise. A disadvantage of the global approach is that it is more complex to implement than a direct method and its computational costs are generally much higher. However, strongly inhomogeneous tissue profiles are easily incorporated in a global method and regularization can be added to the objective function to further suppress the effects of noise.

A number of EPT methods have been developed using two-dimensional datasets [8, 12, 13], whereas there are also methods that work on fully three-dimensional $\tilde{B}_1^+$ data sets [9, 14]. We shall focus on two-dimensional measurements, as it has been shown [15] that the RF field is essentially E-polarized in the midplane of a birdcage coil, meaning that the electric field strength is mainly directed in the longitudinal z-direction, while the magnetic field strength has transverse x- and y-components only. In this paper, we present a dedicated EPT method that exploits this particular field structure.

In particular, in our first-order induced current EPT method (foIC-EPT) we exploit the structure of the RF field and obtain the induced current density by acting with a particular first-order differential operator on collected $\tilde{B}_1^+$ data. Since this operation provides us with an image of the currents that are induced in tissue that is present in the (mid) plane of interest, we call this step the *induced current reconstruction step* of our method. We note that current density imaging in the context of the Helmholtz equation has also been investigated in [16], for example.

In the second *electrical properties step* of our method, the conductivity and permittivity maps are reconstructed by first computing the electric field strength and subsequently employing the constitutive relations between the induced currents and the

electric field strength. Our foIC-EPT can therefore be seen as a hybrid method, in which a local differentiation operator is used to obtain the currents and a global integral operator is used to obtain the electric field.

Similar to most of the EPT approaches mentioned above, foIC-EPT relies on the transceive phase approximation [17] to obtain conductivity and permittivity reconstructions from $\tilde{B}_1^+$ data. The effects of this approximation on the reconstructions is presently not fully understood and application of this approximation may result in reconstruction errors. A possible reconstruction strategy for iterative volume-integral EPT methods that overcomes this drawback has been reported in [18], however.

Finally, we note that foIC-EPT is a dedicated EPT method, in the sense that it exploits the particular field structure that is present in the midplane of a birdcage coil. This makes the method very efficient and it produces images of the induced current density and conductivity and permittivity maps with no boundary artefacts related to any underlying assumptions on the electrical property distribution and essentially in real time even on a standard PC or laptop (e.g. on an Intel i5 PC with 8 GB of RAM).

2.2. Induced Current Density Imaging

In this section, we describe the induced current step of our EPT algorithm. This step is based on the observation presented in [15] that the RF field in the midplane of a birdcage coil is essentially E-polarized. We therefore follow [8], [13], and [15] and consider E-polarized RF fields governed by the Maxwell equations

$$-\partial_x \tilde{B}_y + \partial_y \tilde{B}_x + \mu_0 \tilde{J}_z^{\text{ind}} = 0, \tag{2.1}$$

$$\partial_y \tilde{E}_z + \mathrm{j}\omega \tilde{B}_x = 0, \tag{2.2}$$

and

$$-\partial_x \tilde{E}_z + \mathrm{j}\omega \tilde{B}_y = 0, \tag{2.3}$$

where $\tilde{J}_z^{\text{ind}} = (\sigma + \mathrm{j}\omega\varepsilon)\tilde{E}_z$ is the induced current density, we use a $\exp(+\mathrm{j}\omega t)$ time convention, and the tilde is used to denote frequency domain quantities. This density can be imaged in a straightforward manner from available $\tilde{B}_1^+$ data where $\tilde{B}_1^+$ is given by

$$\tilde{B}_1^+ = \frac{\tilde{B}_x + \mathrm{j}\tilde{B}_y}{2}. \tag{2.4}$$

Specifically, introducing the operator

$$\partial^- = \partial_x - \mathrm{j}\partial_y, \tag{2.5}$$

we have

$$\partial^- \tilde{B}_1^+ = \frac{1}{2}\left[\partial_x \tilde{B}_x + \partial_y \tilde{B}_y - \mathrm{j}\left(\partial_y \tilde{B}_x - \partial_x \tilde{B}_y\right)\right] \tag{2.6}$$

and using Equation (2.1) and $\partial_x \tilde{B}_x + \partial_y \tilde{B}_y = 0$, we arrive at

$$\tilde{J}_z^{\text{ind}} = \frac{2}{\mathrm{j}\mu_0}\partial^- \tilde{B}_1^+. \tag{2.7}$$

This is our basic imaging formula. Since it is based on the first-order Maxwell system, only first-order differentiation operators act on $\tilde{B}_1^+$ data and since there are no additional (higher-order) differentiation operations in the following second step of our method (see Section 2.3), the entire method only contains first-order differentiation operators, as opposed to EPT techniques which are based on second-order (Helmholtz) equations, where a second-order differentiation operator (Laplacian) is applied to the data. The above imaging formula is therefore less sensitive to perturbations or noise and, since for the same accuracy finite difference approximation a smaller kernel can be used, boundary artefacts related to the discrete nature of the finite differencing kernel are also less severe compared with second-order approaches. Lastly, no assumptions on the electrical properties have been made in the definition of the induced currents, whereas Helmholtz based methods have to assume constant dielectric parameters.

2.3. Electrical Properties Reconstruction

Up to this point, we have addressed imaging of the induced current density inside the human body. This density depends on the external sources through the fields that are excited by these sources. The conductivity and permittivity parameters are intrinsic properties of tissue that do not depend on the external sources. To retrieve the tissue parameters, we therefore have to take the presence of the external sources into account. To this end, we set up a volume-integral scattering formalism (see, for example, [19] – [20]) and define the incident RF field $\left\{\tilde{B}_x^{\text{inc}}, \tilde{B}_y^{\text{inc}}, \tilde{E}_z^{\text{inc}}\right\}$ as the field that is present in an empty (air-filled) birdcage coil. The scattered magnetic field $\left\{\tilde{B}_x^{\text{sc}}, \tilde{B}_y^{\text{sc}}, \tilde{E}_z^{\text{sc}}\right\}$ is introduced as the difference between the total field and the incident field. Specifically,

$$\left\{\tilde{B}_x^{\text{sc}}, \tilde{B}_y^{\text{sc}}, \tilde{E}_z^{\text{sc}}\right\} = \left\{\tilde{B}_x, \tilde{B}_y, \tilde{E}_z\right\} - \left\{\tilde{B}_x^{\text{inc}}, \tilde{B}_y^{\text{inc}}, \tilde{E}_z^{\text{inc}}\right\} \tag{2.8}$$

and the scattered electric field due to the presence of the body is given by (see [19] – [20], for example)

$$\tilde{E}_z^{\text{sc}}(\boldsymbol{\rho}) = \mathrm{j}\omega\mu_0 \int_{\boldsymbol{\rho}' \in \mathbb{D}} \tilde{G}(\boldsymbol{\rho} - \boldsymbol{\rho}')\, \tilde{J}_z^{\text{sc}}(\boldsymbol{\rho}')\, \mathrm{d}V, \tag{2.9}$$

where $\mathbb{D}$ is the body domain. This integral representation holds for all observation points in the midplane of the body coil. Furthermore,

$$\tilde{G}(\boldsymbol{\rho}) = -\frac{\mathrm{j}}{4} H_0^{(2)}(k_0|\boldsymbol{\rho}|) \tag{2.10}$$

is the Green's function of the homogeneous background medium (air) with $k_0 = \omega/c_0$ its corresponding wave number and $H_0^{(2)}$ the Hankel function of the second kind and order zero. Finally, $\tilde{J}_z^{\text{sc}}$ is the scattering source given by

$$\tilde{J}_z^{\text{sc}} = \tilde{J}_z^{\text{ind}} - \mathrm{j}\omega\varepsilon_0\tilde{E}_z \quad \text{for} \quad \boldsymbol{\rho} \in \mathbb{D}. \tag{2.11}$$

Substituting this scattering source (Equation (2.11)) in the integral representation of Equation (2.9), using the imaging equation (2.7), and the definition of the scattered electric field strength ($\tilde{E}_z^{\text{sc}} = \tilde{E}_z - \tilde{E}_z^{\text{inc}}$), we find that the electric field satisfies

$$\tilde{E}_z(\boldsymbol{\rho}) + k_0^2 \int_{\boldsymbol{\rho}' \in \mathbb{D}} \tilde{G}(\boldsymbol{\rho} - \boldsymbol{\rho}')\, \tilde{E}_z(\boldsymbol{\rho}')\, \mathrm{d}V = \tilde{E}_z^{\text{inc}}(\boldsymbol{\rho}) - 2\omega \int_{\boldsymbol{\rho}' \in \mathbb{D}} \tilde{G}(\boldsymbol{\rho} - \boldsymbol{\rho}')\, \partial^- \tilde{B}_1^+(\boldsymbol{\rho}')\, \mathrm{d}V \quad (2.12)$$

and $\boldsymbol{\rho} \in \mathbb{D}$. Observe that the right-hand side of Equation (2.12) is known and with $\boldsymbol{\rho} \in \mathbb{D}$, Equation (2.12) is an integral equation for the electric field strength in $\mathbb{D}$ which can be solved iteratively using the generalized minimal residual solver (GMRES), for example [21]. Also note that local noise effects in $\partial^- \tilde{B}_1^+$ are smoothed or smeared out through integration over the body domain. Smoothing is predominantly local, however, because of the singularity of the Green's function at $\boldsymbol{\rho}' = \boldsymbol{\rho}$.

After solving integral equation (2.12), we have the electric field strength at our disposal and the conductivity and permittivity maps at frequency ω can be determined by using the constitutive relation

$$\tilde{J}_z^{\text{ind}}(\boldsymbol{\rho}) = \left[\sigma(\boldsymbol{\rho}) + \mathrm{j}\omega\varepsilon(\boldsymbol{\rho})\right] \tilde{E}_z(\boldsymbol{\rho}), \quad (2.13)$$

for $\boldsymbol{\rho} \in \mathbb{D}$, since both $\tilde{J}_z^{\text{ind}}(\boldsymbol{\rho})$ and $\tilde{E}_z(\boldsymbol{\rho})$ are now known. Explicitly, by equating the real and imaginary parts of the above equation, we obtain the conductivity profile

$$\sigma(\boldsymbol{\rho}) = \frac{2}{\mu_0 \left|\tilde{E}_z(\boldsymbol{\rho})\right|^2} \mathrm{Im}\left[\tilde{E}_z^*(\boldsymbol{\rho}) \partial^- \tilde{B}_1^+(\boldsymbol{\rho})\right], \quad (2.14)$$

while the permittivity profile is given by

$$\varepsilon(\boldsymbol{\rho}) = \frac{-2}{\omega\mu_0 \left|\tilde{E}_z(\boldsymbol{\rho})\right|^2} \mathrm{Re}\left[\tilde{E}_z^*(\boldsymbol{\rho})\, \partial^- \tilde{B}_1^+(\boldsymbol{\rho})\right], \quad (2.15)$$

where * denotes complex conjugation. Note that the conductivity and permittivity can only be retrieved at points $\boldsymbol{\rho} \in \mathbb{D}$ where the electric field strength does not vanish. Our overall electrical properties tomography approach can now be summarized in Algorithm 1. Note that the z-component of the incident electric field strength is not required to carry out induced current step 1, but is required to carry out electrical properties step 2.

2.4. Simulation and Experiment

In this section, we illustrate the performance of foIC-EPT using simulated and measured $\tilde{B}_1^+$ data. Specifically, we apply foIC-EPT to simulated $\tilde{B}_1^+$ data collected inside the head of the female body model Ella of the foundation for research on information technologies in society (IT'IS) foundation [22] and corrupt this data with noise. Subsequently, we apply the foIC-EPT algorithm to measured $\tilde{B}_1^+$ data obtained for a cylindrical inhomogeneous phantom.

Algorithm 1 First-Order Induced Current EPT (foIC-EPT).

- Given the measured $\tilde{B}_1^+$-field in the midplane of the birdcage coil, and the corresponding incident electric field $\tilde{E}_z^{\text{inc}}$:

1 Determine the induced current density using Equation (2.7).

2.a Determine the corresponding electric field strength by solving a specific integral equation (2.12).

2.b Knowing the induced current density and the electric field strength, determine the conductivity and permittivity profiles using Equations (2.14) and (2.15).

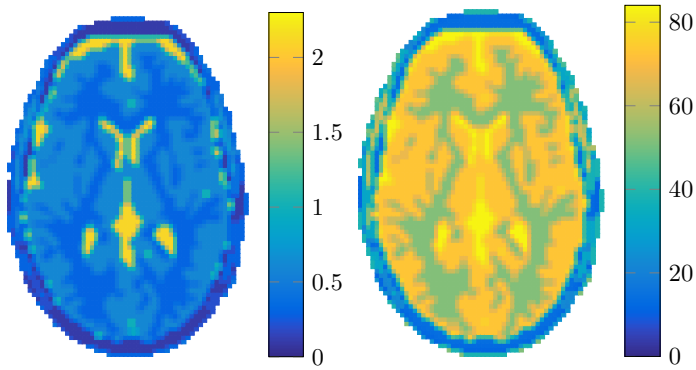

Figure 2.1: Conductivity map in $\mathrm{S\,m^{-1}}$ (left) and relative permittivity map (right) of the center slice head model.

2.4.1. Imaging based on simulated data

The head model of the IT'IS foundation has a voxel size of 2.5 $\mathrm{mm^3}$ isotropic and the conductivity and permittivity maps of the slice that coincides with the midplane of the birdcage coil are shown in Figure 2.1. The coil and corresponding incident field are simulated by positioning 16 line sources uniformly on a circle that is concentric to the head model. The radius of this circle is 34 cm and the line sources operate in quadrature mode at a frequency of 128 MHz, which corresponds to the operating frequency of a 3 T MRI scanner. The simulation was performed at the same resolution as the phantom (2.5 $\mathrm{mm^3}$ isotropic), and the simulation was programmed in MATLAB 2015b (The MathWorks, Inc., Natick, Massachusetts, United States) using an in-house simulation code. Furthermore, we corrupt the $\tilde{B}_1^+$ data by complex white Gaussian noise such that we have an signal to noise ratio (SNR) of 20 dB (100 on a linear scale).

Since the conductivity and permittivity maps of the body model are known in this example, we can numerically compute the exact induced current density within our slice of interest. The magnitude of this current density is shown in Figure 2.2 (left),

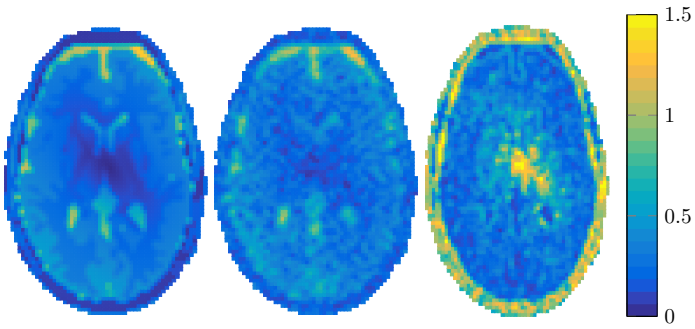

Figure 2.2: Normalised magnitude of the exact induced current density $\tilde{J}_z^{\text{ind}}$ in the center slice of the Ella head model (left), magnitude of the reconstructed current density using imaging formula (2.7) on noisy $\tilde{B}_1^+$ data (middle), and the pointwise relative error of the reconstructed induced current density (right). The left and middle density plots have been normalized with respect to $\max|\tilde{J}_z^{\text{ind}}|$. The colorbar refers only to the error plot.

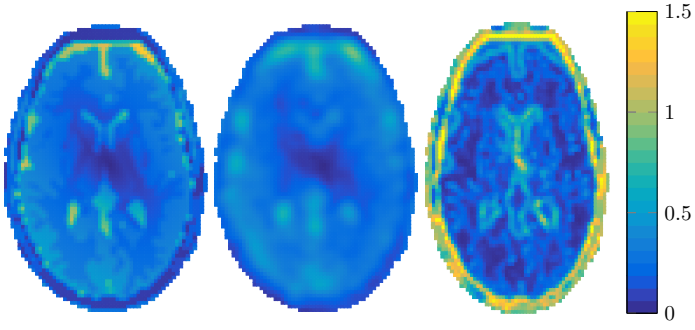

Figure 2.3: Normalised magnitude of the exact induced current density $\tilde{J}_z^{\text{ind}}$ in the center slice of the Ella head model (left), magnitude of the reconstructed current density using imaging formula (2.7) on filtered noisy $\tilde{B}_1^+$ data (middle), and the pointwise relative error of the reconstructed induced current density (right). The left and middle density plots have been normalized with respect to $\max|\tilde{J}_z^{\text{ind}}|$. The colorbar refers only to the error plot.

while the reconstruction based on imaging formula (2.7) is shown in Figure 2.2 (middle). The pointwise relative error between the numerically computed induced current density and the reconstructed density is shown in Figure 2.2 (right). We observe that the largest errors occur near the interfaces between different tissue types, especially at the outer regions of the head. Furthermore, there is a large error in the center of the reconstruction, which is due to a low E-field at this location, that exacerbates the presence of noise in the data.

Sensitivity to noise is not as severe as in Helmholtz-based approaches, however, since in the latter approaches a second-order differentiation operator (Laplacian) acts on the data, while in our induced current step only the first-order derivative of collected $\tilde{B}_1^+$ data is computed. For differencing a first order forward kernel was used, which would lead to single voxel boundary artefacts if the measured data would be perfectly masked to the size of the head. However, in this simulation this mask was chosen

one voxel larger to remove this purely numerical error.

To suppress the effects of noise that is present in the input data, we now first filter this data using a five-point (5×5) Gaussian image filter with mean zero and variance 2. This will lead to some loss of spatial resolution, but will reduce the noise amplification effect due to differentiation of the data. A median filter has also been applied and works well in preserving edge information in high SNR regions, but creates artefacts in low SNR regions due to the nonlinear nature of the filter and the smooth nature of the B_1^+ map.

Subsequently, we apply Equation (2.7) on the filtered data to obtain the reconstructed induced current density as shown in Figure 2.3 (middle) along with the exact current density and pointwise relative error shown in Figure 2.3 (left) and Figure 2.3 (right), respectively. The pointwise relative error is given by

$$\left|(\boldsymbol{u}_{\text{true}} - \boldsymbol{u}_{\text{reconstructed}}) \odot \boldsymbol{u}_{\text{true}}^{-1}\right|,$$

where $\otimes$ signifies the elementwise or Hadamard product. The quality of our one-step imaging result has clearly improved, and we therefore use the filtered $\tilde{B}_1^+$ data to carry out the electrical properties step of foIC-EPT (step 2 of the foIC-EPT algorithm). Specifically, we use the filtered $\tilde{B}_1^+$ data to compute the right-hand side of equation (2.12). Having this right-hand side available, we solve the integral equation (2.12) using the GMRES algorithm, whith the spatial convolution integral equation implemented using FFTs as described in [23]. It takes about ten iterations to arrive at a normalized residual of 1×10^{-6} (matrix size 256×256) and the resulting electric field strength is shown in Figure 2.4 (middle). The corresponding exact electric field strength is shown in Figure 2.4 (left) and the pointwise relative error between the exact and reconstructed electric fields is shown in Figure 2.4 (right). Overall, the electric field strength is fairly well reconstructed, except at the center of the slice, where the magnitude of the exact electric field strength essentially vanishes. For antennas in a birdcage setting and operating in quadrature mode, it is well-known that the magnitude of the electric field strength is small in a neighborhood of the center of the slice (see [8], for example) and it is difficult to accurately reconstruct this field based on noisy $\tilde{B}_1^+$ input data [24].

Having reconstructed the electric field strength from $\tilde{B}_1^+$ data, we can determine the conductivity and permittivity maps using Equations (2.14) and (2.15), respectively. The reconstructed conductivity map is shown in Figure 2.5 (right), while the reconstructed permittivity map is shown in Figure 2.6 (right). Reconstructions of the conductivity and permittivity maps based on noiseless $\tilde{B}_1^+$ data are shown in Figure 2.5 (middle) and Figure 2.6 (middle), respectively, thereby highlighting the effects of noise on the conductivity and permittivity reconstructions. In particular, for noisy data smooth reconstructions are obtained due to filtering and for both noiseless and noisy data the error is maximum around the center of the slice, since the error in the reconstruction of the electric field is maximum in this neighborhood and the magnitude of the electric field strength is small at this location as well. A low E-field leads to induced electric currents $\tilde{J}_z^{\text{ind}}$ that give a small to negligible contribution to the $\tilde{B}_1^+$ field and reconstructing the conductivity and permittivity at such locations is therefore very challenging. Finally, we mention that it takes our implementation of the overall foIC-

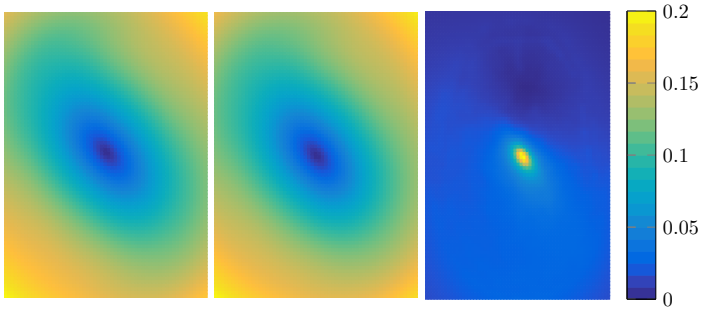

Figure 2.4: Normalised magnitude of the exact electric field strength $\tilde{E}_z$ in the center slice of the Ella head model (left), magnitude of the reconstructed electric field strength based on filtered $\tilde{B}_1^+$ data (middle), and the pointwise relative error of the reconstructed electric field strength (right). The left and middle field strength plots have been normalized with respect to $\max|\tilde{E}_z|$. The colorbar refers only to the error plot.

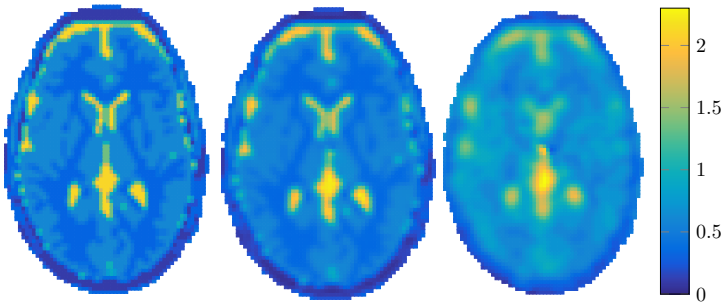

Figure 2.5: Original (left) and reconstructed conductivity maps in S/m based on noiseless (middle) and noisy (right) $\tilde{B}_1^+$ data.

EPT algorithm less than a second to retrieve the conductivity and permittivity maps from the collected $\tilde{B}_1^+$ data on an Intel i5 PC with 8 GB of RAM.

2.4.2. Imaging based on measured data

In this experiment, we use a 1.5% agar based cylindrical phantom filled with saline water to validate our foIC-EPT method. The phantom consists of an inner and an outer cylinder with conductivities given by 0.95 S m^{-1} and 0.45 S m^{-1}, respectively, and a photograph of the phantom is shown in Figure 2.7 (top). The conductivities were independently obtained using the Stogryn equation [25]. A 3 T MRI System (Ingenia, Philips) and a 16 channel head coil (Philips Medical Systems, Best, The Netherlands) were used to obtain the $\tilde{B}_1^+$ data shown in Figure 2.7 (bottom). The amplitude of the $\tilde{B}_1^+$ field was measured using the actual flip-angle imaging (AFI) method [26], while the transceive phase was measured using two single spin echo (SE) sequences with opposing readout polarities [3, 6, 17, 27]. Both sequences were carried out with 10 signal averages, and the field of view is centered at the middle of the coil. Parameter settings of the measurement sequences can be found in Table 1. Furthermore, the phantom was placed at the center, and the system's body

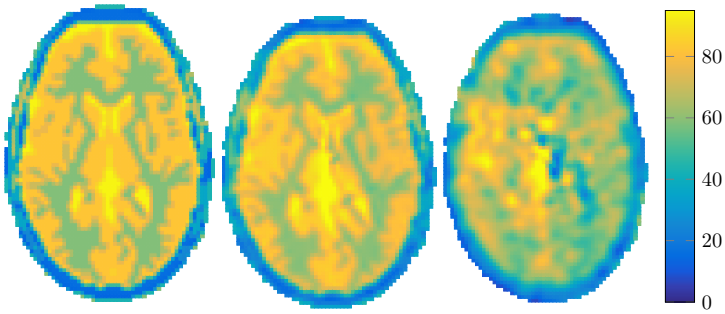

Figure 2.6: Original (left) and reconstructed relative permittivity maps based on noiseless (middle) and noisy (right) $\tilde{B}_1^+$ data.

Table 2.1: Sequence parameters used for the phantom experiment.

Parameters	SE sequence	AFI sequence	Unit
field of view (FoV)	$200 \times 200 \times 2.5$	$200 \times 200 \times 9$	mm^3
Resolution	$2.5 \times 2.5 \times 2.5$	$2.5 \times 2.5 \times 3$	mm^3
Rep. time TR	1000	TR1: 50 TR2: 250	ms
echo time (TE)	5	2.7	ms
Water-fat shift / Bandwidth	$\frac{0.3}{1400}$	$\frac{0.9}{480}$	pixel Hz^{-1}
Flip angle	90	65	°
Signal averages	10	10	#

coil was used for transmitting, while a head coil was used for reception. To remove the impact of the complex sensitivity of the head coil, the receive array data was phase-referenced to the body coil using a built-in routine. In this way, the transmit and receive phase of the birdcage coil determines the observed transceive phase [3, 6, 17, 27]. Subsequently, the transceive phase approximation was applied to obtain an approximate $\tilde{B}_1^+$ phase from the measured transceive phase. Finally, the SNR of the measured data is 17.75 dB (approx. 60 on a linear scale) and 18.75 dB (approx. 75 on a linear scale) for the amplitude and phase scans, respectively.

Having the complex $\tilde{B}_1^+$ data map available, we use the foIC-EPT algorithm to reconstruct the conductivity and permittivity maps of the phantom by essentially following the same steps as in the previous subsection. In particular, first the data is filtered using a Gaussian filter and subsequently the induced current density $\tilde{J}_z^{\text{ind}}$ is determined using the imaging formula of Equation (2.7). The magnitude of the reconstructed current within the reconstruction area is shown in Figure 2.8 (left). In addition, we simulated the $\tilde{B}_1^+$ field using the Sim4Life software package (ZMT, Zurich, Switzerland) and reconstructed the in silico induced currents using Equation (2.7). The magnitude of the in silico induced current is shown in Figure 2.8 (right). Clearly, there is a mismatch at the center of the inner compartment and at its boundary. This

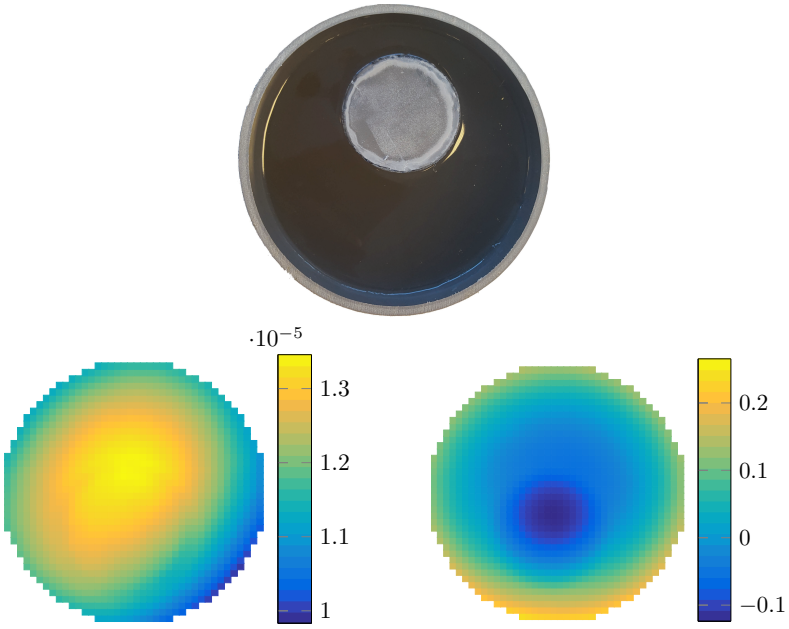

Figure 2.7: Photograph of the phantom (top), the masked amplitude of the measured $\tilde{B}_1^+$ field (left, in $\mathrm{V\,s\,m^{-2}}$) using the AFI sequence as denoted in Table 2.1, and the masked measured transceive phase (right, in rad) using the SE sequences as given in Table 2.1.

mismatch will be discussed further below in combination with the conductivity reconstruction and is also investigated in [18].

To carry out the second step of our reconstruction method, the incident electric field in the imaging plane of interest is required to determine the right-hand side of Equation (2.12). This field was computed using the Sim4Life software package (ZMT, Zurich, Switzerland) obviously using the same configuration as for the in-silico induced current simulations. Having determined the right-hand side of (2.12), we solve the integral equation for the total electric field using the GMRES iterative solver. For this particular configuration, it takes the solver a fraction of a second on an Intel i5 PC with 8 GB of RAM to solve the integral equation in six iterations reaching a normalized residual of 1×10^{-6}.

With the electric field strength now at our disposal, we can determine the conductivity and permittivity profiles of the phantom using Equations (2.14) and (2.15). The reconstructions are shown in the top row of Figure 2.9 along with Helmholtz reconstructions shown in the bottom row of Figure 2.9. The Helmholtz reconstructions were obtained using a smoothed phase-only implementation from [12, 17] that employs a 7×3 finite differencing kernel. We have also attempted a reconstruction using the same (3-point central) differencing kernel but this does not result in meaningful conductivity values at the noise level of the measurement.

We observe that foIC-EPT provides a good overall reconstruction and jumps in the conductivity profile are well resolved. Only small local dips are present in the

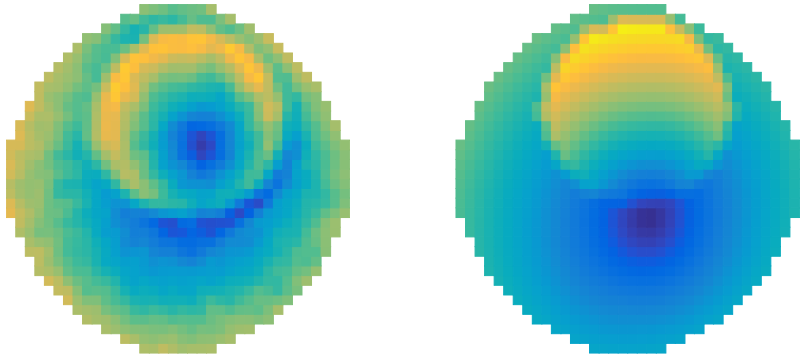

Figure 2.8: Magnitude of the induced current based on measured data (left) and magnitude of the in silico induced-current based on simulated data (right). Both normalised to $\max\left|\tilde{j}_z^{\mathrm{ind}}\right|$ from the simulated data.

conductivity profile near the center of the inner cylinder and to the lower right of the center of the imaging area. These local dips correspond to locations where the reconstructed induced current density is small as well (see Figure 2.8 (left)). Preliminary studies indicate that these dips are due to the application of the transceive phase approximation, but further testing is necessary to confirm these findings. Nevertheless, a good overall agreement with the exact conductivity profile is obtained when using foIC-EPT even in case the transceive approximation is applied. The Helmholtz-based approach, on the other hand, suffers from ripple or edge effects as is evident from the ring-shaped anomaly around the inner cylinder. Such effects are typically observed in standard Helmholtz-based reconstruction approaches as discussed in [10, 12], and [17], for example. The foIC-EPT method does not suffer from such boundary artefacts and is able to reconstruct the piecewise-constant conductivity profile.

The permittivity reconstructions obtained with foIC-EPT and MR-EPT is shown in Figures 2.9b and 2.9d, respectively. In both cases, the reconstructions are poor compared with the quality of the conductivity reconstructions. This should not come as a surprise, however, since permittivity reconstructions are generally very sensitive to perturbations and noise in the data especially at 3 T. More reliable permittivity reconstructions are probably obtained at 7 T or even higher field strengths. Finally, we mention that for this phantom experiment the computation times of foIC-EPT and the Helmholtz approach are 0.041 seconds and 0.027 seconds, respectively, on a standard PC with an Intel i5 (3.1 GHz) and 8 GB of RAM.

2.5. Discussion and Conclusions

In this paper, we have presented a two-step electrical properties tomography technique (foIC-EPT) to reconstruct the conductivity and permittivity maps of tissue based on $\tilde{B}_1^+$ data collected within the midplane of a birdcage coil. The first step consists of reconstructing the induced currents in the midplane of the coil using measured $\tilde{B}_1^+$ data. From the first-order Maxwell equations it follows that these currents can be ob-

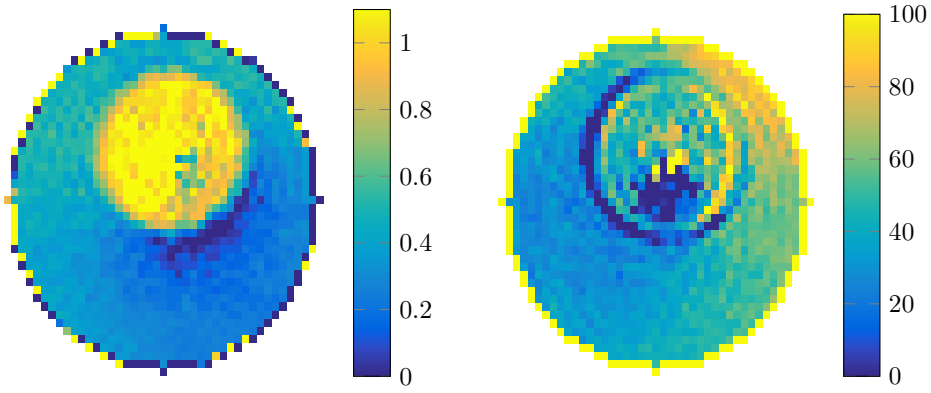

(a) foIC-EPT conductivity reconstruction in S/m.

(b) foIC-EPT relative permittivity reconstruction.

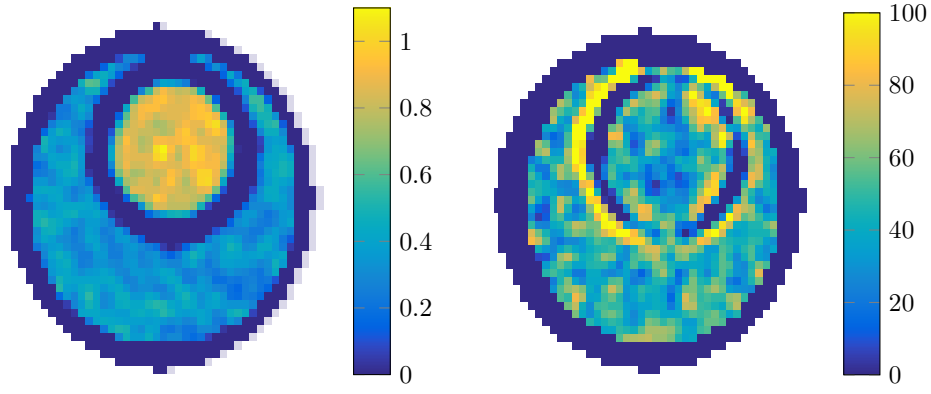

(c) MR-EPT conductivity reconstruction in S/m.

(d) MR-EPT relative permittivity reconstruction.

Figure 2.9: Reconstructed conductivity maps in $\mathrm{S\,m^{-1}}$ and reconstructed relative permittivity maps. The true conductivity of the inner cylinder is $0.95\ \mathrm{S\,m^{-1}}$, while the outer cylinder has a conductivity of $0.45\ \mathrm{S\,m^{-1}}$. The true relative permittivity of the inner and outer cylinder is estimated to be around 80.

tained by acting with a particular first-order differential operator on the collected data. Since only first-order differentiation operators are involved, foIC-EPT is less sensitive to noise compared with (Helmholtz) approaches, where second-order differential operators act on the data.

Having obtained the induced currents from step 1, step 2 consists of computing the electric field inside the plane of interest, by solving a particular integral equation. Iterative solvers are particularly well suited for this task, since the integral that appears in this equation is a spatial convolution integral and fast Fourier transformations (FFTs) can be used to compute matrix-vector products at "FFT-speed." Computationally, this is the most expensive part of the foIC-EPT method, but the examples presented in this paper and additional numerical testing indicates that when the GMRES iterative solver is used, typically less than ten iterations are required to reach an error level of 1×10^{-6}.

After solving the integral equation, the conductivity and permittivity maps can be determined using the induced current density from step 1 and the constitutive relations. For realistic reconstruction problems using simulated or measured data, the complete reconstruction procedure (step 1 and 2) requires a fraction of a second to complete on a standard PC with an Intel i5 processor running at 3.2 GHz and having 8 GB of RAM. This is a significant speed up compared with other optimization-based volume integral equation approaches such as contrast source inversion (CSI)-EPT [8] or the method presented in [9], which typically require tens of seconds or even minutes to arrive at two-dimensional reconstructed conductivity and permittivity maps. We conclude that exploiting field structure in foIC-EPT results in a significant speed up, but also makes the method more restrictive than general volume integral approaches, which do not rely on any particular field structure.

Furthermore, in contrast with the CSI-EPT formulation, we only formulate a volume integral equation for the electric field and take the induced currents as given by Equation (2.7) into account. This is different from CSI-EPT, where the contrast and contrast source (product of the contrast and the electric field) are both unknown and iteratively updated. Here, we already know the induced currents by exploiting the E-polarized field structure.

As opposed to Helmholtz-based approaches, our proposed method, as well as other volume-integral reconstruction methods, can handle jumps in the conductivity and permittivity profiles. No assumptions on the homogeneity of the object have to be imposed and no ripple or edge effects as in Helmholtz-based approaches are observed. However, what foIC-EPT has in common with some other non-Helmholtz-based EPT reconstruction methods is that reconstructions may be poor in regions where the amplitude of the electric field is low. To remedy this situation, active or passive shimming techniques can be applied as discussed in [8] and [13], for example. What the present foIC-EPT method also has in common with many other EPT reconstruction methods is that it relies on the transceive phase approximation, which introduces errors in the reconstructions as well. Numerical simulations and actual experiments indicate that this approximation is responsible for local dips in the reconstructed tissue profiles, but further testing is required. Present and future work focuses on developing an iterative volume-integral EPT reconstruction method that does not rely on the transceive approximation. Preliminary results are promising and have been presented in [18]. Moreover, local dips and variations in reconstructed tissue profiles may also be reduced or even eliminated by incorporating additional regularization strategies such as Total Variation (see [8], for example) into an EPT reconstruction method. Future work will focus on the implementation of such regularization techniques as well.

References

[1] Khin Khin Tha, Ulrich Katscher, Shigeru Yamaguchi, Christian Stehning, Shunsuke Terasaka, Noriyuki Fujima, Kohsuke Kudo, Ken Kazumata, Toru Yamamoto, Marc Van Cauteren, et al. Noninvasive electrical conductivity measurement by MRI: a test of its validity and the electrical conductivity characteristics of glioma. *European radiology*, 28(1):348–355, 2018.

[2] LiXu Liu, WeiWei Dong, XunMing Ji, LiHua Chen, Ling Chen, Wei He, and Jian-Ping Jia. A new method of noninvasive brain-edema monitoring in stroke: cerebral electrical impedance measurement. *Neurological research*, 28(1):31–37, 2006.

[3] Ulrich Katscher and Cornelius AT van den Berg. Electric properties tomography: biochemical, physical and technical background, evaluation and clinical applications. *NMR in Biomedicine*, 30(8):e3729, 2017.

[4] Ji Chen, Zhaomei Feng, and Jian-Ming Jin. Numerical simulation of SAR and B_1-field inhomogeneity of shielded RF coils loaded with the human head. *IEEE transactions on biomedical engineering*, 45(5):650–659, 1998.

[5] Edmond Balidemaj, Cornelis AT van den Berg, Astrid LHMW van Lier, Aart J Nederveen, Lukas JA Stalpers, Hans Crezee, and Rob F Remis. B1-based SAR reconstruction using contrast source inversion–electric properties tomography (CSI-EPT). *Medical & biological engineering & computing*, 55(2):225–233, 2017.

[6] Ulrich Katscher, Tobias Voigt, Christian Findeklee, Peter Vernickel, Kay Nehrke, and Olaf DÖssel. Determination of electric conductivity and local SAR via B_1 mapping. *IEEE transactions on medical imaging*, 28(9):1365–1374, 2009.

[7] Jiaen Liu, Xiaotong Zhang, Sebastian Schmitter, Pierre-Francois Van de Moortele, and Bin He. Gradient-based electrical properties tomography (gEPT): A robust method for mapping electrical properties of biological tissues in vivo using magnetic resonance imaging. *Magnetic resonance in medicine*, 74(3):634–646, 2015.

[8] Edmond Balidemaj, Cornelis AT van den Berg, Johan Trinks, Astrid LHMW van Lier, Aart J Nederveen, Lukas JA Stalpers, Hans Crezee, and Rob F Remis. CSI-EPT: A contrast source inversion approach for improved MRI-based electric properties tomography. *IEEE transactions on medical imaging*, 34(9):1788–1796, 2015.

[9] Ronghan Hong, Shengnan Li, Jianhua Zhang, Youyu Zhang, Na Liu, Zhiru Yu, and Qing Huo Liu. 3-D MRI-based electrical properties tomography using the volume integral equation method. *IEEE Transactions on Microwave Theory and Techniques*, 65(12):4802–4811, 2017.

[10] Jiaen Liu, Yicun Wang, Ulrich Katscher, and Bin He. Electrical properties tomography based on B_1 maps in MRI: Principles, applications, and challenges. *IEEE Transactions on Biomedical Engineering*, 64(11):2515–2530, 2017.

[11] Seung-Kyun Lee, Selaka Bulumulla, and Ileana Hancu. Theoretical investigation of random noise-limited signal-to-noise ratio in mr-based electrical properties tomography. *IEEE transactions on medical imaging*, 34(11):2220–2232, 2015.

[12] Stefano Mandija, Alessandro Sbrizzi, Ulrich Katscher, Peter R Luijten, and Cornelis AT van den Berg. Error analysis of helmholtz-based MR-electrical properties tomography. *Magnetic resonance in medicine*, 80(1):90–100, 2018.

[13] Rita Schmidt and Andrew Webb. A new approach for electrical properties estimation using a global integral equation and improvements using high permittivity materials. *Journal of Magnetic Resonance*, 262:8–14, 2016.

[14] Reijer L Leijsen, Wyger M Brink, Cornelis AT Van Den Berg, Andrew G Webb, and Rob F Remis. 3-D contrast source inversion-electrical properties tomography. *IEEE transactions on medical imaging*, 37(9):2080–2089, 2018.

[15] Bob van den Bergen, Christiaan C Stolk, Jan Bouwe van den Berg, Jan JW Lagendijk, and Cornelis AT Van den Berg. Ultra fast electromagnetic field computations for RF multi-transmit techniques in high field MRI. *Physics in Medicine & Biology*, 54(5):1253, 2009.

[16] GC Scott, MLG Joy, RL Armstrong, and RM Henkelman. RF current density imaging in homogeneous media. *Magnetic resonance in medicine*, 28(2):186–201, 1992.

[17] Astrid LHMW Van Lier, David O Brunner, Klaas P Pruessmann, Dennis WJ Klomp, Peter R Luijten, Jan JW Lagendijk, and Cornelis AT van den Berg. B_1^+ phase mapping at 7 T and its application for in vivo electrical conductivity mapping. *Magnetic Resonance in Medicine*, 67(2):552–561, 2012.

[18] Peter Stijnman, Stefano Mandija, Patrick Fuchs, Rob Remis, and Nico van den Berg. Transceive phase correced contrast source inversion-electrical properties tomography. In *International Society for Magnetic Resonance in Medicine 26th Annual Meeting and Exhibition (ISMRM18)*, page 5087, Paris (France), June 2018.

[19] Adrianus T de Hoop. *Handbook of Radiation and Scattering of Waves*. Academic Press, 1995.

[20] Weng Cho Chew. *Waves and fields in inhomogeneous media*. IEEE press, 1995.

[21] Yousef Saad. *Iterative methods for sparse linear systems*, volume 82. SIAM, 2003.

[22] Andreas Christ, Wolfgang Kainz, Eckhart G Hahn, Katharina Honegger, Marcel Zefferer, Esra Neufeld, Wolfgang Rascher, Rolf Janka, Werner Bautz, Ji Chen, et al. The virtual family—development of surface-based anatomical models of two adults and two children for dosimetric simulations. *Physics in Medicine & Biology*, 55(2):N23, 2009.

[23] Rob Remis and Edoardo Charbon. An electric field volume integral equation approach to simulate surface plasmon polaritons. *Advanced Electromagnetics*, 2(1):15–24, 2013.

[24] Fatih S Hafalir, Omer F Oran, Necip Gurler, and Yusuf Z Ider. Convection-reaction equation based magnetic resonance electrical properties tomography (cr-MREPT). *IEEE transactions on medical imaging*, 33(3):777–793, 2014.

[25] A Stogryn. Equations for calculating the dielectric constant of saline water (correspondence). *IEEE transactions on microwave theory and Techniques*, 19(8):733–736, 1971.

[26] Vasily L Yarnykh. Actual flip-angle imaging in the pulsed steady state: a method for rapid three-dimensional mapping of the transmitted radiofrequency field. *Magnetic Resonance in Medicine: An Official Journal of the International Society for Magnetic Resonance in Medicine*, 57(1):192–200, 2007.

[27] Han Wen. Noninvasive quantitative mapping of conductivity and dielectric distributions using RF wave propagation effects in high-field MRI. In *Medical Imaging 2003: Physics of Medical Imaging*, volume 5030, pages 471–477. International Society for Optics and Photonics, 2003.

3

Developments in Electrical Properties Tomography Based on the Contrast Source Inversion Method

Reijer Leijsen†
Patrick Fuchs†
Wyger Brink
Andrew Webb
Rob Remis

ABSTRACT– *The main objective of electrical properties tomography (EPT) is to retrieve the dielectric tissue parameters from* $\tilde{B}_1^+$ *data as measured by a magnetic resonance (MR) scanner. This is a so-called hybrid inverse problem in which the data is defined* inside *the reconstruction domain of interest. In this paper, we discuss recent and new developments in EPT based on the contrast source inversion (CSI) method. After a short review of the basics of this method, two- and three-dimensional implementations of CSI-EPT are presented along with a very efficient variant of 2-D CSI-EPT called first-order induced current EPT (foIC-EPT). Practical implementation issues that arise when we apply the method to measured data are addressed as well, and the limitations of a two-dimensional approach are extensively discussed. Tissue parameter reconstructions of an anatomical correct male head model illustrate the performance of two- and three-dimensional CSI-EPT. We show that a 2-D implementation produces reliable reconstructions under very special circumstances only while accurate reconstructions can always be obtained with 3-D CSI-EPT.*

Appeared in:
Journal of Imaging, **5**, 2, February 2019
doi: 10.3390/jimaging5020025

†Authors contributed equally

3.1. Introduction

The conductivity and permittivity values of different tissue types are of great importance in a variety of medical applications. In magnetic resonance (MR) safety [1] and hyperthermia treatment planning [2], for example, the conductivity tissue profiles are required to determine the specific absorption rate (SAR). The conductivity may also serve as a bio-marker in oncology or in acute stroke imaging [3]. The permittivity is important since it affects the spatial distribution of the transmitted electromagnetic field responsible for spin excitation.

Typically, the conductivity and permittivity values of tissue are measured *ex vivo* for a particular range of frequencies [4]. Other methods require elaborate hardware such as electrical impedance tomography (EIT) [5] or microwave imaging methods [6]. The objective of electrical properties tomography (EPT) is to retrieve these dielectric tissue values *in vivo* using an MR scanner and standard measurement protocols [3, 7]. Specifically, with an MR scanner, the so-called $\tilde{B}_1^+$-field, defined as $\tilde{B}_1^+ = (\tilde{B}_x + \mathrm{j}\tilde{B}_y)/2$, can be measured at a particular frequency of operation called the Larmor frequency. This frequency is proportional to the magnitude of the static background field B_0 via the relation $f = \gamma B_0$, where $\gamma = 42.577\,\mathrm{MHz\,T^{-1}}$ is the proton gyromagnetic ratio divided by 2π, leading to MR operating frequencies of 128 MHz and 298 MHz for a 3 T and 7 T scanner, respectively.

Reconstruction of the dielectric tissue parameters is based on the measured $\tilde{B}_1^+$-field and what sets EPT apart from other more common inversion and imaging problems is that the measured $\tilde{B}_1^+$-field has its support *inside* the reconstruction domain. The EPT reconstruction problem therefore belongs to the class of so-called hybrid inverse problems [8] and several EPT techniques have been proposed to reconstruct the conductivity and permittivity profiles based on this internal $\tilde{B}_1^+$ data. Loosely speaking, these techniques can be divided into local differential-based approaches (see e.g. [9–12]) and global integral-based approaches (see e.g. [13–19]). Combinations of local and global methods have been developed as well [20, 21].

In this paper, we focus on a global integral-based EPT reconstruction method, called CSI-EPT, where a contrast source inversion approach [22–24] is taken to solve the EPT reconstruction problem. In particular, in CSI-EPT the reconstruction problem is formulated as an optimization problem in which an objective function is iteratively minimized. This objective function consists of a term that measures the mismatch between modeled and measured data (data mismatch) and a term that measures the discrepancy in satisfying Maxwell's equations within the reconstruction domain using a global integral field representation (consistency mismatch). Including the second consistency term in the objective function is crucial to the performance of CSI as shown in [25].

Minimization of the objective function is carried out by iteratively updating a contrast function, which describes the dielectric constitution of the body part of interest, and a so-called contrast source, which is the product of the contrast function and the electric field strength. Updating takes place by fixing one variable and updating the other. More precisely, first the contrast function is fixed and the contrast source is updated and subsequently this is reversed.

The CSI-EPT method was originally introduced in [14], where it was shown that

CSI-EPT is able to reconstruct strongly inhomogeneous conductivity and permittivity profiles within the center slice of an object placed in the center of a body coil in a 3 T MR scanner. The method was initially implemented for E-polarized electromagnetic fields in two-dimensional (2-D) configurations in which the electric field is parallel to the bore axis (z-axis) and the magnetic field is purely transverse, because it is significantly less complex than a full three-dimensional implementation. The use of a 2-D approach was justified, since it was shown that the electromagnetic field in the midplane of a birdcage coil essentially has an E-polarized field structure [26]. An efficient alternative to CSI-EPT, called first-order Induced-Current EPT or foIC-EPT, has been presented as well in [21]. This method exploits the structure of the two-dimensional E-polarized field to efficiently reconstruct the tissue profiles in the midplane of the transmit coil. The foIC-EPT method is significantly faster than CSI-EPT and produces reconstructions in real time with essentially the same quality as 2-D CSI-EPT.

The CSI-EPT method has recently been extended to three-dimensional (3-D) configurations in [27]. With this 3-D implementation of CSI-EPT, volumetric conductivity and permittivity profiles are obtained, and it is no longer necessary to restrict the reconstruction domain to the midplane of a transmit coil. Moreover, 3-D CSI-EPT is based on the vectorial 3-D Maxwell equations and no (E-polarized) field structure is assumed to be present as is the case in a 2-D approach. Unfortunately, computation times dramatically increase compared with 2-D CSI-EPT and foIC-EPT and, depending on the configuration, it may take 3-D CSI-EPT hours or even days to converge even on dedicated high-performance computers or servers. Apart from possible preconditioning techniques that may be applied to accelerate the convergence of 3-D CSI-EPT, 2-D CSI-EPT or foIC-EPT may be preferable in practice, since reconstruction times are significantly shorter compared with 3-D approaches.

In this paper, we thoroughly investigate this issue and compare reconstructions obtained with 2-D CSI-EPT, foIC-EPT, and 3-D CSI-EPT. Reconstruction artifacts in the conductivity and permittivity profiles, the modeled $\tilde{B}_1^+$-field, and the internal electric field are carefully studied. Our analysis shows that only under very special conditions a 2-D approach is justified. Even if the electromagnetic field has an E-polarized field structure in the midplane of the transmit coil, imposing a two-dimensional field structure is generally too limiting an approximation unless the body part of interest and transmit coil strictly satisfy the longitudinal invariance condition.

This paper is organized as follows. In Section 3.2, the 2-D and 3-D CSI-EPT method is briefly reviewed and the governing integral representations are presented as well. A variant of 2-D CSI-EPT, called foIC-EPT, is also presented and a detailed analysis of the performance of all three reconstruction methods is presented in Section 3.3 using a realistic head model from the Virtual Family [28]. A discussion with conclusions can be found in Section 3.4. Finally, we note that the position vectors in 2-D and 3-D are denoted by $\boldsymbol{\rho}$ and $\boldsymbol{x}$, respectively, and we use an $\exp(+\mathrm{j}\omega t)$ time convention.

3.2. Theory

As mentioned above, the CSI-EPT algorithm operates on two unknowns and is based on two fundamental equations. Specifically, the unknowns in CSI-EPT are the contrast function $\tilde{\chi}$ and the contrast source $\tilde{w}$ and the fundamental equations are the data equation and object or state equation.

The contrast function describes the dielectric contrast of the body with respect to free space and is given by $\tilde{\chi}(\boldsymbol{x}) = \varepsilon_{\mathrm{r}}(\boldsymbol{x}) - 1 - \mathrm{j}\sigma(\boldsymbol{x})/\omega\varepsilon_0$, where $\varepsilon_{\mathrm{r}}(\boldsymbol{x})$ and $\sigma(\boldsymbol{x})$ are, respectively, the unknown relative permittivity and conductivity profiles of the body, ε_0 is the permittivity of free space, and ω is the Larmor frequency of operation. The contrast function has the bounded domain $\mathbb{D}_{\mathsf{body}}$ that is occupied by the body as its support, that is the contrast function vanishes for $\boldsymbol{x} \notin \mathbb{D}_{\mathsf{body}}$. Finally, we note that the contrast function is dimensionless and that its real part is determined by the permittivity profile, while its imaginary part is determined by the body's conductivity profile.

The contrast source in CSI-EPT is defined as $\tilde{w} = \tilde{\chi}\tilde{E}$, where $\tilde{\boldsymbol{E}}(\boldsymbol{x})$ is the electric field strength. Note that it is common to refer to $\tilde{w}$ as a contrast source even though it is expressed in volt per meter and is actually a scaled electric field strength. The electric field strength is obviously also unknown, since the dielectric constitution of the body is unknown. Though this field is not of primary interest in EPT, CSI-EPT does provide electric field reconstructions that may be used to reconstruct the local time-averaged power density that is dissipated into heat [1].

To arrive at the two fundamental equations of CSI-EPT, we set up a scattering formalism in which we make use of the linearity of Maxwell's equations and exploit the fact that the body occupies a bounded domain $\mathbb{D}_{\mathsf{body}}$. In particular, we first determine the electromagnetic field that is present inside an empty birdcage coil. In practice, this so-called background field is computed using electromagnetic simulation software and we denote it by $\{\tilde{\boldsymbol{E}}^{\mathrm{b}}, \tilde{\boldsymbol{B}}^{\mathrm{b}}\}$. We note that here the assumption is made that the external currents are impressed and field independent. Consequently, antenna loading is not directly taken into account. The total electromagnetic field in presence of the body is denoted by $\{\tilde{\boldsymbol{E}}, \tilde{\boldsymbol{B}}\}$ and using the linearity of Maxwell's equations this field can be written as

$$\{\tilde{\boldsymbol{E}}, \tilde{\boldsymbol{B}}\} = \{\tilde{\boldsymbol{E}}^{\mathrm{b}}, \tilde{\boldsymbol{B}}^{\mathrm{b}}\} + \{\tilde{\boldsymbol{E}}^{\mathrm{sc}}, \tilde{\boldsymbol{B}}^{\mathrm{sc}}\}, \tag{3.1}$$

where $\{\tilde{\boldsymbol{E}}^{\mathrm{sc}}, \tilde{\boldsymbol{B}}^{\mathrm{sc}}\}$ is the scattered electromagnetic field due to the presence of the body. For this field we have the integral representations

$$\tilde{\boldsymbol{B}}^{\mathrm{sc}}(\boldsymbol{x}) = \int_{\boldsymbol{x}' \in \mathbb{D}_{\mathsf{body}}} \underline{\tilde{\boldsymbol{G}}}^{\mathrm{BJ}}(\boldsymbol{x}, \boldsymbol{x}') \cdot \tilde{w}(\boldsymbol{x}') \, \mathrm{d}V \tag{3.2}$$

and

$$\tilde{\boldsymbol{E}}^{\mathrm{sc}}(\boldsymbol{x}) = \int_{\boldsymbol{x}' \in \mathbb{D}_{\mathsf{body}}} \underline{\tilde{\boldsymbol{G}}}^{\mathrm{EJ}}(\boldsymbol{x}, \boldsymbol{x}') \cdot \tilde{w}(\boldsymbol{x}') \, \mathrm{d}V, \tag{3.3}$$

where $\underline{\tilde{G}}^{\mathrm{EJ}}$ and $\underline{\tilde{G}}^{\mathrm{BJ}}$ are essentially the electric-current to electric field and electric-current to magnetic field Green's tensors of the background medium. Note that these are the Green's tensors of a homogeneous background medium and the presence of the coil is not taken into account. Explicit expressions for these tensors are given below.

Having these integral representations at our disposal, we can now present the basic CSI-EPT equations. We start with the equation that relates the measured $\tilde{B}_1^+$-field to the contrast source. In particular, using the integral representation for the scattered magnetic field of Equation (3.2), we have

$$\tilde{B}_1^{+;\mathrm{sc}}(\boldsymbol{x}) = \frac{\tilde{B}_x^{\mathrm{sc}} + \mathrm{j}\tilde{B}_y^{\mathrm{sc}}}{2} = \frac{1}{2} \int\limits_{\boldsymbol{x}' \in \mathbb{D}_{\mathrm{body}}} \sum_{k=x,y,z} \left[\tilde{G}_{xk}^{\mathrm{BJ}}(\boldsymbol{x}, \boldsymbol{x}') + \mathrm{j}\tilde{G}_{yk}^{\mathrm{BJ}}(\boldsymbol{x}, \boldsymbol{x}') \right] \tilde{w}_k(\boldsymbol{x}') \, \mathrm{d}V, \quad (3.4)$$

which can be written more compactly as

$$\tilde{B}_1^{+;\mathrm{sc}}(\boldsymbol{x}) = \mathcal{G}_{\mathrm{data}}\{\tilde{\boldsymbol{w}}\}(\boldsymbol{x}) \quad \text{for} \quad \boldsymbol{x} \in \mathbb{D}_{\mathrm{body}}, \quad (3.5)$$

where the linear data operator $\mathcal{G}_{\mathrm{data}}$ is implicitly defined in Equation (3.4). Equation (3.5) is known as the *data equation* and relates the unknown contrast source $\tilde{\boldsymbol{w}}$ to the scattered $\tilde{B}_1^+$-field. Note that this scattered field is known, since it is the difference between the total and background fields $\tilde{B}_1^{+;\mathrm{sc}}(\boldsymbol{x}) = \tilde{B}_1^+(\boldsymbol{x}) - \tilde{B}_1^{+;\mathrm{b}}(\boldsymbol{x})$ and the total $\tilde{B}_1^+$-field is known through measurements, while the background field $\tilde{B}_1^{+;\mathrm{b}}(\boldsymbol{x})$ is known through simulations. The real phase is generally not known in practice, and the transceive phase approximation is often used, which can lead to reconstruction artefacts at higher frequencies [29].

The second basic CSI-EPT equation, called the *object* or *state equation*, is obtained from the integral representation for the scattered electric field as given by the second equation of Equation (3.2). Using the definition of the scattered electric field $\tilde{\boldsymbol{E}}^{\mathrm{sc}} = \tilde{\boldsymbol{E}} - \tilde{\boldsymbol{E}}^{\mathrm{b}}$, this integral representation can be written as

$$\tilde{\boldsymbol{E}}(\boldsymbol{x}) - \int\limits_{\boldsymbol{x}' \in \mathbb{D}_{\mathrm{body}}} \underline{\tilde{\boldsymbol{G}}}^{\mathrm{EJ}}(\boldsymbol{x}, \boldsymbol{x}') \cdot \tilde{\boldsymbol{w}}(\boldsymbol{x}') \, \mathrm{d}V = \tilde{\boldsymbol{E}}^{\mathrm{b}}(\boldsymbol{x}) \quad (3.6)$$

and multiplying the above equation by the contrast function $\tilde{\chi}$ we arrive at

$$\tilde{\boldsymbol{w}}(\boldsymbol{x}) - \tilde{\chi}(\boldsymbol{x}) \int\limits_{\boldsymbol{x}' \in \mathbb{D}_{\mathrm{body}}} \underline{\tilde{\boldsymbol{G}}}^{\mathrm{EJ}}(\boldsymbol{x}, \boldsymbol{x}') \cdot \tilde{\boldsymbol{w}}(\boldsymbol{x}') \, \mathrm{d}V = \tilde{\chi}(\boldsymbol{x}) \tilde{\boldsymbol{E}}^{\mathrm{b}}(\boldsymbol{x}) \quad \text{for} \quad \boldsymbol{x} \in \mathbb{D}_{\mathrm{body}}, \quad (3.7)$$

which can be written more compactly as

$$\tilde{\boldsymbol{w}}(\boldsymbol{x}) - \tilde{\chi}(\boldsymbol{x}) \mathcal{G}_{\mathrm{body}}\{\tilde{\boldsymbol{w}}\} = \tilde{\chi}(\boldsymbol{x}) \tilde{\boldsymbol{E}}^{\mathrm{b}}(\boldsymbol{x}) \quad \text{for} \quad \boldsymbol{x} \in \mathbb{D}_{\mathrm{body}}, \quad (3.8)$$

where the linear operator $\mathcal{G}_{\text{body}}$ is implicitly defined in Equation (3.7). To summarize, the two fundamental unknowns in CSI-EPT are the contrast function $\tilde{\chi}$ and the contrast source $\tilde{w}$ and the basic CSI-EPT equations are the data equation (3.5) and the object equation (3.8).

Now suppose we have an approximation for the contrast function and contrast source available. We denote these approximants by $\hat{\chi}$ and $\hat{w}$, respectively, and in order to measure how well these approximations satisfy the data and object equations, we introduce the data and object residuals as

$$\tilde{r}_{\text{d}}(\boldsymbol{x}) = \tilde{B}_1^{+;\text{sc}}(\boldsymbol{x}) - \mathcal{G}_{\text{data}}\{\hat{w}\}(\boldsymbol{x}) \quad \text{for} \quad \boldsymbol{x} \in \mathbb{D}_{\text{body}}, \tag{3.9}$$

and

$$\tilde{\boldsymbol{r}}_{\text{o}}(\boldsymbol{x}) = \hat{\chi}(\boldsymbol{x})\tilde{\boldsymbol{E}}^{\text{b}}(\boldsymbol{x}) - \hat{w}(\boldsymbol{x}) + \hat{\chi}(\boldsymbol{x})\mathcal{G}_{\text{body}}\{\hat{w}\}(\boldsymbol{x}) \quad \text{for} \quad \boldsymbol{x} \in \mathbb{D}_{\text{body}}, \tag{3.10}$$

respectively, and measure their magnitudes using the L_2-norms

$$\|\tilde{r}_{\text{d}}\|^2_{\text{body}} = \int\limits_{\boldsymbol{x}\in\mathbb{D}_{\text{body}}} |\tilde{r}_{\text{d}}(\boldsymbol{x})|^2 \, \text{d}V \quad \text{and} \quad \|\tilde{\boldsymbol{r}}_{\text{o}}\|^2_{\text{body}} = \int\limits_{\boldsymbol{x}\in\mathbb{D}_{\text{body}}} |\tilde{\boldsymbol{r}}_{\text{o}}(\boldsymbol{x})|^2 \, \text{d}V. \tag{3.11}$$

In CSI-EPT, these norms are used to define the objective function

$$F(\hat{\chi}, \hat{w}) = \frac{\|\tilde{r}_{\text{d}}\|^2_{\text{body}}}{\left\|\tilde{B}_1^{+;\text{sc}}\right\|^2_{\text{body}}} + \frac{\|\tilde{\boldsymbol{r}}_{\text{o}}\|^2_{\text{body}}}{\left\|\hat{\chi}\tilde{\boldsymbol{E}}^{\text{b}}\right\|^2_{\text{body}}} \tag{3.12}$$

and the goal is to find a contrast function and contrast source that minimizes this objective function. We note that including the 2-norm of the object residual in the objective function (second term on the right-hand side of Equation (3.12)) is crucial to the success of CSI, since it has been shown that a contrast source inversion approach without this term produces unsatisfactory results in general [25].

In CSI-EPT, finding the desired contrast function is now realized by minimizing the objective function in a "fix-one-minimize-for-the-other" (alternating direction method) approach. The iterative process is continued until a predefined maximum number of iterations or specified tolerance level of the objective function has been reached. Specifically, the basic CSI-EPT algorithm is as shown in Algorithm 2. Polak-Ribière update directions are usually taken for the update direction $v^{[k]}$ in Step 1 of the algorithm, but Fletcher-Reeves or Hesteness-Stiefel update directions may be used as well. To determine these update directions, the gradient of the cost function $F(\hat{\chi}^{[k-1]}, \hat{w})$ with respect to $\hat{w}$ at $\hat{w} = \hat{w}^{[k-1]}$ is required. Explicit expressions for this gradient and the corresponding step length $\alpha^{[k]}$ can be found in [24], for example.

Also, note that with Equation (3.6), the object residual can be written as $\tilde{\boldsymbol{r}}_{\text{o}} = \hat{\chi}\hat{\boldsymbol{E}} - \hat{w}$ and in Steps 2 and 3 we find the minimum-norm contrast function $\hat{\chi}$ for which $\|\tilde{\boldsymbol{r}}_{\text{o}}\|^2_{\text{body}}$ is minimized. This contrast function is generally sensitive to small perturbations in $\hat{w}$ at locations where the magnitude of the electric field strength is

Algorithm 2 contrast source inversion — EPT (CSI-EPT).

- Given initial guesses $\hat{\chi}^{[0]}$ and $\hat{\boldsymbol{w}}^{[0]}$ for the contrast function and contrast source, respectively
- For $k = 1, 2, \ldots$
  1. Fix the contrast to $\hat{\chi}^{[k-1]}$ and update the contrast source according to the update formula
  $$\hat{\boldsymbol{w}}^{[k]} = \hat{\boldsymbol{w}}^{[k-1]} + \alpha^{[k]} \boldsymbol{v}^{[k]}.$$
  2. Compute the corresponding electric field strength $\hat{\boldsymbol{E}}^{[k]}$ according to (cf. Equation (3.6))
  $$\hat{\boldsymbol{E}}^{[k]}(\boldsymbol{x}) = \tilde{\boldsymbol{E}}^{\mathrm{b}}(\boldsymbol{x}) + \mathcal{G}_{\mathrm{body}}\{\hat{\boldsymbol{w}}^{[k]}\}(\boldsymbol{x}).$$
  3. Knowing the contrast source $\hat{\boldsymbol{w}}^{[k]}$ and the corresponding electric field strength $\hat{\boldsymbol{E}}^{[k]}$, determine the contrast function $\hat{\chi}^{[k]}$ from the constitutive relation $\hat{\boldsymbol{w}}^{[k]} = \hat{\chi}^{[k]} \hat{\boldsymbol{E}}^{[k]}$ by solving the least-squares problem $\left\| \hat{\chi} \hat{\boldsymbol{E}}^{[k]} - \hat{\boldsymbol{w}}^{[k]} \right\|^2_{\mathrm{body}}$ for the minimum norm contrast function $\hat{\chi}$.
  4. Stop if objective function is smaller than user specified tolerance level, or if maximum number of iterations has been reached.
- End

"small." To suppress this effect, we can update the contrast function at every iteration according to the update formula

$$\hat{\chi}^{[k]} = \hat{\chi}^{[k-1]} + \beta^{[k]} u^{[k]}, \tag{3.13}$$

with $u^{[k]}$ the Polak-Ribière update direction for the contrast function and $\beta^{[k]}$ its corresponding update coefficient. Such an approach usually has a regularizing effect and typically leads to smoother reconstructions.

3.2.1. The Object and Data Operators for Three-Dimensional CSI-EPT

In three dimensions and with air as a background medium, the integral representations for the scattered fields as given by Equation (3.2) take on the form

$$\tilde{\boldsymbol{B}}^{\mathrm{sc}}(\boldsymbol{x}) = \mathrm{j} \frac{\omega}{c_0^2} \nabla \times \tilde{\boldsymbol{A}}^{\mathrm{sc}}(\boldsymbol{x}) \quad \text{and} \quad \tilde{\boldsymbol{E}}^{\mathrm{sc}}(\boldsymbol{x}) = (k_0^2 + \nabla\nabla\cdot)\tilde{\boldsymbol{A}}^{\mathrm{sc}}(\boldsymbol{x}), \tag{3.14}$$

where c_0 is the electromagnetic wave speed in vacuum, $k_0 = \omega/c_0$ the wave number in vacuum, and $\tilde{\boldsymbol{A}}^{\text{sc}}$ is the vector potential given by

$$\tilde{\boldsymbol{A}}^{\text{sc}}(\boldsymbol{x}) = \int_{\boldsymbol{x}' \in \mathbb{D}_{\text{body}}} \tilde{G}(\boldsymbol{x} - \boldsymbol{x}') \tilde{\boldsymbol{w}}(\boldsymbol{x}') \, \mathrm{d}V, \tag{3.15}$$

with $\tilde{G}$ the three-dimensional Green's function of the vacuum background domain given by

$$\tilde{G}(\boldsymbol{x}) = \frac{\exp(-\mathrm{j} k_0 |\boldsymbol{x}|)}{4\pi |\boldsymbol{x}|}. \tag{3.16}$$

Note that the nabla-operators act on the position vector $\boldsymbol{x}$ and not on the integration variable $\boldsymbol{x}'$. The 3-D object operator $\mathcal{G}_{\text{body}}$ can be easily identified from the second equation in (3.14). For the data operator $\mathcal{G}_{\text{data}}$, however, we have to substitute the x- and y-components of the scattered magnetic flux density in Equation (3.4) to obtain

$$\tilde{B}_1^{+;\text{sc}} = \frac{\omega}{c_0^2} \left(\partial^+ \tilde{A}_z^{\text{sc}} - \partial_z \tilde{A}^{+;\text{sc}} \right), \tag{3.17}$$

where $\partial^+ = \frac{1}{2}(\partial_x + \mathrm{j}\partial_y)$ and $\tilde{A}^{+;\text{sc}} = \frac{1}{2}(\tilde{A}_x^{\text{sc}} + \mathrm{j}\tilde{A}_y^{+;\text{sc}})$. From the above expression for the scattered $\tilde{B}_1^+$-field, the 3-D data operator $\mathcal{G}_{\text{data}}$ can be identified. Note the particular structure of this operator: the scattered $\tilde{B}_1^+$-field originates from a difference between the transverse variations of the longitudinal vector potential ($\partial^+ \tilde{A}_z^{\text{sc}}$) and the longitudinal variations of the transverse vector potential ($\partial_z \tilde{A}^{+;\text{sc}}$).

3.2.2. The Object and Data Operators for Two-Dimensional CSI-EPT

In various papers (see [26], for example) it has been reported that the radio frequency (RF) field in the midplane of a birdcage coil is essentially E-polarized, meaning that the electric field strength has a longitudinal component only ($\tilde{\boldsymbol{E}} = \tilde{E}_z \hat{\boldsymbol{\imath}}_z$), while the magnetic flux density has only x- and y-components ($\tilde{\boldsymbol{B}} = \tilde{B}_x \hat{\boldsymbol{\imath}}_x + \tilde{B}_y \hat{\boldsymbol{\imath}}_y$). Additionally, in a two-dimensional configuration that is invariant in the z-direction, external electric current densities with longitudinal components only generate E-polarized fields. Identifying the currents in the rungs of the birdcage coil with these z-directed external current sources and denoting the slice through the object that coincides with the midplane of the birdcage coil by $\mathbb{S}_{\text{body}}$, it makes sense to assume that within this midplane the RF field is essentially two-dimensional and E-polarized with integral representations for the scattered fields given by

$$\tilde{\boldsymbol{B}}^{\text{sc}}(\boldsymbol{\rho}) = \mathrm{j} \frac{\omega}{c_0^2} \nabla_{\text{T}} \times \tilde{\boldsymbol{A}}^{\text{sc}}(\boldsymbol{\rho}), \quad \text{and} \quad \tilde{\boldsymbol{E}}^{\text{sc}}(\boldsymbol{\rho}) = k_0^2 \tilde{\boldsymbol{A}}^{\text{sc}}(\boldsymbol{\rho}), \tag{3.18}$$

where $\boldsymbol{\rho}$ is the position vector in the midplane of the birdcage coil, $\nabla_{\text{T}} = \hat{\boldsymbol{\imath}}_x \partial_x + \hat{\boldsymbol{\imath}}_y \partial_y$ is the transverse nabla-operator, and

$$\tilde{\boldsymbol{A}}^{\text{sc}}(\boldsymbol{\rho}) = \int_{\boldsymbol{\rho}' \in \mathbb{S}_{\text{body}}} \tilde{G}(\boldsymbol{\rho} - \boldsymbol{\rho}') \tilde{\boldsymbol{w}}(\boldsymbol{\rho}') \, \mathrm{d}S \tag{3.19}$$

is the vector potential in two dimensions (and is therefore expressed as a two-dimensional integral as opposed to the three-dimensional integral in the 3-D case) with

$$\tilde{G}(\boldsymbol{\rho}) = -\frac{\mathrm{j}}{4} H_0^{(2)}(k_0 |\boldsymbol{\rho}|) \tag{3.20}$$

the Green's function of the two-dimensional homogeneous background medium (air) and $H_0^{(2)}$ is the Hankel function of the second kind and order zero. In this two-dimensional case, the object operator $\mathcal{G}_{\text{body}}$ can be easily identified from the second equation of (3.18) and does not contain a gradient-divergence operator as in the three-dimensional case. For the 2-D data operator $\mathcal{G}_{\text{data}}$, we have to substitute the x- and y-components of the magnetic flux density as given by the first equation of (3.18) in the definition of the $\tilde{B}_1^+$-field to obtain

$$\tilde{B}_1^{+;\text{sc}} = \frac{\omega}{c_0^2} \partial^+ \tilde{A}_z^{\text{sc}}. \tag{3.21}$$

From this expression, the 2-D data operator $\mathcal{G}_{\text{data}}$ can now easily be identified. Comparing the two-dimensional field representation of Equation (3.21) with their three-dimensional counterpart of Equation (3.17), we observe that longitudinal spatial variations are absent in the two-dimensional case. Moreover, the vector potentials in both expressions are different as well, since this quantity is computed using Equation (3.19) in the two-dimensional case, while the three-dimensional vector potential is given by Equation (3.15). The differences between two- and three-dimensional CSI-EPT reconstructions will be discussed in more depth in Section 3.3.

3.2.3. Two-Dimensional CSI-EPT Simplified–First-Order Induced Current EPT (foIC-EPT)

In two dimensions, the CSI-EPT algorithm can be simplified by exploiting the particular structure of E-polarized RF fields. To make this simplification explicit, we first introduce the differentiation operator $\partial^- = \frac{1}{2}(\partial_x - \mathrm{j}\partial_y)$ and note that the operators ∂^- and ∂^+ essentially factor the two-dimensional Laplacian $\Delta = \partial_x^2 + \partial_y^2$ as

$$\Delta = 4\partial^-\partial^+ = 4\partial^+\partial^-. \tag{3.22}$$

Now as a first step, we substitute the second equation of ((3.18)) in Equation (3.21) to obtain

$$\tilde{B}_1^{+;\text{sc}}(\boldsymbol{\rho}) = \frac{1}{\omega} \partial^+ \tilde{E}_z^{\text{sc}}(\boldsymbol{\rho}). \tag{3.23}$$

Subsequently, we use the definition of the scattered fields to write the above expression as

$$\tilde{B}_1^{+}(\boldsymbol{\rho}) = \tilde{B}_1^{+;\text{b}}(\boldsymbol{\rho}) + \frac{1}{\omega} \partial^+ \tilde{E}_z(\boldsymbol{\rho}) - \frac{1}{\omega} \partial^+ \tilde{E}_z^{\text{b}}(\boldsymbol{\rho}) \tag{3.24}$$

and since $\tilde{B}_1^{+;\text{b}}(\boldsymbol{\rho}) = \frac{1}{\omega} \partial^+ \tilde{E}_z^{\text{b}}(\boldsymbol{\rho})$, this simplifies to

$$\tilde{B}_1^{+}(\boldsymbol{\rho}) = \frac{1}{\omega} \partial^+ \tilde{E}_z(\boldsymbol{\rho}). \tag{3.25}$$

Algorithm 3 First-Order Induced Current EPT Algorithm (foIC-EPT).

- Given the measured $\tilde{B}_1^+$-field in the midplane of the birdcage coil:
  1. Determine the induced current density using Equation (3.28).
  2. Determine the corresponding electric field strength by solving a specific integral equation (Equation (2.12)).
  3. Knowing the induced current density and the electric field strength, determine the conductivity and permittivity profiles using Equation (3.27).

If we now act with the ∂^- operator on this equation, we obtain

$$\partial^- \tilde{B}_1^+ = \frac{1}{4\omega} \Delta \tilde{E}_z \tag{3.26}$$

and since $\tilde{E}_z$ satisfies $\Delta \tilde{E}_z - \mathrm{j}\omega\mu_0 \tilde{J}_z^{\mathrm{ind}} = 0$ with

$$\tilde{J}_z^{\mathrm{ind}} = (\sigma + \mathrm{j}\omega\varepsilon)\tilde{E}_z, \tag{3.27}$$

we arrive at

$$\tilde{J}_z^{\mathrm{ind}} = \frac{4}{\mathrm{j}\mu_0} \partial^- \tilde{B}_1^+. \tag{3.28}$$

This last equation shows that in two dimensions, the induced current density is obtained (accounting for multiplication by $4/\mathrm{j}\mu_0$) by acting with the ∂^- operator on the total B_1^+-field. The simplified CSI-EPT method is therefore called a first-order induced current EPT method, since a first-order differentiation of the B_1^+-field essentially immediately results in an image of the induced current density.

As shown in [21], after the induced current density has been obtained, the corresponding electric field strength can be computed by solving a specific integral equation defined on $\mathbb{S}_{\mathrm{body}}$. With the electric field strength now known, the conductivity and permittivity profiles within the slice can be obtained from Equation (3.27). The overall first-order induced current density EPT algorithm can be summarized as presented in Algorithm 3. More details on this algorithm can be found in [21]. Finally, we note that the above algorithm is a direct non-iterative EPT method and, as opposed to CSI-EPT, requires the solution of a system of equations (Step 2) to arrive at the reconstructed conductivity and permittivity profiles. Fortunately, as demonstrated in [21], this system of equations can be solved efficiently using iterative solvers such as the generalized minimal residual solver (GMRES) [30] and typically only a few iterations are required to reach a prescribed error.

3.3. Methods and Results

To illustrate the performance of foIC-EPT and two- and three-dimensional CSI-EPT, we reconstruct the conductivity and permittivity profiles of the head of the anatomical

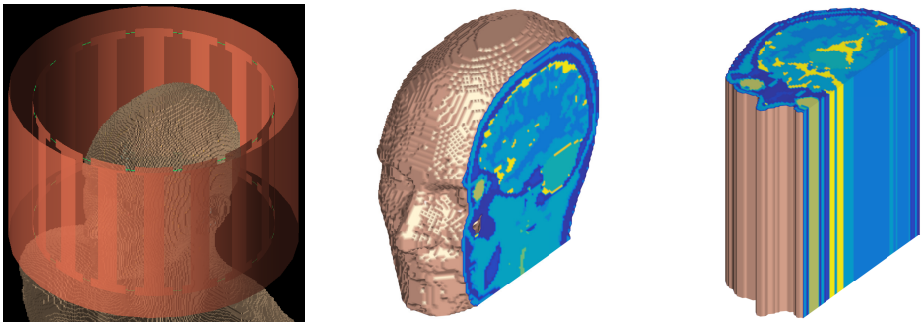

(a) (b) (c)

Figure 3.1: Birdcage coil and head models. The high-pass birdcage coil with the head model placed inside (a), the Duke head model from the Virtual Family [28] (b), and a longitudinally uniform head model obtained by repeating the center slice in the longitudinal direction (c).

human body model Duke from the Virtual Family [28] (see the Figures 3.1a and 3.1b), from noise-free $\tilde{B}_1^+$-data. The head model consists of $124 \times 100 \times 109$ isotropic voxels with side lengths of 2 mm. The model is placed inside an ideal high-pass birdcage coil (see Figure 3.1a) consisting of 16 rungs each having a width of 25 mm. The coil has a radius of 150 mm, is 195 mm long, and is driven in quadrature at 128 MHz, which corresponds to the operating frequency of a 3 T magnetic resonance imaging (MRI) system. The shield surrounding the coil has a radius of 180 mm and a length of 200 mm. Commercial EM simulation software (XFdtd, v.7.5, Remcom State College, PA, USA) is used to obtain the background field $\left\{\tilde{\boldsymbol{E}}^{\mathrm{b}}, \tilde{\boldsymbol{B}}^{\mathrm{b}}\right\}$ as generated by the high-pass birdcage coil. Finally, to investigate the difference between two- and three-dimensional conductivity and permittivity reconstructions, we also consider a longitudinally uniform "head model" in which the center slice is simply repeated in the longitudinal direction thereby creating a model with no variations in the longitudinal z-direction within the head (see Figure 3.1c).

3.3.1. Two-Dimensional CSI-EPT and foIC-EPT

The CSI-EPT method was originally implemented for two-dimensional configurations in [14] to study its potential as an EPT reconstruction method and to test if the method can handle strongly inhomogeneous tissue profiles. Let us therefore start with a purely two-dimensional, noise free, reconstruction problem in which we attempt to reconstruct the conductivity and permittivity profiles within the center slice of the head model shown in Figure 3.2a. In this two-dimensional setting, we take the background field in the midplane of the realistic birdcage coil shown in Figure 3.1a as the 2-D background field. The reconstructed conductivity and permittivity profiles obtained after 5000 iterations of the two-dimensional CSI-EPT method are shown in Figure 3.2b. It takes the algorithm approximately 86 seconds on an Intel i7–6700 CPU operating on Windows 7 with Matlab 2016a to arrive at these reconstructions, and we terminate the algorithm after 5000 iterations, since the objective function has already

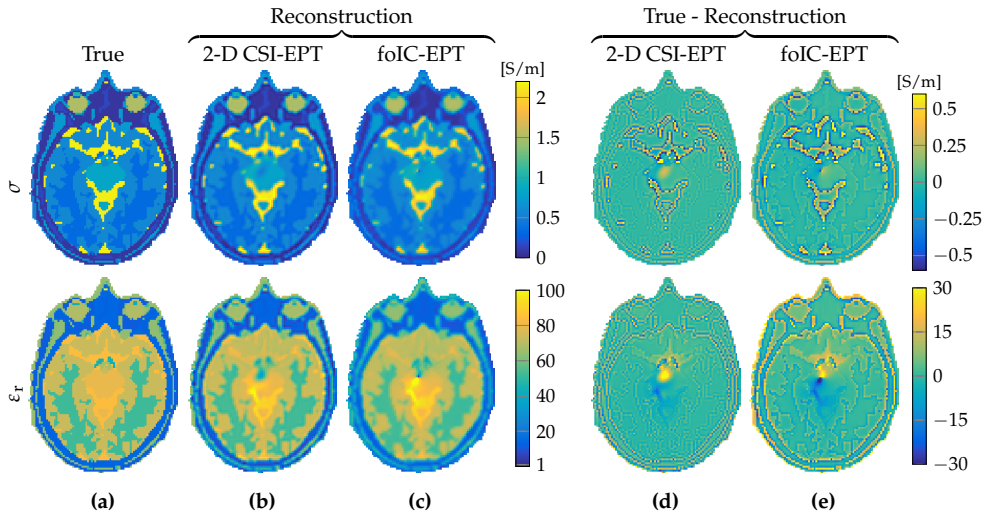

Figure 3.2: Reconstruction results from 2-D reconstruction methods on noise free data. The true model (a), the reconstruction obtained after 5000 iterations of 2-D CSI-EPT (b) and the reconstruction from foIC-EPT (c). The respective errors are shown in (d, e). Top row shows the conductivity and the bottom row the relative permittivity.

dropped below a 1.53×10^{-5} tolerance level at this point and essentially no significant improvements are obtained. In addition, the foIC-EPT reconstruction profiles of the conductivity and permittivity are shown in Figure 3.2c and the errors of CSI-EPT and foIC-EPT conductivity and permittivity reconstructions are shown in Figures 3.2d and 3.2e, respectively. We observe that the quality of the foIC-EPT reconstructions is similar to CSI-EPT even though it takes foIC-EPT only a fraction of a second to produce these reconstructions (see Table 3.1 for details).

3.3.2. Three-Dimensional CSI-EPT

In a two-dimensional approach, the RF field is an E-polarized field with an electric field strength that is longitudinal ($\tilde{\boldsymbol{E}} = \tilde{E}_z \hat{\boldsymbol{\imath}}_z$) and a magnetic flux density that is transverse ($\tilde{\boldsymbol{B}} = \tilde{B}_x \hat{\boldsymbol{\imath}}_x + \tilde{B}_y \hat{\boldsymbol{\imath}}_y$). Such an approach has been shown to be reasonable for a homogeneous cylindrical phantom in a central region of a body coil consisting of elementary center-fed dipole antennas in [26], and indeed, when the longitudinal uniform head model of Figure 3.1c is placed within our birdcage coil we also observe that the x- and y- components of the electric field strength in the central transverse slice are small compared to its z-component as illustrated in the top rows of Figures 3.3a-c and Figures 3.4a-b.

However, as we move away from the center slice in the longitudinally uniform head model of Figure 3.1c, the magnitude of the x- and y-components of the electric field strength starts to increase as illustrated in the top rows of Figures 3.3d-f and Figures 3.4c-d, where the magnitude of the electric field strength components is shown in a slice located 5 cm above the central slice. We observe that even though the

Table 3.1: The mean and standard deviation of the reconstructed electrical properties in the different tissues that are apparent in the center slice of the head models using 2-D CSI-EPT and foIC-EPT in a two-dimensional setting. Units of σ and ε_r are in siemens per meter and permittivity of free space, respectively.

	Conductivity (σ)		
	True	2-D CSI-EPT	foIC-EPT
Fat	0.07	0.13±0.10	0.18±0.10
Red marrow	0.16	0.11±0.06	0.15±0.03
Bone	0.07	0.14±0.15	0.21±0.14
Eye lens	0.31	0.54±0.11	0.78±0.09
Nerve	0.35	0.74±0.30	0.77±0.26
Connective tissue	0.50	0.47±0.12	0.44±0.13
White matter	0.34	0.36±0.04	0.38±0.04
Muscle	0.72	0.63±0.11	0.55±0.13
Eye sclera	0.92	0.89±0.15	0.87±0.13
Skin	0.52	0.48±0.08	0.36±0.09
Hypothalamus	0.80	0.88±0.11	0.91±0.11
Eye vitreous humor	1.51	1.46±0.13	1.40±0.15
Cornea	1.06	0.92±0.13	0.83±0.11
Gray matter	0.59	0.61±0.15	0.63±0.15
Midbrain	0.83	0.84±0.17	0.88±0.18
Cerebrospinal fluid	2.14	1.90±0.29	1.75±0.29
Mucosa	2.28	1.50±0.03	1.01±0.02
	Relative permittivity (ε_r)		
Fat	12.37	17.23±7.89	19.27±7.15
Red marrow	13.54	11.08±2.52	13.68±1.47
Bone	14.72	19.09±8.05	21.73±6.90
Eye lens	42.79	48.86±5.26	51.52±1.44
Nerve	44.07	51.49±8.74	47.33±7.42
Connective tissue	51.86	46.48±7.56	40.54±7.06
White matter	52.53	54.33±3.12	55.37±3.54
Muscle	63.49	56.76±7.28	48.30±8.72
Eye sclera	65.00	56.78±6.67	50.26±5.95
Skin	65.44	59.00±8.95	42.29±8.55
Hypothalamus	66.78	59.48±4.91	54.12±4.20
Eye vitreous humor	69.06	66.19±4.86	61.03±4.95
Cornea	71.46	61.52±9.32	52.81±5.84
Gray matter	73.52	72.68±4.18	70.54±4.92
Midbrain	79.74	78.58±10.24	81.93±12.33
Cerebrospinal fluid	84.04	80.66±8.57	76.46±11.31
Mucosa	116.00	78.07±5.17	53.83±2.77

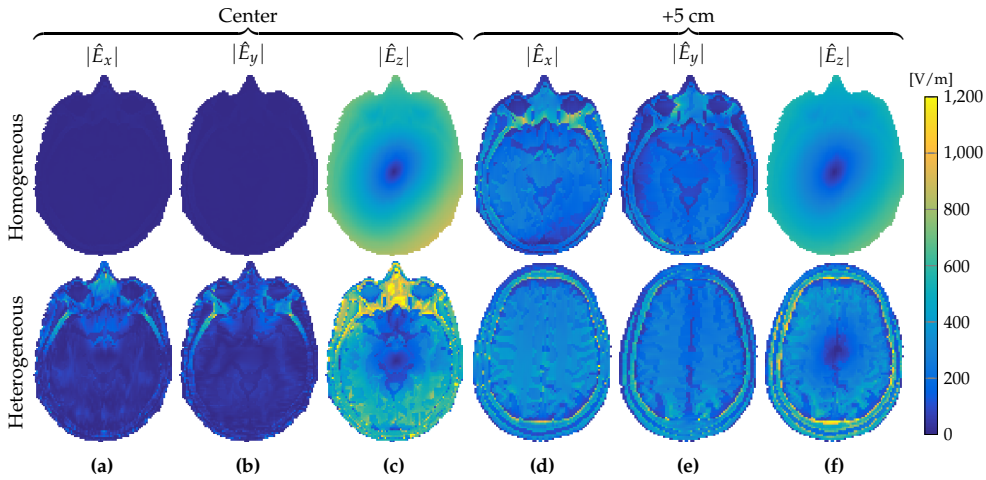

Figure 3.3: The magnitude of the electric field strength components. The x-, y- and z-component at the transversal midplane (a-c) and at the slice 5 cm higher (d-f), respectively. The top and bottom row show the fields in the case of a longitudinal homogeneous and heterogeneous object, respectively.

transverse components of the electric field strength are negligible within the center slice, they can no longer be neglected 5 cm away from it.

Furthermore, for the realistic heterogeneous head model of Figure 3.1b a two-dimensional E-polarized field assumption completely fails as shown in the bottom rows of Figures 3.3a-f and 3.4a-d. In the slice 5 cm above the central slice and even within the central slice itself the x- and y-components of the electric field strength can no longer be neglected and have to be taken into account in the full Maxwell equations to properly describe RF field behavior within the head model.

To study the effects of longitudinal spatial variations of the tissue parameters on the $\tilde{B}_1^+$-field, we consider Equation (3.17) again and write it in the form

$$\tilde{B}_1^{+;\mathrm{sc}} = \mathcal{B}^{\mathrm{tra}} + \mathcal{B}^{\mathrm{lon}}, \tag{3.29}$$

where $\mathcal{B}^{\mathrm{tra}} = (\omega/c_0^2)\partial^+ \tilde{A}_z^{\mathrm{sc}}$ and $\mathcal{B}^{\mathrm{lon}} = -(\omega/c_0^2)\partial_z \tilde{A}^{+;\mathrm{sc}}$. The longitudinal variation term $\mathcal{B}^{\mathrm{lon}}$ is absent in a 2-D approach (see Equation (3.21)), since in a 2-D setting the configuration is assumed to be invariant in the longitudinal z-direction ($\partial_z = 0$). Figure 3.5, however, shows that for both the longitudinally homogeneous and realistic heterogeneous head model the longitudinal variation term is significant and cannot be ignored. Especially near the periphery of both head models, $\mathcal{B}^{\mathrm{lon}}$ contributes to the scattered $\tilde{B}_1^+$-field. More specifically, within a 1 cm outer boundary layer located in the center slice, the mean of the fraction $\left|\mathcal{B}^{\mathrm{lon}}/\tilde{B}_1^{+;\mathrm{sc}}\right|$ is 1.18 and 1.25 for the homogeneous and inhomogeneous head model, respectively, while in the inner region these means are 0.51 and 0.60 and similar averages are obtained for the slice located 5 cm above the center slice. From these observations, it is clear that longitudinal variations of the transverse vector potential $\tilde{A}^{+;\mathrm{sc}}$ contribute to the scattered $\tilde{B}_1^+$-field and cannot be ignored.

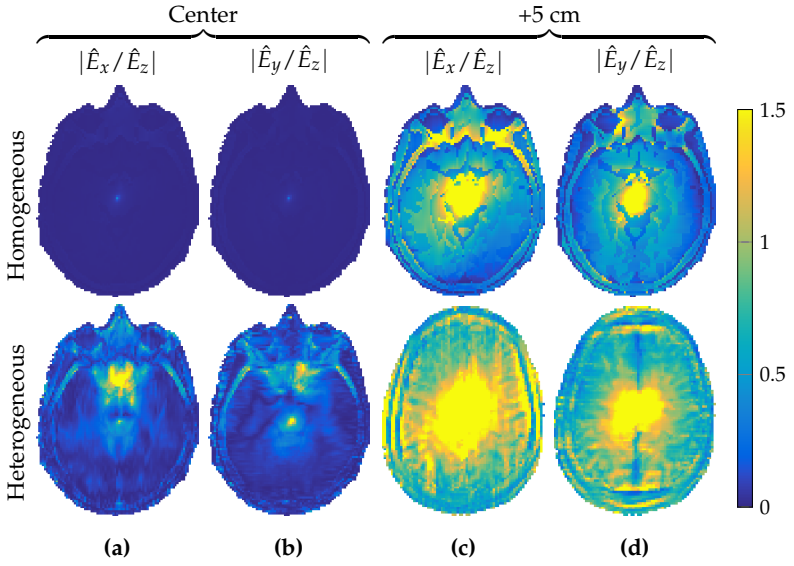

Figure 3.4: Ratios of the x- and y-components of the electric field strength relative to its z-component. The relative field components at the center slice (a,b) and at the slice 5 cm higher (c,d). The top row is for the longitudinally uniform object, the bottom row for the object with longitudinal variations.

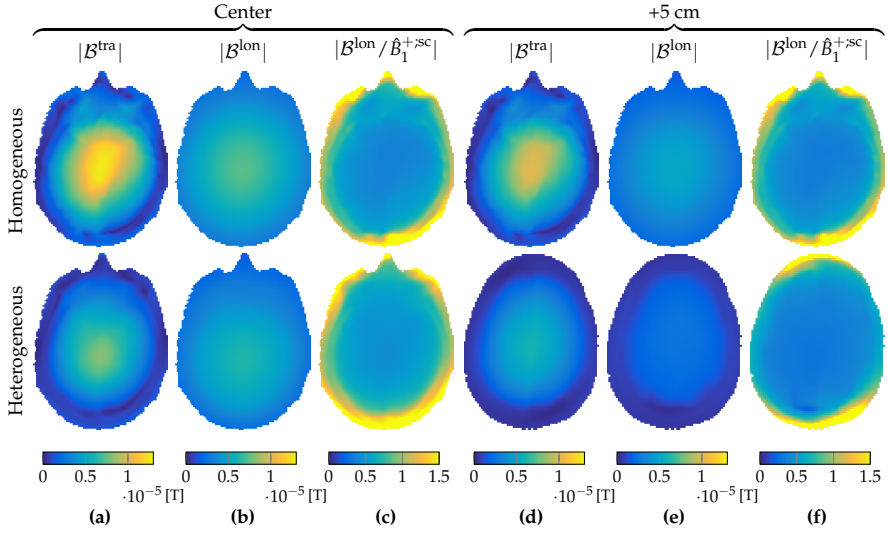

Figure 3.5: Magnitude of the scattered $\tilde{B}_1^+$ terms. The transverse variation (a) and longitudinal variation term of the scattered $\tilde{B}_1^+$ (b) and the contributions of $\mathcal{B}^{\mathrm{lon}}$ w.r.t. $\tilde{B}_1^{+,\mathrm{sc}}$ (c) at the center slice. (d-f) show respectively the same at a slice 5 cm higher in the head domain. Top row shows in the case of a longitudinally uniform object, the bottom row for the head model with longitudinal variations. (b) and (e) are neglected in the 2-D approach.

Up to this point, we have compared 3-D RF field structures with their 2-D counterparts for a longitudinally uniform and a realistic heterogeneous head model. In a two-dimensional configuration, however, the sources are invariant in the longitudinal direction as well, and we expect that due to the finite extent of the birdcage coil additional deviations in the $\tilde{B}_1^+$ fields will be observed.

To investigate this issue further, we first determine the two-dimensional $\tilde{B}_1^+$-field in the central slice as described in Section 3.3.1. The magnitude and phase of this field are shown in the top and bottom row of Figure 3.6a, respectively. Subsequently, we consider RF excitation by the 3-D birdcage coil, but assume that the birdcage coil, including its currents, does not vary in the longitudinal direction. For the longitudinally uniform head model, a $\tilde{B}_1^+$-field as shown in Figure 3.6b is then obtained, and we observe that this field strongly resembles the 2-D $\tilde{B}_1^+$-field pattern of Figure 3.6a. Replacing the longitudinal invariant currents in the rungs by the exact current, but keeping the homogeneous head model, we obtain the $\tilde{B}_1^+$-field pattern shown in Figure 3.6c. The agreement with the 2-D field $\tilde{B}_1^+$-field pattern clearly deteriorates and this correspondence becomes even worse for the realistic longitudinal heterogeneous head model as shown in Figure 3.6d. Since the $\tilde{B}_1^+$-field is used as an input for the CSI-EPT method, an accurate correspondence is obviously necessary for a proper reconstruction. The 2-D CSI-EPT algorithm expects a 2-D $\tilde{B}_1^+$-field as shown in Figure 3.6a for the center head slice, but in 3-D the $\tilde{B}_1^+$-field from Figure 3.6d is present and providing this 3-D field as an input to a 2-D CSI-EPT algorithm will lead to inaccurate reconstructions in general.

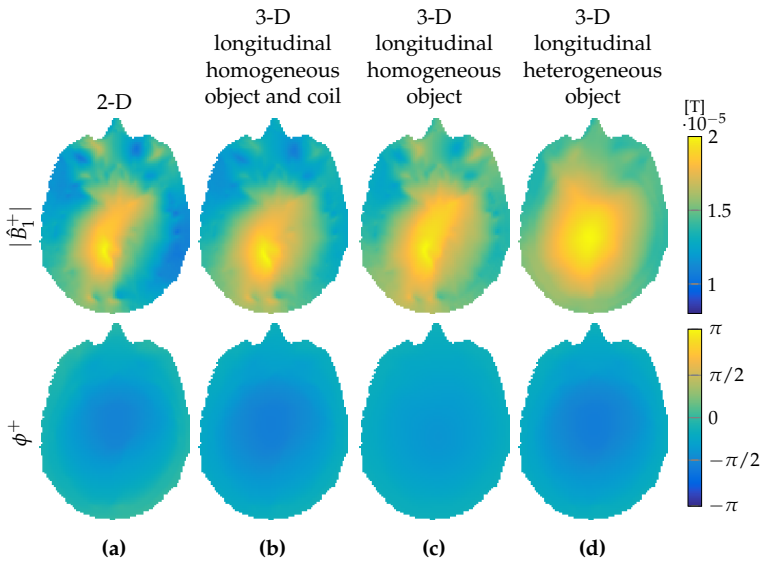

Figure 3.6: $\tilde{B}_1^+$ field comparison. The total $\tilde{B}_1^+$ field assumed in the 2-D setting (a), the total $\tilde{B}_1^+$ field obtained in a 3-D setting with longitudinal homogeneity of the object and coil (b), of longitudinal homogeneity of only the object (c) and with longitudinal variations of also the object (d). Top row shows the $\tilde{B}_1^+$ magnitude, the bottom row the $\tilde{B}_1^+$ phase.

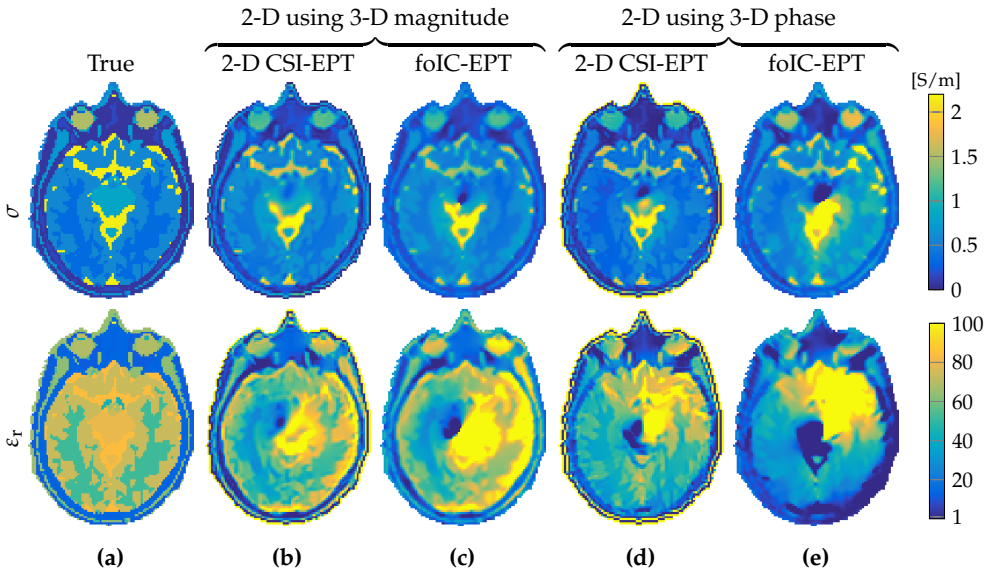

Figure 3.7: Reconstruction results from 2-D reconstruction methods using parts of 3-D $\tilde{B}_1^+$ data. True model (a), reconstruction results assuming 2-D phase with 3-D magnitude (b,c), and reconstruction results assuming 2-D magnitude with 3-D phase (d,e) of the $\tilde{B}_1^+$-field in the central transverse slice from simulations with the longitudinal invariant head model. Top row shows the conductivity and the bottom row the relative permittivity.

To illustrate how these differences in actual fields (3-D) and expected fields (2-D) translate to reconstruction errors, both two-dimensional algorithms have been applied to quasi three-dimensional data using either 3-D amplitudes or phases. Note that, in order to match 2-D and 3-D data, the maximum absolute value of the $\tilde{B}_1^+$-field of both datasets is taken to be equal. The results are depicted in Figure 3.7b-e from which it can be observed that particularly the permittivity is sensitive to 2-D violations. This reconstruction difference between conductivity and permittivity is due to the fact that conduction currents ($\sigma\hat{\boldsymbol{E}}$) influence the $\tilde{B}_1^+$-field to a much larger extent than the displacement currents ($\mathrm{j}\omega\varepsilon\hat{\boldsymbol{E}}$) at 3 T.

The reconstructions of the conductivity and relative permittivity profiles for the full 3-D case without any further assumptions, using 3-D magnitude as well as 3-D phase $\tilde{B}_1^+$ data are shown for the longitudinally uniform model in Figures 3.8a-f and for the realistic heterogeneous head model in Figure 3.8g-l. Reconstructions are shown for the central slice profiles as well as for the profiles located within the slice positioned 5 cm above the central slice. For comparison, 2-D CSI-EPT reconstructions based on 3-D $\tilde{B}_1^+$ data are also presented. The relative residual error (norm of the difference between the exact and reconstructed profile normalized by the norm of the exact profile, where the norm is taken over the center slice) of Figure 3.8h is 0.7339 and 0.8263 for the conductivity and permittivity, respectively, while the relative residual error of the conductivity and permittivity of Figure 3.8i is 0.3358 and 0.1587, respectively. Clearly, 2-D CSI-EPT is unable to accurately reconstruct the conductivity and permittivity profiles. The 2-D and 3-D permittivity reconstructions are also less ac-

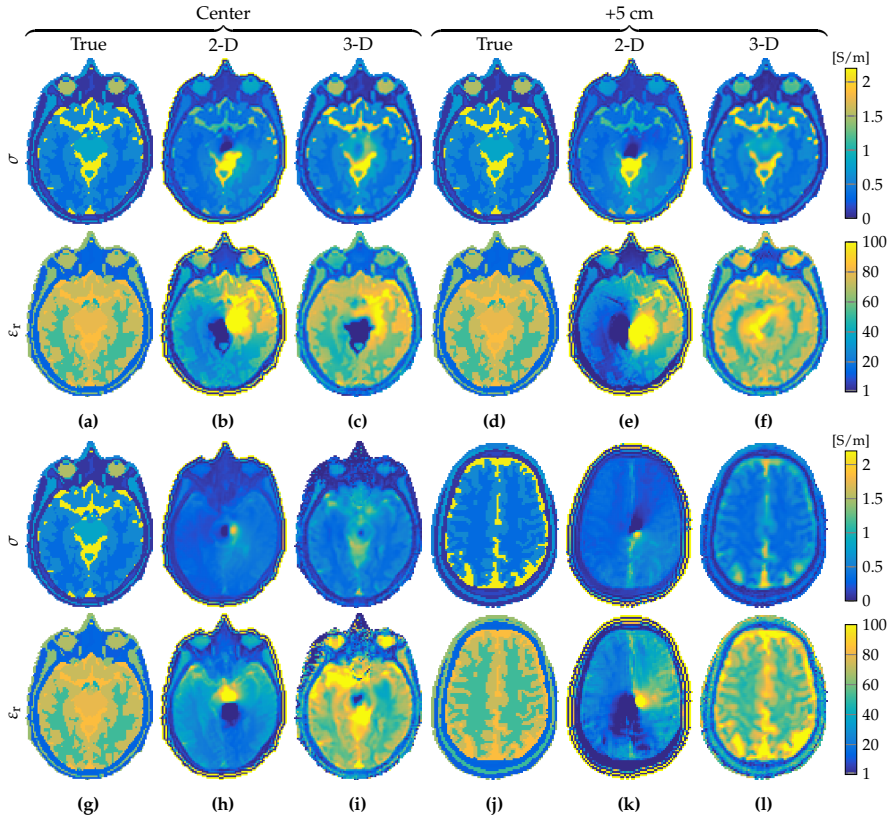

Figure 3.8: Reconstruction comparison of 2-D and 3-D CSI-EPT on 3-D $\tilde{B}_1^+$ fields after 5000 and 50000 iterations, respectively. (a-c) show the true object, the reconstruction with 2-D CSI-EPT and the reconstruction with 3-D CSI-EPT for a homogeneous object and for the center slice. (d-f) show respectively the same, but for a slice five centimeter higher. (g-l) show respectively the same as (a-f), but in the case of a longitudinal inhomogeneous object. The top row depicts the conductivity, the bottom row the permittivity.

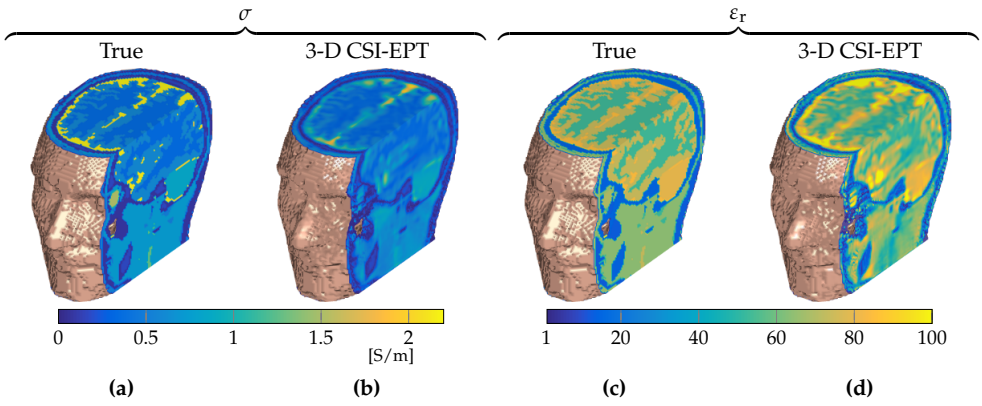

Figure 3.9: Three-dimensional visualization of a section of the 3-D CSI-EPT reconstruction of the heterogeneous Duke head model (Figure 3.1b) after 50000 iterations. The true and reconstructed conductivity (a,b) and the true and reconstructed relative permittivity (c, d). The top slice that is visible is the slice 5 cm above the transverse midplane.

curate than the conductivity reconstructions, indicating that $\tilde{B}_1^+$-field data acquired at 3 T is less sensitive to permittivity variations.

Finally, to emphasize that 3-D CSI-EPT is a fully three-dimensional volumetric reconstruction method, we present a full 3-D CSI-EPT reconstruction of the realistic head model obtained after 50000 iterations based on 3-D $\tilde{B}_1^+$ data, in Figure 3.9. This number of iterations was chosen due to time constraints, since it takes approximately 110 hours on an Intel i7–6700 CPU operating on Windows 7 with Matlab 2016a.

3.4. Discussion

We have investigated the performance of two- and three-dimensional CSI-EPT in reconstructing dielectric tissue profiles based on $\tilde{B}_1^+$ data collected inside the reconstruction slice or domain of interest. Since this data has its support inside the reconstruction domain, EPT belongs to the class of so-called hybrid inverse problems [8]. In CSI-EPT, reconstructing the tissue parameters is posed as an optimization problem in which an internal objective function, that is an objective function that measures both field and model discrepancies within the domain of interest, is minimized in an iterative manner. Field discrepancies are measured by considering the L_2-norm of the difference between modeled and measured data, while model discrepancies are measured by an L_2-norm that tells us how well a conductivity and permittivity tissue profile and corresponding contrast source satisfy Maxwell's equations. Including model discrepancies in the objective function is crucial to the performance of CSI-EPT, since it has been shown that without this term unsatisfactory reconstruction results may be obtained [25]. In addition to the tissue profiles, CSI-EPT reconstructs the electric field strength as well, and may therefore also be used to predict the SAR that is induced inside the body or a body part of interest [31], which is important for MR safety and hyperthermia treatment planning, for example. Finally, we have also shown that in two dimensions an alternative non-iterative and integral-based reconstruction algorithm called foIC-EPT may be employed. This method is significantly faster than 2-D

and 3-D CSI-EPT and reconstructs the tissue profiles and the corresponding electric field strength essentially in real-time on a present day standard laptop or PC (Intel i5-i7 or similar). However, foIC-EPT is restricted to two-dimensional configurations, since it exploits two-dimensional E-polarized field structures. CSI-EPT, on the other hand, does not exploit any particular field structure and can be extended to the vectorial three-dimensional case turning CSI-EPT into a volumetric EPT reconstruction method.

We have carried out several comparisons between reconstructions obtained with 2-D CSI-EPT, foIC-EPT, and 3-D CSI-EPT. Our simulations show that care needs to be exercised when a 2-D reconstruction approach is followed, otherwise reconstruction artifacts are obtained in the reconstructed dielectric tissue profiles. Specifically, we have shown that using 2-D methods erroneous reconstructions may be obtained, since the longitudinal variations of the transverse vector potential are completely ignored in the data model for the $\tilde{B}_1^+$ field. Moreover, the vector potential itself is computed differently in 2-D and 3-D, since longitudinal invariance is assumed in the 2-D case. In fact, the transverse electric field and the longitudinal magnetic field vanish in 2-D as a consequence of the (assumed) invariance of the object and external sources along the longitudinal direction. In 3-D, however, all components of the electromagnetic field are present and their contributions to the measured data and object equations have to be taken into account. Of course, in some situations an E-polarized field structure may be present in the midplane of a birdcage coil, but the scattered $\tilde{B}_1^+$-field is also influenced by longitudinal variations of the transverse vector potential ($\partial_z \tilde{A}_z$). These equations can only be simplified to 2-D if we can guarantee that longitudinal invariance or smoothness of certain field components can be imposed before any reconstruction algorithm is applied to the measured data. Therefore, cylindrical body parts such as the legs or arms might be reliably reconstructed via 2-D CSI-EPT, but this at least requires further validation through simulations and measurements using cylindrical phantom models with known dielectric characteristics.

No assumptions on the fields are imposed in 3-D CSI-EPT and reconstruction errors due to such assumptions are therefore avoided. Moreover, 3-D CSI-EPT is a volumetric reconstruction method and is not restricted to a specific plane within the configuration. Reliable reconstructions can be obtained within any desired domain of interest provided that $\tilde{B}_1^+$ data is available within this domain. Unfortunately, computation times significantly increase when applying 3-D CSI-EPT. Depending on the number of unknowns in the EPT reconstruction problem, 3-D CSI-EPT may take many iterations to converge to the desired error tolerance, with total computation times of hours or days even on dedicated computers or servers. In future research, we focus on accelerating the convergence rate of 3-D CSI-EPT by including preconditioning techniques in CSI-EPT (as described in [24], for example) that exploit all *a priori* knowledge we have about the object or body part that needs to be reconstructed. This knowledge can also be used to construct an accurate initial guess thereby possibly further accelerating CSI-EPT.

In our experiments, we have used simulated $\tilde{B}_1^+$-field data to test the performance of 2-D and 3-D CSI-EPT on strongly inhomogeneous structures and to study the differences between two- and three-dimensional CSI-EPT approaches. In real-world

measurements, the data obviously differs from simulated data and CSI-EPT should be adapted so that it can handle measured $\tilde{B}_1^+$ data. In this respect, we have identified three practical issues that need to be addressed, which are part of our current CSI-EPT research.

First, in practice the $\tilde{B}_1^+$-field is obtained in polar form through separate amplitude and phase measurements. In both cases, the collected data is contaminated with noise and therefore filtering or regularization techniques that suppress the effects noise should be incorporated in CSI-EPT. Initial studies show that filtering of the data allows us to handle measured data in foIC-EPT [21] and, as demonstrated in [14], total variation (TV) regularization may suppress noise effects in CSI-EPT. However, due to the many possible choices for the regularization parameter in this method, it is presently not clear for which parameter or parameter range the TV-CSI-EPT scheme is most effective.

Second, the phase that is measured in practice is not the phase of the $\tilde{B}_1^+$-field, but the so-called transceive phase from which the $\tilde{B}_1^+$-phase can be extracted. To this end, the transceive phase approximation is often applied, but the validity of this approximation is not fully understood and may lead to reconstruction errors in the conductivity and permittivity profiles [29]. Fortunately, it is shown in [32] that improved $\tilde{B}_1^+$-phase approximations can be obtained from the transceive phase by incorporating an iterative phase correction scheme in the CSI-EPT reconstruction algorithm. This correction scheme seems to reliably retrieve $\tilde{B}_1^+$-phase maps from the measured transceive phase and leads to improved conductivity and permittivity reconstructions compared with reconstructions that are obtained when the transceive phase approximation is applied. We will include this phase correction mechanism in future CSI-EPT implementations as well. Another option is to opt for phaseless approaches as, for example, proposed in [33, 34].

Finally, in practice the current densities in the transmit coil that generate the incident field depend on the object present, and we must account for this loading effect as well. Specifically, the integral representations for the fields in CSI-EPT are obtained using a scattered field formalism, in which it is assumed that the current density in the transmitting antenna is impressed and independent of the scatterer that may be present in the configuration. In practice, however, these currents do depend on the object and consequently care must be taken when we compute the background field in CSI-EPT. One approach is therefore to simulate this loading effect using a suitable coil and appropriate simulated body model in a commercial field solver and to extract the current densities in the coil from this solver. The background field in CSI-EPT (the field without any load) can then computed using these extracted currents. In this way, the loading effect encountered in practice can be incorporated in our CSI-EPT reconstruction algorithm.

Our final aim is, of course, to turn CSI-EPT into a practical reconstruction method to obtain accurate and reliable conductivity and permittivity tissue maps of an interior part of the human body at MR frequencies of operation. Reconstruction results based on simulated data are very promising, and we think that by addressing the practical issues discussed above, we will indeed make significant progress towards a reliable EPT reconstruction method that provides us with accurate dielectric tissue maps.

References

[1] Valentina Hartwig. Engineering for safety assurance in MRI: analytical, numerical and experimental dosimetry. *Magnetic resonance imaging*, 33(5):681–689, 2015.

[2] JJW Lagendijk. Hyperthermia treatment planning. *Physics in Medicine & Biology*, 45(5):R61, 2000.

[3] Ulrich Katscher and Cornelius AT van den Berg. Electric properties tomography: biochemical, physical and technical background, evaluation and clinical applications. *NMR in Biomedicine*, 30(8):e3729, 2017.

[4] Sami Gabriel, RW Lau, and Camelia Gabriel. The dielectric properties of biological tissues: Ii. measurements in the frequency range 10 Hz to 20 GHz. *Physics in medicine & biology*, 41(11):2251, 1996.

[5] Brian H Brown. Electrical impedance tomography (EIT): a review. *Journal of medical engineering & technology*, 27(3):97–108, 2003.

[6] Rohit Chandra, Huiyuan Zhou, Ilangko Balasingham, and Ram M Narayanan. On the opportunities and challenges in microwave medical sensing and imaging. *IEEE transactions on biomedical engineering*, 62(7):1667–1682, 2015.

[7] Xiaotong Zhang, Jiaen Liu, and Bin He. Magnetic-resonance-based electrical properties tomography: a review. *IEEE reviews in biomedical engineering*, 7:87–96, 2014.

[8] Guillaume Bal. Hybrid inverse problems and internal functionals. *Inverse problems and applications: inside out. II*, 60:325–368, 2013.

[9] EM Haacke, LS Petropoulos, EW Nilges, and DH Wu. Extraction of conductivity and permittivity using magnetic resonance imaging. *Physics in Medicine & Biology*, 36(6):723, 1991.

[10] Ulrich Katscher, Tobias Voigt, Christian Findeklee, Peter Vernickel, Kay Nehrke, and Olaf DÖssel. Determination of electric conductivity and local SAR via B_1 mapping. *IEEE transactions on medical imaging*, 28(9):1365–1374, 2009.

[11] Tobias Voigt, Ulrich Katscher, and Olaf Doessel. Quantitative conductivity and permittivity imaging of the human brain using electric properties tomography. *Magnetic Resonance in Medicine*, 66(2):456–466, 2011.

[12] Astrid LHMW Van Lier, David O Brunner, Klaas P Pruessmann, Dennis WJ Klomp, Peter R Luijten, Jan JW Lagendijk, and Cornelis AT van den Berg. B_1^+ phase mapping at 7 T and its application for in vivo electrical conductivity mapping. *Magnetic Resonance in Medicine*, 67(2):552–561, 2012.

[13] Fatih S Hafalir, Omer F Oran, Necip Gurler, and Yusuf Z Ider. Convection-reaction equation based magnetic resonance electrical properties tomography (cr-MREPT). *IEEE transactions on medical imaging*, 33(3):777–793, 2014.

[14] Edmond Balidemaj, Cornelis AT van den Berg, Johan Trinks, Astrid LHMW van Lier, Aart J Nederveen, Lukas JA Stalpers, Hans Crezee, and Rob F Remis. CSI-EPT: A contrast source inversion approach for improved MRI-based electric properties tomography. *IEEE transactions on medical imaging*, 34(9):1788–1796, 2015.

[15] Ilias Giannakopoulos, Jos EC Serrallés, Luca Daniel, Daniel Sodickson, Athanasios Polimeridis, Jacob K White, and Riccardo Lattanzi. Magnetic-resonance-based electrical property mapping using global Maxwell tomography with an 8-channel head coil at 7 Tesla: a simulation study. *IEEE Transactions on Biomedical Engineering*, 2020.

[16] José EC Serrallés, Ilias I Giannakopoulos, Bei Zhang, Carlotta Ianniello, Martijn A Cloos, Athanasios G Polimeridis, Jacob K White, Daniel K Sodickson, Luca Daniel, and Riccardo Lattanzi. Noninvasive estimation of electrical properties from magnetic resonance measurements via global Maxwell tomography and match regularization. *IEEE Transactions on Biomedical Engineering*, 67(1):3–15, 2019.

[17] Ronghan Hong, Shengnan Li, Jianhua Zhang, Youyu Zhang, Na Liu, Zhiru Yu, and Qing Huo Liu. 3-D MRI-based electrical properties tomography using the volume integral equation method. *IEEE Transactions on Microwave Theory and Techniques*, 65(12):4802–4811, 2017.

[18] Alessandro Arduino, Luca Zilberti, Mario Chiampi, and Oriano Bottauscio. CSI-EPT in presence of RF-shield for MR-coils. *IEEE Transactions on medical imaging*, 36(7):1396–1404, 2017.

[19] Anar Rahimov, Amélie Litman, and Guillaume Ferrand. MRI-based electric properties tomography with a quasi-Newton approach. *Inverse Problems*, 33(10):105004, 2017.

[20] Necip Gurler and Yusuf Ziya Ider. Gradient-based electrical conductivity imaging using MR phase. *Magnetic resonance in medicine*, 77(1):137–150, 2017.

[21] Patrick Fuchs, Stefano Mandija, Peter Stijnman, Wyger Brink, Nico van den Berg, and Rob Remis. First-order induced current density imaging and electrical properties tomography in MRI. *IEEE Transactions on Computational Imaging*, 4:624–631, 2018.

[22] Peter M Van den Berg and A Abubakar. Contrast source inversion method: State of art. *Progress in Electromagnetics Research*, 34:189–218, 2001.

[23] Peter M Van Den Berg and Ralph E Kleinman. A contrast source inversion method. *Inverse problems*, 13(6):1607, 1997.

[24] Peter M van den Berg, AL Van Broekhoven, and Aria Abubakar. Extended contrast source inversion. *Inverse problems*, 15(5):1325, 1999.

[25] Peter M Van den Berg and Kasper FI Haak. Profile inversion by error reduction in the source type integral equations. *Wavefields and Reciprocity – Proceedings of a Symposium Held in Honour of Professor dr. A.T. de Hoop*, pages 87–98, 1996.

[26] Bob van den Bergen, Christiaan C Stolk, Jan Bouwe van den Berg, Jan JW Lagendijk, and Cornelis AT Van den Berg. Ultra fast electromagnetic field computations for RF multi-transmit techniques in high field MRI. *Physics in Medicine & Biology*, 54(5):1253, 2009.

[27] Reijer L Leijsen, Wyger M Brink, Cornelis AT Van Den Berg, Andrew G Webb, and Rob F Remis. 3-D contrast source inversion-electrical properties tomography. *IEEE transactions on medical imaging*, 37(9):2080–2089, 2018.

[28] Andreas Christ, Wolfgang Kainz, Eckhart G Hahn, Katharina Honegger, Marcel Zefferer, Esra Neufeld, Wolfgang Rascher, Rolf Janka, Werner Bautz, Ji Chen, et al. The virtual family—development of surface-based anatomical models of two adults and two children for dosimetric simulations. *Physics in Medicine & Biology*, 55(2):N23, 2009.

[29] Astrid LHMW van Lier, Alexander Raaijmakers, Tobias Voigt, Jan JW Lagendijk, Peter R Luijten, Ulrich Katscher, and Cornelis AT van den Berg. Electrical properties tomography in the human brain at 1.5, 3, and 7T: a comparison study. *Magnetic resonance in medicine*, 71(1):354–363, 2014.

[30] Yousef Saad. *Iterative methods for sparse linear systems*, volume 82. SIAM, 2003.

[31] Edmond Balidemaj, Cornelis AT van den Berg, Astrid LHMW van Lier, Aart J Nederveen, Lukas JA Stalpers, Hans Crezee, and Rob F Remis. B1-based SAR reconstruction using contrast source inversion–electric properties tomography (CSI-EPT). *Medical & biological engineering & computing*, 55(2):225–233, 2017.

[32] Peter Stijnman, Stefano Mandija, Patrick Fuchs, Rob Remis, and Nico van den Berg. Transceive phase correced contrast source inversion-electrical properties tomography. In *International Society for Magnetic Resonance in Medicine 26th Annual Meeting and Exhibition (ISMRM18)*, page 5087, Paris (France), June 2018.

[33] Alessandro Arduino, Oriano Bottauscio, Mario Chiampi, and Luca Zilberti. Magnetic resonance-based imaging of human electric properties with phaseless contrast source inversion. *Inverse Problems*, 34(8):084002, jun 2018.

[34] Martina T Bevacqua, Gennaro G Bellizzi, Lorenzo Crocco, and Tommaso Isernia. A method for quantitative imaging of electrical properties of human tissues from only amplitude electromagnetic data. *Inverse Problems*, 35(2):025006, jan 2019.

4

Gradient Coil Design and Realization for a Halbach-Based MRI System

Bart de Vos
Patrick Fuchs
Thomas O'Reilly
Andrew Webb
Rob Remis

ABSTRACT– *In this paper we design and construct gradient coils for a Halbach permanent magnet array magnetic resonance (MR) scanner. The target field method, which is widely applied for the case of axial static magnetic fields, has been developed for a transverse static magnetic field as produced by a Halbach permanent magnet array. Using this method, current densities for three gradient directions are obtained and subsequently verified using a commercial magneto-static solver. Stream functions are used to turn the surface current densities into wire patterns for constructing the gradient coils. The measured fields are in good agreement with simulations and their prescribed target fields. Three dimensional images have been acquired using the constructed gradient coils with very low degree of geometric distortion.*

Appeared in:
IEEE Transactions on Magnetics, ***56***, *3, March 2020*
doi: 10.1109/TMAG.2019.2958561

4.1. Introduction

Gradient coils are an integral part of magnetic resonance imaging (MRI) systems. Ideally, such coils produce linear magnetic fields that are used to spatially encode an object or body part: linearity allows simple image reconstruction via an inverse 2- or 3-dimensional Fourier transformation [1]. Numerous methods for the design and optimisation of gradient coils have been proposed over the years (e.g. [2, 3]), but most of these approaches are for conventional MRI scanners with the static magnetic field (B_0) aligned axially along the bore of the system.

Interest in MRI for a low-resource setting is increasing [4]. Conventional MRI hardware cannot be used under such circumstances, since it is expensive and generally difficult to maintain. Superconducting magnets, for example, are financially out of reach, and high power and fast switching requirements for gradient and radiofrequency hardware simply cannot be met. Moreover, conventional scanners are typically immobile and therefore cannot be easily transported to different locations.

To address the difficulties that are encountered in a low-resource setting, new MR systems are being proposed such as MR scanners based on resistive magnets [5, 6] or systems that utilize a Halbach permanent magnet array [7, 8]. For a resistive magnet, gradient coil design runs along similar lines as for conventional MRI systems, albeit typically for smaller bore sizes and lower power requirements. In contrast, for a Halbach array the background magnetic field is transverse to the bore as opposed to along the bore, and this provides additional challenges for the design of the gradient coils [9]. In a previous publication we described a 27 cm clear bore Halbach array designed ultimately for pediatric neuroimaging, operating at 2.15 MHz [7]. For this system simple non-optimized gradient coils were constructed, but the linear range was quite limited.

In this paper, the target field method, as originally proposed by Turner [10], is applied to design transverse oriented gradient fields. Specifically, a transverse gradient field is prescribed on an inner cylinder that is concentric to the Halbach array and the target field method is applied to find surface current densities on an outer cylinder that generate magnetic fields, which approximate this prescribed target field. Since this is an inverse source problem, regularization is required to obtain physically acceptable surface current densities. To this end, we follow the standard target field method and include regularization through apodisation using a parametric spectral-domain Gaussian filter. By following this approach, x-, y-, and z- gradient coils are designed and realized. Furthermore, field simulations and measurements of these are presented, to show that the produced gradients are in good agreement with simulation, thereby verifying that the modified target field method can indeed be used to realize gradient coils in case the background field is transverse to the axis of the bore of a Halbach MR scanner. Finally, the gradient coils are incorporated in an experimental low-field Halbach MR scanner [7] thereby enabling us to use Fourier imaging techniques to acquire three-dimensional low-field MR images. Initial imaging results that are obtained with this scanner are presented as well.

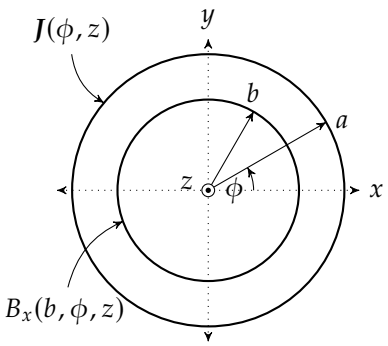

Figure 4.1: Geometry and coordinate system for the target field method. The outer cylinder with radius a supports a surface current $\boldsymbol{J}$ and the x-component of the magnetic field is prescribed on the inner cylinder with radius $b < a$. Both cylinders are of infinite length in the z-direction.

4.2. Target Field Method

To design gradient coils for a Halbach scanner with a transverse B_0 field, consider the cylindrical configuration illustrated in Figure 4.1 consisting of two cylinders that extend to infinity in the positive and negative z-direction. The outer cylinder has a radius a and the domains inside ($r < a$) and outside ($r > a$) the cylinder are filled with air. This cylinder supports a surface current density denoted by $\boldsymbol{J}$ and our objective is to find a surface current that approximates a prescribed magnetic field $\boldsymbol{B}$ on the inner cylinder with radius b. Given the cylindrical structure of our configuration, we will mainly work in cylindrical coordinates.

As a first step, we specify the target fields. Specifically, for a background field aligned in the x-direction, one of the following three linear x-directed gradient fields must be designed

$$B_x(b, \phi, z) = \begin{cases} \Gamma_{\text{tr}}(z) b \cos(\phi) g_x \\ \Gamma_{\text{tr}}(z) b \sin(\phi) g_y \\ \Gamma_{\text{ln}}(z) g_z. \end{cases} \tag{4.1}$$

These are prescribed on an inner cylinder with fixed radius $b < a$ to derive surface currents (and ultimately the position of surface copper wires) that generate fields which approximate these given target fields. In the above expressions, $g_{x,y,z} > 0$ are constants and $\Gamma_{\text{tr}}(z)$ and $\Gamma_{\text{ln}}(z)$ are the transverse (tr) and longitudinal (ln) gradient shape functions given by

$$\Gamma_{\text{tr}}(z) = \frac{1}{1 + \left(\frac{z}{d}\right)^n} \quad \text{and} \quad \Gamma_{\text{ln}}(z) = \frac{z}{1 + \left(\frac{z}{d}\right)^n}, \tag{4.2}$$

respectively, where d and n (n being an even integer) are tuning parameters that determine the length and decay rate of the gradient field in the z-direction. Note that $\Gamma_{\text{tr}}(z)$ is an even function of z, while $\Gamma_{\text{ln}}(z)$ is an odd function of z. Figure 4.2 illustrates the two gradient shape functions as a function of z/d for various choices of the order n. These functions are chosen since they are also used in the original target field

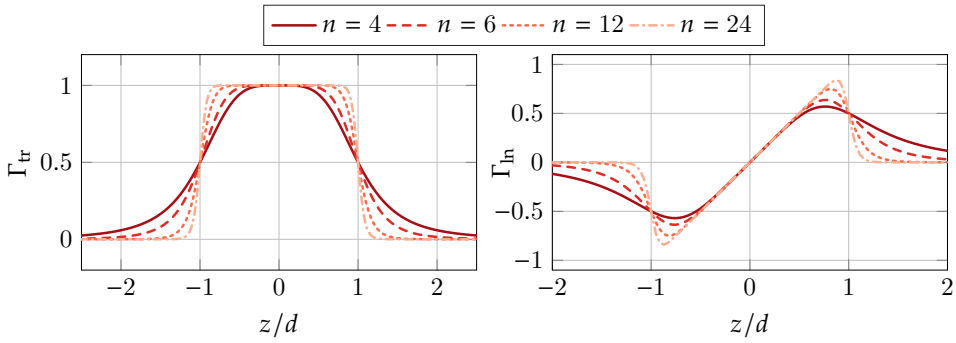

Figure 4.2: The gradient shape functions Γ_{tr} (left) and Γ_{ln} (right) as a function of z/d for different values of the order n of the gradient profile functions.

method, and have closed form expressions for their transforms, other shapes are of course also possible.

To find a surface current density that approximately produces the prescribed target fields, we apply a two-dimensional Fourier transformation with respect to the spatial coordinate z and the angle ϕ. For a generic field quantity $\Psi(r,\phi,z)$ this Fourier transformation is given by

$$\tilde{\Psi}^{[m]}(r,k) = \int_{z=-\infty}^{\infty} \int_{\phi=-\pi}^{\pi} \Psi(r,\phi,z) e^{-\mathrm{j}m\phi} e^{-\mathrm{j}kz} \,\mathrm{d}\phi \,\mathrm{d}z \tag{4.3}$$

and the corresponding inverse Fourier transformation is

$$\Psi(r,\phi,z) = \frac{1}{4\pi^2} \int_{k=-\infty}^{\infty} \sum_{m=-\infty}^{\infty} \tilde{\Psi}^{[m]}(r,k) e^{\mathrm{j}m\phi} e^{\mathrm{j}kz} \,\mathrm{d}k. \tag{4.4}$$

In Appendix A.1 it is shown that the Fourier transform of the target field $B_x(b,\phi,z)$ is related to the Fourier transform of the ϕ-component of the surface current by

$$\begin{aligned} \tilde{B}_x^{[m]}(b,k) = {} & \frac{\mathrm{j}}{2} \left[\tilde{P}^{[m-1]}(b,k) - \tilde{Q}^{[m-1]}(b,k)\right] \tilde{J}_\phi^{[m-1]}(k) \\ & + \frac{\mathrm{j}}{2} \left[\tilde{P}^{[m+1]}(b,k) + \tilde{Q}^{[m+1]}(b,k)\right] \tilde{J}_\phi^{[m+1]}(k), \end{aligned} \tag{4.5}$$

where $\tilde{P}^{[m]}(b,k)$ and $\tilde{Q}^{[m]}(b,k)$ are given by

$$\tilde{P}^{[m]}(b,k) = a\mu_0 k I_m'(|k|\,b) K_m'(|k|\,a), \tag{4.6}$$

and

$$\tilde{Q}^{[m]}(b,k) = m \frac{a\mu_0}{b} \frac{|k|}{k} I_m(|k|\,b) K_m'(|k|\,a), \tag{4.7}$$

with μ_0 the permeability of vacuum, and I_m and K_m modified Bessel functions of the first and second kind, respectively, and the prime indicates differentiation with respect to the argument of the Bessel functions. Note that $\tilde{P}^{[-m]}(b,k) = \tilde{P}^{[m]}(b,k)$ and $\tilde{Q}^{[-m]}(b,k) = -\tilde{Q}^{[m]}(b,k)$ for $m \in \mathbb{Z}$.

Since the target fields are known, Equation (4.5) can be formally solved for the ϕ-component of a spectral surface current density. However, similar to the standard target field method, such a current becomes unbounded as $|k| \to \infty$, which is not surprising, since we are attempting to directly solve an (ill-posed) inverse source problem. Therefore, regularization is applied in the form of a so-called apodisation function $\tilde{T}(k)$, which serves as a low-pass filter that prevents exponential growth of the spectral domain current densities. Usually, the Gaussian function $\tilde{T}(k) = e^{-2(kh)^2}$ is used for apodisation (with h a regularization parameter) and we use this Gaussian in our approach as well.

Having found a solution to Equation (4.5) and filtering out high spatial frequencies through multiplication by $\tilde{T}(k)$, the ϕ-component of the surface current is obtained by substituting the filtered spectral solution into the inverse Fourier transformation. Denoting the resulting spatial currents by J_ϕ^x, J_ϕ^y, and J_ϕ^z for the ϕ-component of the surface current in the case of an x-, y-, or z-gradient target field, we obtain the surface current densities

$$J_\phi^x(\phi,z) = -\mathrm{j}b\frac{g_x}{\pi}\cos(2\phi)\int_{k=-\infty}^{\infty}\frac{\tilde{\Gamma}_{\mathrm{tr}}(k)\tilde{T}(k)}{\tilde{P}^{[2]}+\tilde{Q}^{[2]}}e^{\mathrm{j}kz}\mathrm{d}k, \tag{4.8}$$

$$J_\phi^y(\phi,z) = -\mathrm{j}b\frac{g_y}{\pi}\sin(2\phi)\int_{k=-\infty}^{\infty}\frac{\tilde{\Gamma}_{\mathrm{tr}}(k)\tilde{T}(k)}{\tilde{P}^{[2]}+\tilde{Q}^{[2]}}e^{\mathrm{j}kz}\mathrm{d}k, \tag{4.9}$$

and

$$J_\phi^z(\phi,z) = -\mathrm{j}\frac{g_z}{\pi}\cos(\phi)\int_{k=-\infty}^{\infty}\frac{\tilde{\Gamma}_{\mathrm{ln}}(k)\tilde{T}(k)}{\tilde{P}^{[1]}+\tilde{Q}^{[1]}}e^{\mathrm{j}kz}\mathrm{d}k. \tag{4.10}$$

The corresponding z-components of the surface current density follow directly from the continuity equation. Further details can be found in Appendix A.1.1.

Finally, from the computed current densities it is straightforward to extract the wire or current paths using stream functions as described in e.g. [10]. These stream functions can then be used to realize the gradient coils.

To verify our design method, we first compute the surface current densities given by Equations (4.8) to (4.10) and use stream functions to convert these current densities into wire patterns. These patterns are then used in a magneto-static field solver to verify that currents flowing through the conductors of the gradient coils indeed produce the prescribed target fields. Subsequently, the three gradient coils are constructed and a magnetic field map of the z-gradient coil measured. Finally, the three gradient coils are incorporated into the low-field MRI Halbach-based scanner de-

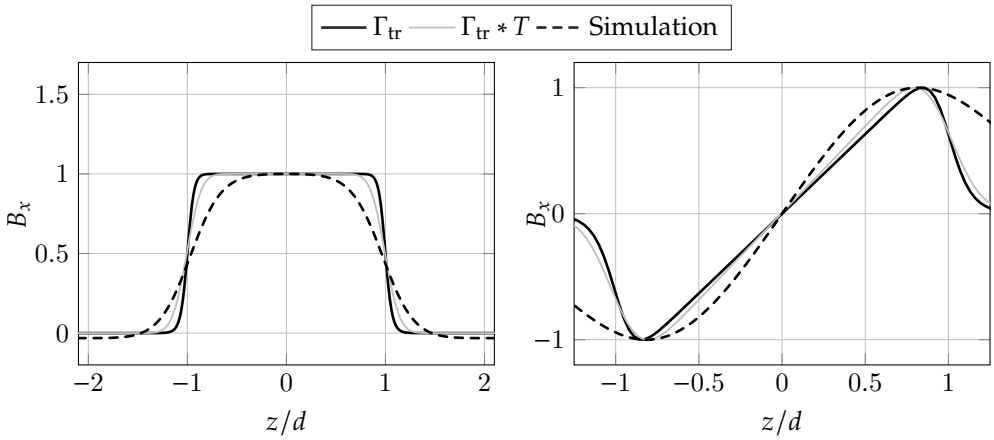

Figure 4.3: The x- (left) and z- (right) gradient shape functions along the bore of the coil (at radius b and $\phi = 0$) compared with the target field shapes used to generate the gradient coil.

scribed previously. Three-dimensional imaging results which are obtained with this scanner are also presented.

4.3. Results

4.3.1. Simulation results

The surface current densities of Equations (4.8) to (4.10) were computed using MATLAB[1]. The regularization parameter was chosen as $h = 0.05$ which provides the least amount of regularisation that still leads to smooth current paths, and the order n of the target fields was taken as $n = 16$ for the z-gradient coil and $n = 30$ for the x- and y-gradient coils. These values were chosen in order for the physical length of the coils to correspond to the system requirements (the length of the magnet is 50 cm, and the gradients are constrained to a length of 37 cm inside the magnet). The design of the y-gradient coil is equivalent to the design of the x-gradient coil, since $J^y_\phi(\phi, z) = g_y\, g_x^{-1} J^x_\phi(\phi - \pi/4, z)$, that is, $J^y_\phi(\phi, z)$ is a scaled and rotated version of J^x_ϕ.

Subsequently, the computed surface current densities were turned into discrete current paths using stream functions [10]. These current paths then served as input for a magneto-static field simulation using CST[2]. The simulations provided a magnetic field, which could then be compared with the prescribed target field (4.1).

This comparison can be found Figure 4.3, where the prescribed target field profile functions are shown along with the simulated and normalized field along the bore of the coil at $\phi = 0$ and $r = b$, since the target field is prescribed at this radius. As can be seen from the figures, the simulated fields closely follow the prescribed target profile functions. The difference is primarily caused by the apodisation function. This function effectively smoothens the fields along the z-direction.

[1] MATLAB 2018b, The MathWorks, Inc., Massachussets, USA.
[2] Computer Simulation Technology, 2019, 3DS SIMULIA, Johnston, RI, USA.

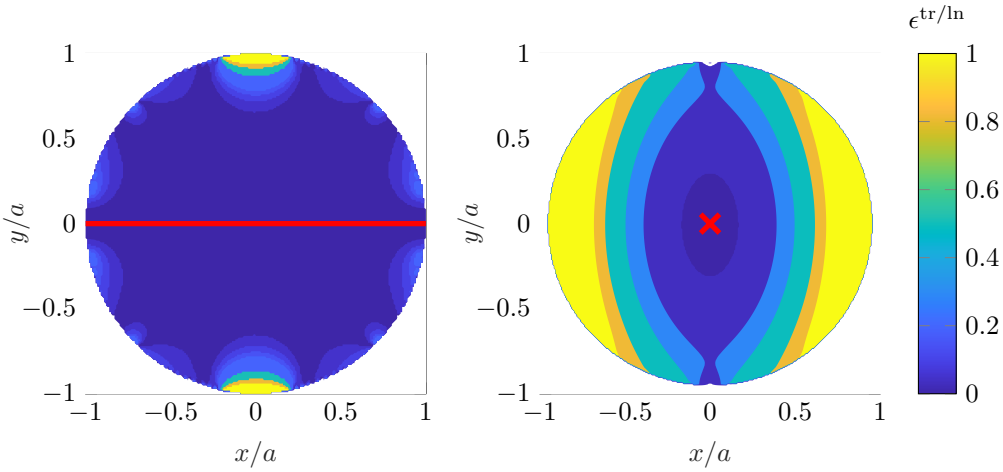

Figure 4.4: Linear uniformity error $\epsilon^{\{\mathrm{tr,ln}\}}$ with respect to the field at the center of the bore. The error ϵ^{tr} for the x-gradient coil is shown at the top, while the error ϵ^{ln} for the z-gradient coil is shown at the bottom. The red line and cross indicate the reference field line.

To study the effects of the coil parameters on the performance of the gradient coils, let us first consider the coil efficiency η, which is defined as the gradient strength produced by a unit current ($\mathrm{T\,m^{-1}\,A^{-1}}$). We found that the order n of the target field profile function essentially does not influence the coil efficiencies of the x- and y-gradient coils. As n increases, the distance between adjacent turns decreases, which will increase the inductance and shorten the physical coil length in the z-direction. The coil efficiency, however, remains essentially the same. On the other hand, n does influence the efficiency of the z-gradient. For example, if we increase the order of the profile function from $n = 6$ to $n = 26$, the efficiency drops by approximately 20%. Larger orders may be necessary for z-gradient coils, however, since otherwise the coil length in the z-direction may become longer than the length of the Halbach array. We note that special care must be taken when increasing n in gradient coil design, since numerically the wires can be placed arbitrarily close together but in reality this is limited by the construction method. Close inspection of the current paths with the construction method in mind is needed to find the respective limits for this parameter.

The linear uniformity of the gradient influences the region which can be imaged without distortions. This is quantified using the difference between the linear varying (prescribed) field and the field actually generated. In this case the simulated fields along the center line of the corresponding gradient are used as opposed to the prescribed fields. For the x-gradient this center line is across the bore in the x-direction (red line in Figure 4.4, top), for the z-gradient it is along the axis of the bore (cross in Figure 4.4, bottom). For the simulated field values B_x this error is computed as

$$\epsilon^{\{\mathrm{tr,ln}\}}(x,y) = \frac{|B_x(x,y) - B_x^{\{\mathrm{tr,ln}\}}|}{|B_x^{\{\mathrm{tr,ln}\}}|} \tag{4.11}$$

where the references $B_x^{\{\mathrm{tr,ln}\}}$ are defined as $B_x^{\mathrm{tr}} = B_x(x,0,0)$, and $B_x^{\mathrm{ln}} = B_x(0,0,z)$. These errors are displayed in Figure 4.4 from which it is immediately clear that the x-gradient field is linear over a much larger area in the xy-plane than the z-gradient field.

The uniformity of the gradient fields can also be described in terms of the linear spherical volume. Within this volume the deviation of the simulated field from a target field is less than 5%. For the transverse x- and y gradients the linear spherical volume is approximately 70% of the diameter of the outer cylinder. In other words, a sphere centered at the origin and having a radius of $0.7a$ completely encloses a region where the realized field deviates less than 5% from the prescribed field. For the longitudinal z-gradient field, however, the linear volume is only 20% of the diameter of the outer cylinder. Clearly, the linear region of the z-gradient coil is smaller than the linear region of the x- and y-gradient coils, which is due to the geometry of the z-gradient coil. In commercial scanners similar non-uniformity issues arise for these type of gradient fields and their effects in three-dimensional imaging are usually corrected in post-processing.

To summarize, we have found that the coil efficiency η of the x- and y-gradient coils does not significantly vary for moderate changes in the order n of the target field function. The coil efficiency of the z-gradient coil, however, is strongly dependent on n. Larger values of this parameter lead to z-gradient coils with a smaller spatial extent in the longitudinal z-direction, but decrease the coil efficiency. Moreover, for all coils the winding separation decreases as n increases, which puts a restriction on the magnitude of the order n of the profile function, since in practice wires cannot be placed arbitrarily close to each other.

4.3.2. Gradient Construction

To fixate and accurately position the wires, a 3D printable mould was created where the current paths were designed as slots. These slots facilitate easy and accurate placement of the wires. A single layer of 1.5 mm diameter copper wire was used to minimize the resistance and to reduce power dissipation. For the z-gradient coil, the order of the target field profile function $n = 16$ is chosen, which leads to a gradient coil with a longitudinal length that is acceptable. For x- and y-gradient coils an order of $n = 30$ was chosen. This was the maximum n for which the adjacent wires (diameter 1.5 mm) do not overlap. It must be noted that all three gradients have a slightly different radius as they are placed on top of each other. Denoting the radii of the x-, y-, and z-gradient coils by a_x, a_y, and a_z, respectively, the coils were placed on top of each other such that $a_z < a_y < a_x$. In other words, the y-gradient coil is positioned on top of the z-gradient coil, and the x-gradient coil on top of the y-gradient coil. This order of stacking was chosen because the z-gradient has the lowest efficiency and the x-gradient naturally has the highest performance due to the background field being x-directed.

The resistance and inductance of the coils were measured using an RCL meter (Keysight U1733C) and a table of the coil design parameters and electrical properties can be found in Table 4.1. Renderings of the wire paths of the coils are shown in Figure 4.5, where currents run in a clockwise manner through the red wires and in a

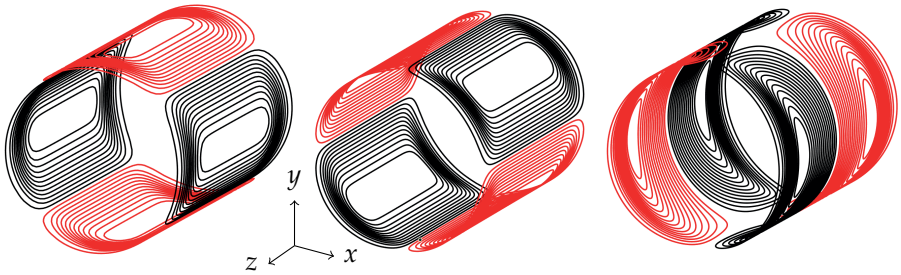

Figure 4.5: Three-dimensional rendering of the wire paths of the x- (left), y- (middle), and z- (right) gradients. The color indicates the direction of the current: red for clockwise and black for counterclockwise currents.

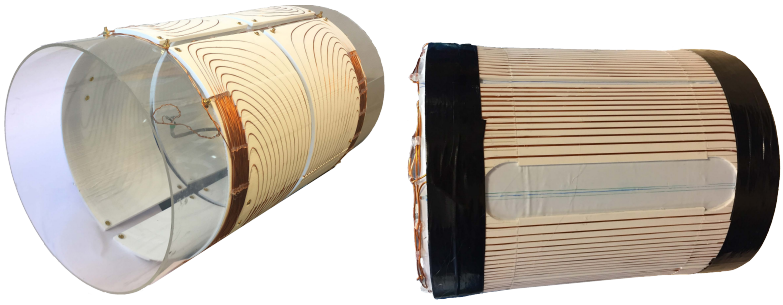

Figure 4.6: A prototype z-gradient coil (left), where the 3D printed mould is clearly visible, and the gradient coil assembly after attaching the y-gradient (right).

counterclockwise manner through the black wires. Lastly, photographs of the finished assembly and the 3D moulds can be found in Figure 4.6.

4.3.3. Measurement results

The field generated by the gradient coils is measured using a multipurpose 3-axis measuring robot [11]. The robot holds an AlphaLab inc. Gauss meter model GM2 which measures the field at a resolution of 10 mm isotropic. In Figure 4.7, the x-component of the measured gradient field is shown as measured along the linear axis of the gradient at the center of the coil ($B_x(x,0,0)$ for the x-gradient, $B_x(0,y,0)$ for the y-gradient and $B_x(0,0,z)$ for the z-gradient). The measured and simulated fields are in good agreement with each other. Finally, for completeness we mention that the resistance and inductance of the coils were also measured using a Keysight U1733C RCL meter. These can be found in Table 4.1 together with the efficiency of the coils computed from the field measurements.

The constructed coils were incorporated in an experimental low-field Halbach MR scanner that is currently under development at the Leiden university medical center (LUMC) [7]. The gradient coils were tested and used to acquire three-dimensional images of different types of objects. Figure 4.8 provides an example of such an image, in which coronal, sagittal, and transverse slices through a melon are depicted.

Table 4.1: Design parameters of the gradient coils. The power is computed for a gradient strength of 10 mT m^{-1}.

Type	n	d [mm]	l [m]	# turns / quad	a [mm]	η_{sim} [mT m^{-1} A^{-1}]	η_{meas} [mT m^{-1} A^{-1}]	R [Ω]	L [μH]	P [W]
z	16	140	38	15	135	0.52	0.59	0.37	180	329
x	30	155	42	12	139	0.81	0.95	0.41	227	165
y	30	155	43	12	137	0.82	1.02	0.40	224	162

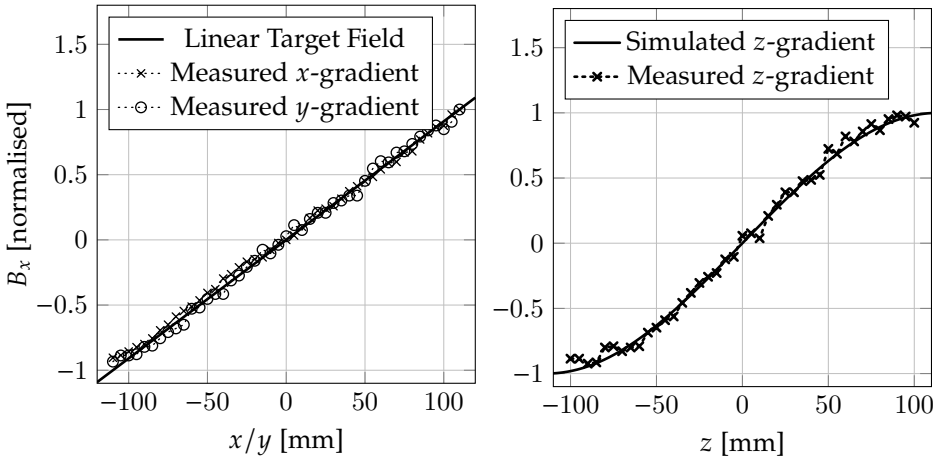

Figure 4.7: The simulated and measured x-component of the gradient field in a longitudinal slice through the center of a x- and y-gradient coil (left) and z-gradient coil (right). The fields have been normalised for ease of comparison, the measured efficiency η can be used to find the relation between current and field strength.

Minimal distortion can be observed, which is most likely due to B_0 inhomogeneities and not due to any nonlinearities in the gradient fields.

4.4. Discussion and Conclusion

We have applied the target field method to design gradient coils for an MR scanner with a transverse magnetic background field. It is then relatively straightforward to turn these current paths into a constructed gradient coil using simple three-dimensional printing techniques and wire winding. Field measurements confirmed that the proposed design procedure indeed leads to gradient coils that produce the required gradient fields.

Transverse x- and y-gradient coils are generally more efficient, and therefore easier to design with respect to field requirements than the longitudinal z-gradient coils. The coil efficiency of the transverse coils is typically less sensitive to the order of the target field profile function and the magnitude of the order is basically limited by the spacing allowed between the wires. The region of uniform linearity is also much larger for transverse gradient coils than for z-gradient coils as indicated by the uniformity error that we introduced and the linear spherical volume. Coil efficiency of a

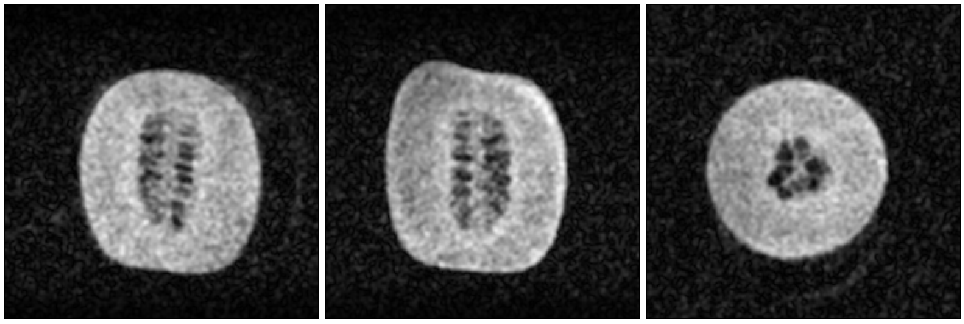

Figure 4.8: Coronal (left), sagital (middle), and transverse (right) images of a melon obtained with the low-field scanner of the LUMC that incorporates the gradient coils described in this paper. A 3D-turbo spin echo (TSE) sequence was used with echo time (TE) over repetition time (TR) of 30 ms/2000 ms. Echo train length was 32, with a field of view (FoV) of $192 \times 192 \times 192$ mm. The data matrix consisted of $128 \times 128 \times 128$ complex points. Total acquisition time was 17 minutes 4 seconds.

z-gradient coil, in contrast, strongly depends on the order of the profile function and decreases as the order increases. This indicates that a relatively small order should be chosen to realize an effective z-gradient coil, but selecting a small order leads to a very long gradient coil which may be longer than the magnet itself. Careful tuning is therefore necessary to obtain a realizable z-gradient coil with a sufficiently large linear region and coil efficiency. Given the cylindrical geometry of our Halbach configuration, it can also be expected that the realization of a z-gradient coil in a scanner with a transverse background field is more difficult than realizing transverse gradient coils, since the magnitude of a linearly varying transverse field along the bore of the magnet naturally increases as we move in a radial direction towards the coil.

Possible extensions of this work include incorporating gradient power minimization as it relates to the Halbach configuration, since this would simplify power supply requirements, which is of importance in a low-resource setting. In addition, using conductive sheets for the construction of a gradient coil may be a feasible large-scale production method.

To summarize, with the proposed design methodology it is possible to design effective x-, y-, and z-gradient coils in case of transverse background fields as encountered in a Halbach permanent magnet scanner. The method is very efficient and allows for parametric coil design, thereby providing insight into the trade offs of gradient coil construction.

Acknowledgment

The authors would like to thank Wouter Teeuwisse for fruitful discussions and his help in the construction and assembly of the gradient coils, Danny de Gans for his work on the gradient amplifier, and Martin van Gijzen for his support in the low field MRI scanner project. This research was made possible in part through the NWO-WOTRO grant nr. W 07.303.101:'A sustainable MRI system to diagnose hydrocephalus in Uganda', Horizon 2020 ERC Advanced NOMA-MRI 670629: and the Simon Stevin

Prijs from the Dutch research council (NWO).

References

[1] M. Bernstein, K. F. King, and X. J. Zhou. *Handbook of MRI Pulse Sequences*. Academic Press, 2004.

[2] Robert Turner. Gradient coil design: A review of methods. *Magnetic Resonance Imaging*, 11(7):903 – 920, 1993.

[3] S.S. Hidalgo-Tobon. Theory of gradient coil design methods for magnetic resonance imaging. *Concepts in Magnetic Resonance Part A*, 36A(4):223–242, 2010.

[4] Mathieu Sarracanie, Cristen D. LaPierre, Najat Salameh, David E. J. Waddington, Thomas Witzel, and Matthew S. Rosen. Low-cost high-performance MRI. *Scientific Reports*, 5(1):15177, 2015.

[5] G. Morrow. Progress in MRI magnets. *IEEE Transactions on Applied Superconductivity*, 10(1):744–751, March 2000.

[6] Rui Zhang, Jing Xu, Youyi Fu, Yangjing Li, Kefu Huang, Jue Zhang, and Jing Fang. An optimized target-field method for MRI transverse biplanar gradient coil design. *Measurement Science and Technology*, 22(12):125505, nov 2011.

[7] T. O'Reilly, W.M. Teeuwisse, and A.G. Webb. Three-dimensional MRI in a homogenous 27cm diameter bore Halbach array magnet. *Journal of Magnetic Resonance*, 307:106578, 2019.

[8] C. Z. Cooley, M. W. Haskell, S. F. Cauley, C. Sappo, C. D. Lapierre, C. G. Ha, J. P. Stockmann, and L. L. Wald. Design of sparse Halbach magnet arrays for portable MRI using a genetic algorithm. *IEEE Transactions on Magnetics*, 54(1):1–12, Jan 2018.

[9] Wentao Liu, Federico Casanova, Bernhard BlAŒmich, and Donglin Zu. An efficacious target-field approach to design shim coils for Halbach magnet of mobile NMR sensors. *Applied Magnetic Resonance*, 42(1):101–112, 2012.

[10] R Turner. A target field approach to optimal coil design. *Journal of Physics D: Applied Physics*, 19(8):L147–L151, aug 1986.

[11] COSI Measure. Multi-purpose 3-axis robot with submillimeter resolution for static / dynamic field mapping. http://www.opensourceimaging.org/project/cosi-measure, 2020. Accessed: 2020-03-11.

5

Generalized Signal Models and Direct FID-Based Dielectric Parameter Retrieval in MRI

Patrick Fuchs
Rob Remis

ABSTRACT– *This paper presents a full-wave signal models for magnetic and electric field measurements in a magnetic resonance imaging (MRI) scanner. Our analysis is based on a scattering formalism in which the presence of an object or body is taken into account via an electric scattering source. We show that these signal models can be evaluated, provided the Green's tensors of the background field are known along with the dielectric parameters of the object and the magnetization within the excited part of the object. Furthermore, explicit signal expressions are derived in case of a small homogeneous ball that is embedded in free space and for which the quasi-static Born approximation can be applied. The conductivity and permittivity of the ball appear as explicit parameters in the resulting signal models and allow us to study the sensitivity of the measured signals with respect to these dielectric parameters. Moreover, for free induced decay (FID) signals we show that under certain conditions it is possible to retrieve the dielectric parameters of the ball from noise-contaminated induction decay signals that are based on electric or magnetic field measurements.*

Submitted to:
IEEE Transactions on Antennas and Propagation

5.1. Introduction

The influence of biological tissue on a typical magnetic resonance imaging (MRI) experiment (and previously in nuclear magnetic resonance (NMR) or zeugmatography [1]) has been investigated almost as long as the imaging modality exists. Most of this research has focused on the signal to noise ratio (SNR) of the received signals [2], and on the influence of tissue on the antenna sensitivity patterns [3]. Both of these aspects play an important role in understanding the structure of the received signal, of course, and are taken into account in signal optimization frameworks as shown in the recent work [4], for example. The influence of scattering currents, induced in biological tissue through the magnetization itself, however is neglected in research on this matter up till now.

Due to the relationship between the SNR and the MRI background field there is a continuing push to higher field strengths to achieve improved SNRs and faster scan times. These improvements do come at a cost as with higher field strengths also the frequency at which the MRI measurement is performed increases. This higher frequency leads to new challenges in radio frequency (RF) coil design, for example, and the received signals are generally more sensitive to changes in the dielectric (tissue) parameters as well.

In RF coil design a major challenge at higher fields is to achieve a uniform excitation of the region of interest (ROI). Since the size of the object is on the order of the wavelength, non-uniform RF fields and interference patterns may appear within the ROI. Possible solutions are increasing antenna array sizes and combining antenna types, although it has been demonstrated that such an approach has diminishing returns for larger array sizes [5]. Another approach is varying the array elements, using dipoles [6], combining loops and dipoles [7, 8], or using “special” fractionated dipoles [9]. In most of these approaches the goal is to optimize the so-called ultimate intrinsic signal to noise ratio (UISNR) or, in other words, to approximate ideal current patterns which would lead to the highest SNR [4]. Originally the term UISNR was introduced in [10], but additions have been made ever since, covering parallel MRI [11], current patterns required to attain this ratio [4], and addition of the specific absorption rate (SAR) [12].

For the SAR all the above-mentioned challenges are combined, as the higher heterogeneity of the RF fields leads to a local increase in tissue heating, which limits the amount of current that can be used to power a measurement and thus limits the SNR that can be obtained for a specific field strength and antenna array. Validated simulation techniques may be used to obtain more accurate local SAR estimates and may lead to antenna designs with reduced restrictions on the antenna currents that can be employed, or dielectric pads (passive shimming) can be used to improve the field homogeneity and reduce local heating effects [13].

In this paper, we focus on the signal modeling part and derive full-wave signal models based on Maxwell’s equations. Electric and magnetic field measurements are considered, and we show that the resulting signals are due to the time-varying magnetization inside the object and the induced electric scattering currents, each weighted by their own receive field as determined by the coil or antenna that is used for reception. The signal models can be explicitly evaluated provided the Green’s ten-

sors of the background medium and the medium parameters of the object are known. Moreover, to gain further insight into how the electromagnetic medium parameters of the object influence the measured signal, explicit time- and frequency-domain signal models are derived for a special case, where the background medium consists of air and the object is a homogeneous ball that is uniformly excited and for which the Born approximation applies. Quasi-static signal representations are derived from the full-wave signal models and through a series of numerical experiments we verify our models for the received signals. Finally, we demonstrate that under certain conditions it is possible to retrieve the dielectric parameters of the ball from measured free induction decay signals that are based on electric or magnetic field measurements.

We present our analysis in the Laplace- or s-domain, since it allows us to easily obtain frequency-domain solutions by letting $s \to \mathrm{j}\omega$ via the right-half of the complex s-plane, or time-domain field responses using standard Laplace transformation rules.

5.2. Theory

Let $\mathbb{D}_{\text{obj}}$ be a bounded domain occupied by a penetrable object that is present in an MR scanner. We assume that the complete object or part of this object has been excited during the transmit state of the scanner. More precisely, we assume that the temporal derivative of magnetization $\partial_t \boldsymbol{M}(\boldsymbol{x}, t)$ is nonzero within the subdomain $\mathbb{D}_{\text{ex}} \subseteq \mathbb{D}_{\text{obj}}$ and vanishes outside this domain. In other words, $\partial_t \boldsymbol{M}(\boldsymbol{x}, t)$ has the domain $\mathbb{D}_{\text{ex}}$ as its spatial support and $\mathbb{D}_{\text{ex}} = \mathbb{D}_{\text{obj}}$ if the complete object is excited.

Measurements are carried out outside the object and take place in free space. To set up the data models that describe our measurements, we first consider a surface S with unit normal $\boldsymbol{\nu}$ and closed boundary curve C with a unit normal $\boldsymbol{\tau}$ along this curve such that $\boldsymbol{\tau}$ and $\boldsymbol{\nu}$ are oriented according to the right-hand rule. The surface S has an area A and the position vector of its barycenter is denoted by $\boldsymbol{x}_{\text{R}}$. The surface is completely located in air and is used to measure the electromotive or magnetomotive force given by

$$\hat{V}_{\text{emf}}(s) = \int_{\boldsymbol{x} \in C} \hat{\boldsymbol{E}} \cdot \boldsymbol{\tau} \, \mathrm{d}\ell \quad \text{and} \quad \hat{I}_{\text{mmf}}(s) = \int_{\boldsymbol{x} \in C} \hat{\boldsymbol{H}} \cdot \boldsymbol{\tau} \, \mathrm{d}\ell, \tag{5.1}$$

respectively. Using Maxwell's equations and assuming that the area A of the surface is sufficiently small (diameter much smaller than the smallest wavelength of interest), we have

$$\hat{V}_{\text{emf}}(s) = -s \int_{\boldsymbol{x} \in S} \hat{\boldsymbol{B}} \cdot \boldsymbol{\nu} \, \mathrm{d}A \approx -s\mu_0 A \, \hat{\boldsymbol{H}}(\boldsymbol{x}_{\text{R}}, s) \cdot \boldsymbol{\nu}, \tag{5.2}$$

where we have used $\hat{\boldsymbol{B}} = \mu_0 \hat{\boldsymbol{H}}$, since the measurement surface S is located in air. Similarly, for the magnetomotive force we obtain

$$\hat{I}_{\text{mmf}}(s) = s \int_{\boldsymbol{x} \in S} \hat{\boldsymbol{D}} \cdot \boldsymbol{\nu} \, \mathrm{d}A \approx s\varepsilon_0 A \, \hat{\boldsymbol{E}}(\boldsymbol{x}_{\text{R}}, s) \cdot \boldsymbol{\nu}, \tag{5.3}$$

where we have used $\hat{\boldsymbol{D}} = \varepsilon_0 \hat{\boldsymbol{E}}$. Assuming that a measurement is linear and time-invariant, we can generalise our field measurement description to

$$\hat{d}_{\mathsf{h}}(s) = \int\limits_{\boldsymbol{x}\in\mathbb{D}_{\mathsf{rec}}} \hat{\boldsymbol{m}}_{\mathsf{h}}(\boldsymbol{x}, s) \cdot \hat{\boldsymbol{H}}(\boldsymbol{x}, s)\, \mathrm{d}V \tag{5.4}$$

and

$$\hat{d}_{\mathsf{e}}(s) = \int\limits_{\boldsymbol{x}\in\mathbb{D}_{\mathsf{rec}}} \hat{\boldsymbol{m}}_{\mathsf{e}}(\boldsymbol{x}, s) \cdot \hat{\boldsymbol{E}}(\boldsymbol{x}, s)\, \mathrm{d}V, \tag{5.5}$$

in which a volumetric receiver is used to obtain the measured signals. The receiver is completely located outside the object, occupies the receiver domain $\mathbb{D}_{\mathsf{rec}}$, and its action on the electromagnetic field inside the receiver domain is described by the vectorial receiver functions $\hat{\boldsymbol{m}}_{\mathsf{h}}$ and $\hat{\boldsymbol{m}}_{\mathsf{e}}$ for magnetic and electric field measurements, respectively. Note that the electro- and magnetomotive forces are special cases of (5.4) and (5.5). In particular, with

$$\hat{\boldsymbol{m}}_{\mathsf{h}}(s) = s\mu_0 A \delta(\boldsymbol{x} - \boldsymbol{x}_{\mathsf{R}})\boldsymbol{\nu}, \quad \text{and} \quad \hat{\boldsymbol{m}}_{\mathsf{e}}(s) = s\varepsilon_0 A \delta(\boldsymbol{x} - \boldsymbol{x}_{\mathsf{R}})\boldsymbol{\nu}, \tag{5.6}$$

we have $\hat{d}_{\mathsf{h}}(s) = -\hat{V}_{\mathsf{emf}}(s)$ and $\hat{d}_{\mathsf{e}}(s) = \hat{I}_{\mathsf{mmf}}(s)$. Since an electromotive force measurement is characterized by (5.4), we refer to such a measurement as a magnetic field measurement, while a magnetomotive force measurement is refered to as an electric field measurement, since it can be described by (5.5). Below, we take these general signal models as a starting point and consider the electro- and magnetomotive forces as special cases.

5.2.1. Scattering Formalism

To further develop the signal models (5.4) and (5.5), the magnetic and electric field strengths inside the receiver domain are obviously required. To this end, we set up a scattering formalism and write the electromagnetic field as a superposition of a background and a scattered field. The background field is defined as the field that is present when the constitutive parameters within the object domain are the same as the parameters of the background medium, while the scattered field takes the presence of the object into account. Assuming that the background can be accurately described by a background conductivity $\sigma_{\mathsf{b}}(\boldsymbol{x})$, a background permittivity $\varepsilon_{\mathsf{b}}(\boldsymbol{x})$, and a permeability $\mu_{\mathsf{b}}(\boldsymbol{x})$, the Laplace-domain background field satisfies the Maxwell equations

$$-\boldsymbol{\nabla} \times \hat{\boldsymbol{H}}^{\mathsf{b}} + \sigma_{\mathsf{b}} \hat{\boldsymbol{E}}^{\mathsf{b}} + s\varepsilon_{\mathsf{b}} \hat{\boldsymbol{E}}^{\mathsf{b}} = \boldsymbol{0}, \tag{5.7}$$

and

$$\boldsymbol{\nabla} \times \hat{\boldsymbol{E}}^{\mathsf{b}} + s\mu_{\mathsf{b}} \hat{\boldsymbol{H}}^{\mathsf{b}} = -\hat{\boldsymbol{K}}, \tag{5.8}$$

where $\hat{\boldsymbol{K}}$ is the Laplace transform of $\mu_0 \partial_t \boldsymbol{M}$ with $\boldsymbol{M}(\boldsymbol{x}, t)$ the time-varying magnetization with the domain $\mathbb{D}_{\text{ex}}$ as its spatial support. Across interfaces where the background medium parameters exhibit a jump, the above Maxwell equations have to be supplemented by the appropriate boundary conditions and if perfectly conducting structures are present in the background configuration, then the boundary condition for a perfectly conducting structure has to be included as well, of course. For general inhomogeneous background configurations that can be described in terms of the background medium parameters, the above Maxwell equations can only be solved numerically. Formally, however, we can express the electromagnetic background field in terms of the Green's tensors of the background medium as

$$\hat{\boldsymbol{H}}^{\text{b}}(\boldsymbol{x}, s) = \int\limits_{\boldsymbol{x}' \in \mathbb{D}_{\text{ex}}} \underline{\hat{\boldsymbol{G}}}^{\text{HK}}(\boldsymbol{x}, \boldsymbol{x}', s) \cdot \hat{\boldsymbol{K}}(\boldsymbol{x}', s)\, \mathrm{d}V \tag{5.9}$$

and

$$\hat{\boldsymbol{E}}^{\text{b}}(\boldsymbol{x}, s) = \int\limits_{\boldsymbol{x}' \in \mathbb{D}_{\text{ex}}} \underline{\hat{\boldsymbol{G}}}^{\text{EK}}(\boldsymbol{x}, \boldsymbol{x}', s) \cdot \hat{\boldsymbol{K}}(\boldsymbol{x}', s)\, \mathrm{d}V, \tag{5.10}$$

where $\underline{\hat{\boldsymbol{G}}}^{\text{HK}}$ and $\underline{\hat{\boldsymbol{G}}}^{\text{EK}}$ are the magnetic current to magnetic field and magnetic current to electric field Green's tensors of the background medium.

Furthermore, the scattered field $\{\hat{\boldsymbol{H}}^{\text{sc}}, \hat{\boldsymbol{E}}^{\text{sc}}\}$ satisfies the Maxwell equations

$$-\boldsymbol{\nabla} \times \hat{\boldsymbol{H}}^{\text{sc}} + \sigma_{\text{b}} \hat{\boldsymbol{E}}^{\text{sc}} + s\, \varepsilon_{\text{b}} \hat{\boldsymbol{E}}^{\text{sc}} = -\hat{\boldsymbol{J}}^{\text{sc}} \tag{5.11}$$

and

$$\boldsymbol{\nabla} \times \hat{\boldsymbol{E}}^{\text{sc}} + s\, \mu_{\text{b}} \hat{\boldsymbol{H}}^{\text{sc}} = \boldsymbol{0}, \tag{5.12}$$

where $\hat{\boldsymbol{J}}^{\text{sc}}$ is the Laplace transformed dielectric scattering source given by

$$\hat{\boldsymbol{J}}^{\text{sc}}(\boldsymbol{x}, s) = \{\sigma(\boldsymbol{x}) - \sigma_{\text{b}}(\boldsymbol{x}) + s[\varepsilon(\boldsymbol{x}) - \varepsilon_{\text{b}}(\boldsymbol{x})]\}\, \hat{\boldsymbol{E}}(\boldsymbol{x}, s) \tag{5.13}$$

for $\boldsymbol{x} \in \mathbb{D}_{\text{obj}}$, where $\sigma(\boldsymbol{x})$ is the conductivity of the object and $\varepsilon(\boldsymbol{x})$ its permittivity. The object is assumed to have no contrast in its permeability with respect to the background medium.

For the scattered field we have the integral representations

$$\hat{\boldsymbol{H}}^{\text{sc}}(\boldsymbol{x}, s) = \int\limits_{\boldsymbol{x}' \in \mathbb{D}_{\text{obj}}} \underline{\hat{\boldsymbol{G}}}^{\text{HJ}}(\boldsymbol{x}, \boldsymbol{x}', s) \cdot \hat{\boldsymbol{J}}^{\text{sc}}(\boldsymbol{x}', s)\, \mathrm{d}V \tag{5.14}$$

and

$$\hat{\boldsymbol{E}}^{\text{sc}}(\boldsymbol{x}, s) = \int\limits_{\boldsymbol{x}' \in \mathbb{D}_{\text{obj}}} \underline{\hat{\boldsymbol{G}}}^{\text{EJ}}(\boldsymbol{x}, \boldsymbol{x}', s) \cdot \hat{\boldsymbol{J}}^{\text{sc}}(\boldsymbol{x}', s)\, \mathrm{d}V, \tag{5.15}$$

where $\hat{\underline{G}}^{\mathsf{HJ}}$ and $\hat{\underline{G}}^{\mathsf{EJ}}$ are the electric current to magnetic field and electric current to electric field Green's tensors of the background medium. Having the integral representations for the background and scattered fields at our disposal, we can now further develop the full-wave signal models (5.4) and (5.5).

5.2.2. Full-Wave Signal Model

Writing the total magnetic and electric fields in the receiver domain as a superposition of the background and scattered fields and using the integral representations Equations (5.9), (5.10), (5.14) and (5.15), the signal models of Equations (5.4) and (5.5) become

$$\begin{aligned}\hat{d}_{\mathsf{h}}(s) = &\int_{\boldsymbol{x}\in\mathbb{D}_{\mathsf{ant}}} \hat{\boldsymbol{m}}_{\mathsf{h}}(\boldsymbol{x},s)\cdot\int_{\boldsymbol{x}'\in\mathbb{D}_{\mathsf{ex}}} \hat{\underline{G}}^{\mathsf{HK}}(\boldsymbol{x},\boldsymbol{x}',s)\cdot\hat{\boldsymbol{K}}(\boldsymbol{x}',s)\,\mathrm{d}V\,\mathrm{d}V\\ &+\int_{\boldsymbol{x}\in\mathbb{D}_{\mathsf{ant}}} \hat{\boldsymbol{m}}_{\mathsf{h}}(\boldsymbol{x},s)\cdot\int_{\boldsymbol{x}'\in\mathbb{D}_{\mathsf{obj}}} \hat{\underline{G}}^{\mathsf{HJ}}(\boldsymbol{x},\boldsymbol{x}',s)\cdot\hat{\boldsymbol{J}}^{\mathsf{sc}}(\boldsymbol{x}',s)\,\mathrm{d}V\,\mathrm{d}V\end{aligned} \tag{5.16}$$

and

$$\begin{aligned}\hat{d}_{\mathsf{e}}(s) = &\int_{\boldsymbol{x}\in\mathbb{D}_{\mathsf{ant}}} \hat{\boldsymbol{m}}_{\mathsf{e}}(\boldsymbol{x},s)\cdot\int_{\boldsymbol{x}'\in\mathbb{D}_{\mathsf{ex}}} \hat{\underline{G}}^{\mathsf{EK}}(\boldsymbol{x},\boldsymbol{x}',s)\cdot\hat{\boldsymbol{K}}(\boldsymbol{x}',s)\,\mathrm{d}V\,\mathrm{d}V\\ &+\int_{\boldsymbol{x}\in\mathbb{D}_{\mathsf{ant}}} \hat{\boldsymbol{m}}_{\mathsf{e}}(\boldsymbol{x},s)\cdot\int_{\boldsymbol{x}'\in\mathbb{D}_{\mathsf{obj}}} \hat{\underline{G}}^{\mathsf{EJ}}(\boldsymbol{x},\boldsymbol{x}',s)\cdot\hat{\boldsymbol{J}}^{\mathsf{sc}}(\boldsymbol{x}',s)\,\mathrm{d}V\,\mathrm{d}V.\end{aligned} \tag{5.17}$$

Interchanging the order of integration and using the reciprocity properties of the current to field Green's tensors [14] allows us to write the signal representations as

$$\hat{d}_{\mathsf{h}}(s) = \int_{\boldsymbol{x}'\in\mathbb{D}_{\mathsf{ex}}} \hat{\boldsymbol{K}}(\boldsymbol{x}',s)\cdot\hat{\boldsymbol{W}}_{\mathsf{h}}^{\mathsf{mg}}(\boldsymbol{x}',s)\,\mathrm{d}V - \int_{\boldsymbol{x}'\in\mathbb{D}_{\mathsf{obj}}} \hat{\boldsymbol{J}}^{\mathsf{sc}}(\boldsymbol{x}',s)\cdot\hat{\boldsymbol{W}}_{\mathsf{e}}^{\mathsf{mg}}(\boldsymbol{x}',s)\,\mathrm{d}V \tag{5.18}$$

and

$$\hat{d}_{\mathsf{e}}(s) = -\int_{\boldsymbol{x}'\in\mathbb{D}_{\mathsf{ex}}} \hat{\boldsymbol{K}}(\boldsymbol{x}',s)\cdot\hat{\boldsymbol{W}}_{\mathsf{h}}^{\mathsf{el}}(\boldsymbol{x}',s)\,\mathrm{d}V + \int_{\boldsymbol{x}'\in\mathbb{D}_{\mathsf{obj}}} \hat{\boldsymbol{J}}^{\mathsf{sc}}(\boldsymbol{x}',s)\cdot\hat{\boldsymbol{W}}_{\mathsf{e}}^{\mathsf{el}}(\boldsymbol{x}',s)\,\mathrm{d}V \tag{5.19}$$

where we have introduced the receive fields for a magnetic field measurement as

$$\hat{\boldsymbol{W}}_{\mathsf{h}}^{\mathsf{mg}}(\boldsymbol{x}',s) = \int_{\boldsymbol{x}\in\mathbb{D}_{\mathsf{rec}}} \hat{\underline{G}}^{\mathsf{HK}}(\boldsymbol{x}',\boldsymbol{x},s)\cdot\hat{\boldsymbol{m}}_{\mathsf{h}}(\boldsymbol{x},s)\,\mathrm{d}V, \tag{5.20}$$

and

$$\hat{\boldsymbol{W}}_{\mathsf{e}}^{\mathsf{mg}}(\boldsymbol{x}',s) = \int_{\boldsymbol{x}\in\mathbb{D}_{\mathsf{rec}}} \hat{\underline{G}}^{\mathsf{EK}}(\boldsymbol{x}',\boldsymbol{x},s)\cdot\hat{\boldsymbol{m}}_{\mathsf{h}}(\boldsymbol{x},s)\,\mathrm{d}V, \tag{5.21}$$

while the receive fields for an electric field measurement are given by

$$\hat{W}_{\mathrm{h}}^{\mathrm{el}}(\boldsymbol{x}', s) = \int_{\boldsymbol{x}\in\mathbb{D}_{\mathrm{rec}}} \underline{\hat{G}}^{\mathrm{HJ}}(\boldsymbol{x}', \boldsymbol{x}, s) \cdot \hat{\boldsymbol{m}}_{\mathrm{e}}(\boldsymbol{x}, s)\, \mathrm{d}V, \tag{5.22}$$

and

$$\hat{W}_{\mathrm{e}}^{\mathrm{el}}(\boldsymbol{x}', s) = \int_{\boldsymbol{x}\in\mathbb{D}_{\mathrm{rec}}} \underline{\hat{G}}^{\mathrm{EJ}}(\boldsymbol{x}', \boldsymbol{x}, s) \cdot \hat{\boldsymbol{m}}_{\mathrm{e}}(\boldsymbol{x}, s)\, \mathrm{d}V, \tag{5.23}$$

Equations (5.18) and (5.19) are the full-wave signal models for a magnetic and electric field measurement, respectively, in which the magnetic-current source (magnetization) and the scattering source contribute to the measured signal both weighted by their respective antenna receive fields. It can be confirmed that the magnetic field measurement simplifies to the traditional quasi-static signal model by referring to the receive field as $\boldsymbol{B}_1$ per MRI convention, and substituting the magnetisation into the magnetic source formulation $\hat{\boldsymbol{K}}$.

To evaluate these models, first the magnetization (and hence the magnetic-current source $\hat{\boldsymbol{K}}$) must be known within the excited part $\mathbb{D}_{\mathrm{ex}}$ of the object, since the time variations of this field quantity generate the radiated electromagnetic field. Second, the conductivity and permittivity profiles of the object must be known. This allows us to compute the electric field strength within the object by solving a forward problem with the magnetic-current density $\hat{\boldsymbol{K}}$ in $\mathbb{D}_{\mathrm{ex}}$ as a source. Finally, the Green's tensors of the background medium must be known as well to determine the receive fields in Equations (5.20) to (5.23). In general, these tensors can only be determined through simulations, since the background is inhomogeneous. In conclusion, the full-wave signals can be evaluated in principle, provided that (i) the magnetization in $\mathbb{D}_{\mathrm{ex}}$ is known, (ii) the conductivity and permittivity profiles of the object are known, and (iii) the Green's tensors of the background medium are known. Note that frequency-domain responses are obtained by letting $s \to \mathrm{j}\omega$ and time-domain signal responses involve temporal convolutions of the magnetic-current source and the dielectric scattering source with their respective receive fields, since their Laplace-domain counterparts all are s-dependent in general.

5.2.3. Simplified Full-Wave Signal Models for a Ball Located in Free-Space

Given the above observations, we consider a specific configuration for which it is possible to develop signal models that explicitly show how the received signals depend on the conductivity and permittivity of the object. In particular, we first consider a background medium consisting of free space. The Green's tensors of the background medium and the receive fields for electro- or magnetomotive force measurements (dipole measurements) can then be determined explicitly. Second, we take a small homogeneous ball with a constant conductivity σ and permittivity ε as our object of interest. Explicit signal models can then be developed provided the radius of the ball is sufficiently small.

Let the background medium be free space and consider an electro- or magnetomotive force measurement. For an electromotive force measurement, the receive function $\hat{\boldsymbol{m}}_{\mathsf{h}}$ is given by Equation (5.6) and since the background medium is free space, the Green's tensors are explicitly known [14] and the receive fields follow as

$$\begin{aligned}\hat{\boldsymbol{W}}_{\mathsf{h}}^{\mathsf{mg}}(\boldsymbol{x}', s) &= s\mu_0 A \hat{\underline{\boldsymbol{G}}}^{\mathsf{HK}}(\boldsymbol{x}', \boldsymbol{x}_{\mathsf{R}}, s) \cdot \boldsymbol{\nu} \\ &= \frac{A}{4\pi\mathcal{R}^3} \exp(-s\tau) \left[(1 + s\tau)\boldsymbol{p}_1 + (s\tau)^2 \boldsymbol{p}_2\right]\end{aligned} \tag{5.24}$$

and

$$\begin{aligned}\hat{\boldsymbol{W}}_{\mathsf{e}}^{\mathsf{mg}}(\boldsymbol{x}', s) &= s\mu_0 A \hat{\underline{\boldsymbol{G}}}^{\mathsf{EK}}(\boldsymbol{x}', \boldsymbol{x}_{\mathsf{R}}, s) \cdot \boldsymbol{\nu} \\ &= \frac{s\mu_0 A}{4\pi\mathcal{R}^2} \exp(-s\tau)(1 + s\tau)\boldsymbol{n} \times \boldsymbol{\nu},\end{aligned} \tag{5.25}$$

where $\tau = c_0^{-1}\mathcal{R}$ with c_0 is the electromagnetic wave speed in vacuum. Clearly, τ is the travel time from the point of integration $\boldsymbol{x}'$ to the receiver location $\boldsymbol{x}_{\mathsf{R}}$. Furthermore, $\boldsymbol{p}_1 = 3\boldsymbol{n}(\boldsymbol{n} \cdot \boldsymbol{\nu}) - \boldsymbol{\nu}$, and $\boldsymbol{p}_2 = \boldsymbol{n}(\boldsymbol{n} \cdot \boldsymbol{\nu}) - \boldsymbol{\nu}$ with $\boldsymbol{n} = (\boldsymbol{x}' - \boldsymbol{x}_{\mathsf{R}})/\mathcal{R}$ the unit vector pointing from the receiver location to the point of integration, and $\mathcal{R} = |\boldsymbol{x}' - \boldsymbol{x}_R|$ the distance of receiver location to the point of integration.

Similarly, for a magnetomotive force measurement, the receive function $\hat{\boldsymbol{m}}_{\mathsf{e}}$ is given by Equation (5.6) and the receive fields follow as

$$\begin{aligned}\hat{\boldsymbol{W}}_{\mathsf{h}}^{\mathsf{el}}(\boldsymbol{x}, s) &= s\varepsilon_0 A \hat{\underline{\boldsymbol{G}}}^{\mathsf{HJ}}(\boldsymbol{x}, \boldsymbol{x}_{\mathsf{R}}, s) \cdot \boldsymbol{\nu} \\ &= -\frac{s\varepsilon_0 A}{4\pi\mathcal{R}^2} \exp(-s\tau)(1 + s\tau)\boldsymbol{n} \times \boldsymbol{\nu},\end{aligned} \tag{5.26}$$

and

$$\begin{aligned}\hat{\boldsymbol{W}}_{\mathsf{e}}^{\mathsf{el}}(\boldsymbol{x}, s) &= s\varepsilon_0 A \hat{\underline{\boldsymbol{G}}}^{\mathsf{EJ}}(\boldsymbol{x}, \boldsymbol{x}_{\mathsf{R}}, s) \cdot \boldsymbol{\nu} \\ &= \frac{A}{4\pi\mathcal{R}^3} \exp(-s\tau) \left[(1 + s\tau)\boldsymbol{p}_1 + (s\tau)^2 \boldsymbol{p}_2\right].\end{aligned} \tag{5.27}$$

Note that $\hat{\boldsymbol{W}}_{\mathsf{e}}^{\mathsf{mg}}$ and $\hat{\boldsymbol{W}}_{\mathsf{h}}^{\mathsf{el}}$ are proportional to each other and $\hat{\boldsymbol{W}}_{\mathsf{h}}^{\mathsf{mg}} = \hat{\boldsymbol{W}}_{\mathsf{e}}^{\mathsf{el}}$.

Second, we take a small ball as our object of interest. The ball is centered at the origin of our reference frame and has a radius $a > 0$. It is characterized by a constant conductivity σ and permittivity ε, and its permeability is equal to that of free space. We assume that the radius a is so small that the ball is excited throughout ($\mathbb{D}_{\mathsf{ex}} = \mathbb{D}_{\mathsf{obj}}$) and time variations of the magnetization (and hence the magnetic-current source $\hat{\boldsymbol{K}}$) are uniform, that is, $\hat{\boldsymbol{K}}$ does not vary with position within the ball. For a given magnetization, the magnetic-current source is now known and the total electric field within the ball can be computed by solving the integral equation

$$\hat{\boldsymbol{E}}(\boldsymbol{x}', s) = \hat{\boldsymbol{E}}^{\mathsf{b}}(\boldsymbol{x}', s) - \hat{\chi}(\hat{\gamma}_0^2 - \boldsymbol{\nabla}\boldsymbol{\nabla}\cdot) \int\limits_{\boldsymbol{x}' \in \mathbb{D}_{\mathsf{obj}}} \hat{G}(\boldsymbol{x} - \boldsymbol{x}', s)\hat{\boldsymbol{E}}(\boldsymbol{x}', s)\, \mathrm{d}V, \tag{5.28}$$

for the electric field $\hat{\boldsymbol{E}}(\boldsymbol{x}', s)$ with $\boldsymbol{x}' \in \mathbb{D}_{\text{obj}}$. In the above equation, $\hat{\gamma}_0 = s/c_0$ is the propagation coefficient of free space, $\hat{\chi} = \varepsilon_{\text{r}} - 1 + \sigma/(s\varepsilon_0)$ is the contrast of the ball, $\hat{G}$ is the scalar Green's function of free space, and $\hat{\boldsymbol{E}}^{\text{b}}$ can be determined from Equation (5.10), since $\hat{\boldsymbol{K}}$ is known. In the next section, we will essentially follow such an approach, except that we will determine the electric field in the time-domain using finite difference time domain (FDTD) for a given magnetization. Here, we use the above integral equation to arrive at the desired signal models. Specifically, let us consider frequencies of operation s and a ball of radius a with conductivity and permittivity values σ and ε, respectively, such that the condition

$$(2a\,|\hat{\gamma}_0|)^2\,|\hat{\chi}| \ll 1 \tag{5.29}$$

is satisfied. For three-dimensional scalar wave field problems, this is a sufficient condition for the Neumann series to converge [15, 16]. In addition, let us assume that there is (essentially) no charge accumulation at the boundary of the ball. The gradient-divergence term is then negligible and the above integral equation turns into a scalar integral equation for the electric field. Moreover, since we consider frequencies and dielectric parameters for which Equation (5.29) holds, we may approximate

$$\hat{\boldsymbol{E}}(\boldsymbol{x}', s) \approx \hat{\boldsymbol{E}}^{\text{b}}(\boldsymbol{x}', s). \tag{5.30}$$

Now provided the quasi-static condition $|2a\hat{\gamma}_0| \ll 1$ is also satisfied, this background field is essentially given by

$$\hat{\boldsymbol{E}}^{\text{b}}(\boldsymbol{x}', s) = -\frac{1}{3}\hat{\boldsymbol{K}} \times \boldsymbol{x}' \tag{5.31}$$

with $\boldsymbol{x}' \in \mathbb{D}_{\text{obj}}$. Notice that this background field does not have a radial component, which is consistent with our assumption of no charge accumulation at the boundary. Also, note that if the quasi-static condition $|2a\hat{\gamma}_0| \ll 1$ holds, then Equation (5.29) can be satisfied for $|\hat{\chi}| \gg 1$ [16].

Provided the quasi-static and Born approximation hold, the dielectric scattering source within the ball is given by

$$\begin{aligned} \hat{\boldsymbol{J}}^{\text{sc}}(\boldsymbol{x}', s) &= [\sigma + s(\varepsilon - \varepsilon_0)]\hat{\boldsymbol{E}}(\boldsymbol{x}', s) \\ &= -\frac{1}{3}[\sigma + s(\varepsilon - \varepsilon_0)]\hat{\boldsymbol{K}}(s) \times \boldsymbol{x}', \end{aligned} \tag{5.32}$$

for $\boldsymbol{x}' \in \mathbb{D}_{\text{obj}}$. Substitution in Equations (5.18) and (5.19), we obtain the signal models

$$\hat{d}_{\text{h}}(s) = \hat{\boldsymbol{K}}(s) \cdot \int_{\boldsymbol{x}' \in \mathbb{D}_{\text{obj}}} \hat{\boldsymbol{S}}^{\text{mg}}(\boldsymbol{x}', s)\,\mathrm{d}V \tag{5.33}$$

and

$$\hat{d}_{\text{e}}(s) = -\hat{\boldsymbol{K}}(s) \cdot \int_{\boldsymbol{x}' \in \mathbb{D}_{\text{obj}}} \hat{\boldsymbol{S}}^{\text{el}}(\boldsymbol{x}', s)\,\mathrm{d}V, \tag{5.34}$$

5

where the vectorial sensitivity functions are given by

$$\hat{S}^{\mathrm{mg}}(x', s) = \hat{W}_{\mathrm{h}}^{\mathrm{mg}} + \hat{\chi}_{\mathrm{e}} x' \times \hat{W}_{\mathrm{e}}^{\mathrm{mg}} \tag{5.35}$$

and

$$\hat{S}^{\mathrm{el}}(x', s) = \hat{W}_{\mathrm{h}}^{\mathrm{el}} + \hat{\chi}_{\mathrm{e}} x' \times \hat{W}_{\mathrm{e}}^{\mathrm{el}} \tag{5.36}$$

with $\hat{\chi}_{\mathrm{e}} = [\sigma + s(\varepsilon - \varepsilon_0)]/3 = s\varepsilon_0\hat{\chi}/3$. Substituting expressions Equations (5.24) to (5.27) for the receive fields in the above equations and applying an inverse Laplace transformation, we obtain the time-domain signals

$$d_{\mathrm{h}}(t) = \mu_0 \partial_t M(t) \overset{t}{*} \int\limits_{x' \in \mathbb{D}_{\mathrm{obj}}} S^{\mathrm{mg}}(x', t - \tau)\, \mathrm{d}V, \tag{5.37}$$

and

$$d_{\mathrm{e}}(t) = -\mu_0 \partial_t M(t) \overset{t}{*} \int\limits_{x' \in \mathbb{D}_{\mathrm{obj}}} S^{\mathrm{el}}(x', t - \tau)\, \mathrm{d}V, \tag{5.38}$$

for $t > 0$, where the asterisk denotes convolution in time and the time-domain sensitivity functions are given by

$$S^{\mathrm{mg}}(x', t) = \frac{A}{4\pi\mathcal{R}^3} \sum_{k=0}^{3} \tau^k \delta^{(k)}(t) r_k^{\mathrm{mg}} \tag{5.39}$$

and

$$S^{\mathrm{el}}(x', t) = \frac{A}{4\pi\mathcal{R}^3} \sum_{k=0}^{3} \tau^k \delta^{(k)}(t) r_k^{\mathrm{el}}, \tag{5.40}$$

where $\delta^{(k)}$ is the kth derivative of the Dirac distribution. Explicit expressions for the expansion vectors $r_k^{\mathrm{mg,el}}$, $k = 0, 1, 2, 3$, are given in the Appendix.

In the above signal models, propagation effects and travel times from the ball to the receiver are fully taken into account. However, when the receivers are located not too far from the ball (in a sense to be made precise) then the signals may be simplified even further. To this end, we substitute the receive fields of Equations (5.24) to (5.27) in Equations (5.35) and (5.36) and arrange the resulting expressions in such a way that the sensitivities are expanded in terms of vectors that do not depend on the distance $\mathcal{R}$. Carrying out these steps, we find for the magnetic field sensitivity function

$$\hat{S}^{\mathrm{mg}}(x', s) = \frac{Ae^{-s\tau}}{4\pi\mathcal{R}^3} \cdot \left[p_1 + (s\tau)(p_1 + \hat{q}^{\mathrm{mg}}) + (s\tau)^2 (p_2 + \hat{q}^{\mathrm{mg}}) \right], \tag{5.41}$$

while for the sensitivity function for an electric field measurement, we have

$$\hat{S}^{\mathrm{el}}(x', s) = \frac{Ae^{-s\tau}}{4\pi\mathcal{R}^3} \cdot \left[\hat{\chi}_{\mathrm{e}} p_1' + (s\tau)(\hat{\chi}_{\mathrm{e}} p_1' + Y_0 q^{\mathrm{el}}) + (s\tau)^2 (\hat{\chi}_{\mathrm{e}} p_2' + Y_0 q^{\mathrm{el}}) \right] \tag{5.42}$$

with $\hat{\boldsymbol{q}}^{\mathsf{mg}} = Z_0\hat{\chi}_{\mathsf{e}}[(\boldsymbol{x}'\cdot\boldsymbol{v})\boldsymbol{n} - (\boldsymbol{x}'\cdot\boldsymbol{n})\boldsymbol{v}]$, $\boldsymbol{q}^{\mathsf{el}} = \boldsymbol{v}\times\boldsymbol{n}$, and $\boldsymbol{p}'_{1,2} = \boldsymbol{x}'\times\boldsymbol{p}_{1,2}$ respectively. Note that the vectors

$$\boldsymbol{p}_{1,2} + \hat{\boldsymbol{q}}^{\mathsf{mg}} \quad \text{and} \quad \hat{\chi}_{\mathsf{e}}\boldsymbol{x}'\times\boldsymbol{p}_{1,2} + Y_0\boldsymbol{q}^{\mathsf{el}} \tag{5.43}$$

are s-dependent, but do not depend on $\mathcal{R}$. We can now use the above expressions to investigate which terms contribute to the received signals measured at different receiver locations. Specifically, let us first consider the case where we place the receiver near (almost at) the surface of the ball ($|\boldsymbol{x}_{\mathsf{R}}| = a(1+\epsilon)$, with $\epsilon > 0$ small). In this case, $|s|\,\tau \leq |\hat{\gamma}_0 2a| \ll 1$ and the receive field can be considered quasi-static. The signals models simplify to

$$\begin{aligned}
&\hat{d}_{\mathsf{h}}(s) \approx \hat{d}_{\mathsf{h}}^{\mathsf{QS}}(s)\\
&\hat{d}_{\mathsf{h}}^{\mathsf{QS}}(s) = \frac{A}{4\pi}\left[\hat{\boldsymbol{K}}\cdot\int\limits_{\boldsymbol{x}'\in\mathbb{D}_{\mathsf{obj}}}\frac{\boldsymbol{p}_1}{\mathcal{R}^3}\,\mathrm{d}V + s\mu_0\hat{\chi}_{\mathsf{e}}\hat{\boldsymbol{K}}\cdot\int\limits_{\boldsymbol{x}'\in\mathbb{D}_{\mathsf{obj}}}\frac{(\boldsymbol{x}'\cdot\boldsymbol{v})\boldsymbol{n} - (\boldsymbol{x}'\cdot\boldsymbol{n})\boldsymbol{v}}{\mathcal{R}^2}\,\mathrm{d}V\right]
\end{aligned} \tag{5.44}$$

and

$$\begin{aligned}
&\hat{d}_{\mathsf{e}}(s) \approx \hat{d}_{\mathsf{e}}^{\mathsf{QS}}(s)\\
&\hat{d}_{\mathsf{e}}^{\mathsf{QS}}(s) = -\frac{A}{4\pi}\left[\hat{\chi}_{\mathsf{e}}\hat{\boldsymbol{K}}\cdot\int\limits_{\boldsymbol{x}'\in\mathbb{D}_{\mathsf{obj}}}\frac{\boldsymbol{x}'\times\boldsymbol{p}_1}{\mathcal{R}^3}\,\mathrm{d}V + s\varepsilon_0\hat{\boldsymbol{K}}\cdot\int\limits_{\boldsymbol{x}'\in\mathbb{D}_{\mathsf{obj}}}\frac{\boldsymbol{v}\times\boldsymbol{n}}{\mathcal{R}^2}\,\mathrm{d}V\right]
\end{aligned} \tag{5.45}$$

and their time-domain counterparts are given by

$$\begin{aligned}
d_{\mathsf{h}}^{\mathsf{QS}}(t) = \frac{\mu_0 A}{4\pi}\Bigg[&\partial_t\boldsymbol{M}\cdot\int\limits_{\boldsymbol{x}'\in\mathbb{D}_{\mathsf{obj}}}\frac{\boldsymbol{p}_1}{\mathcal{R}^3}\,\mathrm{d}V\\
&+\frac{\sigma\mu_0}{3}\partial_t^2\boldsymbol{M}\cdot\int\limits_{\boldsymbol{x}'\in\mathbb{D}_{\mathsf{obj}}}\frac{[(\boldsymbol{x}'\cdot\boldsymbol{v})\boldsymbol{n} - (\boldsymbol{x}'\cdot\boldsymbol{n})\boldsymbol{v}]}{\mathcal{R}^2}\,\mathrm{d}V\\
&+\frac{\varepsilon_{\mathrm{r}}-1}{3}\frac{1}{c_0^2}\partial_t^3\boldsymbol{M}\cdot\int\limits_{\boldsymbol{x}'\in\mathbb{D}_{\mathsf{obj}}}\frac{[(\boldsymbol{x}'\cdot\boldsymbol{v})\boldsymbol{n} - (\boldsymbol{x}'\cdot\boldsymbol{n})\boldsymbol{v}]}{\mathcal{R}^2}\,\mathrm{d}V\Bigg]
\end{aligned} \tag{5.46}$$

and

$$d_{\mathsf{e}}^{\mathsf{QS}}(t) = -\frac{\mu_0 A}{4\pi}\left[\frac{\sigma}{3}\partial_t \boldsymbol{M} \cdot \int\limits_{\boldsymbol{x}'\in\mathbb{D}_{\mathsf{obj}}} \frac{\boldsymbol{x}'\times\boldsymbol{p}_1}{\mathcal{R}^3}\,\mathrm{d}V + \frac{\varepsilon_{\mathrm{r}}-1}{3}\varepsilon_0\partial_t^2\boldsymbol{M} \cdot \int\limits_{\boldsymbol{x}'\in\mathbb{D}_{\mathsf{obj}}} \frac{\boldsymbol{x}'\times\boldsymbol{p}_1}{\mathcal{R}^3}\,\mathrm{d}V + \varepsilon_0\partial_t^2\boldsymbol{M} \cdot \int\limits_{\boldsymbol{x}'\in\mathbb{D}_{\mathsf{obj}}} \frac{\boldsymbol{\nu}\times\boldsymbol{n}}{\mathcal{R}^2}\,\mathrm{d}V\right], \tag{5.47}$$

for $t > 0$ explicitly showing that time variations of the magnetization are received without any propagation delay in the quasi-static limit. We observe that for a magnetic field measurement, the conductivity and permittivity are still present in the intermediate-field contribution to the signal ($1/\text{distance}^2$ term), while for an electric field measurement the dielectric properties of the ball show up even in the near field contribution to the signal ($1/\text{distance}^3$ term).

As we move away from the ball, the travel time τ will obviously increase. The above quasi-static signal models remain valid, however, provided that $|s|\,\tau \ll 1$ for all $\boldsymbol{x}' \in \mathbb{D}_{\mathsf{obj}}$. Obviously, the quasi-static signal models can no longer be used as soon as this inequality is not satisfied.

Finally, for later convenience we write the quasi-static signals as

$$d_{\mathsf{h}}^{\mathsf{QS}}(t) = \partial_t \boldsymbol{M} \cdot \boldsymbol{a}_1^{\mathsf{h}}(\boldsymbol{x}_{\mathsf{R}}) + \frac{\sigma\mu_0}{3}\,\partial_t^2\boldsymbol{M} \cdot \boldsymbol{a}_2^{\mathsf{h}}(\boldsymbol{x}_{\mathsf{R}}) + \frac{\varepsilon_{\mathrm{r}}-1}{3}\frac{1}{c_0^2}\,\partial_t^3\boldsymbol{M} \cdot \boldsymbol{a}_2^{\mathsf{h}}(\boldsymbol{x}_{\mathsf{R}}) \tag{5.48}$$

and

$$d_{\mathsf{e}}^{\mathsf{QS}}(t) = \frac{\sigma}{3}\partial_t \boldsymbol{M} \cdot \boldsymbol{a}_1^{\mathsf{e}}(\boldsymbol{x}_{\mathsf{R}}) + \frac{\varepsilon_{\mathrm{r}}-1}{3}\varepsilon_0\,\partial_t^2\boldsymbol{M} \cdot \boldsymbol{a}_1^{\mathsf{e}}(\boldsymbol{x}_{\mathsf{R}}) + \varepsilon_0\,\partial_t^2\boldsymbol{M} \cdot \boldsymbol{a}_2^{\mathsf{e}}(\boldsymbol{x}_{\mathsf{R}}), \tag{5.49}$$

where the expressions for the expansion vectors $\boldsymbol{a}_k^{\mathsf{e,h}}(\boldsymbol{x}_{\mathsf{R}})$, $k = 1, 2$, are easily obtained from Equations (5.46) and (5.47).

5.3. Simulations

To test the validity of our signal models and to study the influence of the permittivity and conductivity of the ball on these signals, we consider the configuration illustrated in Figure 5.1. In this configuration, all geometrical parameters are fixed and wavelength independent, since we want to investigate this setup in MR scanners with different background fields. In particular, the radius of the ball is set to $a = 2.5$ cm, and we use three receivers located on the x-axis to measure the various field responses. With Receiver 1 we carry out surface measurements, and in our simulations this receiver is located at a distance $d_1 = 2.5 \times 10^{-6}$ cm from the ball. Receiver 2 is located at a distance $d_2 = 25$ cm from the ball and, finally, Receiver 3 is located at a distance $d_3 = 50$ cm from the ball. All three receivers are loops that have a circular

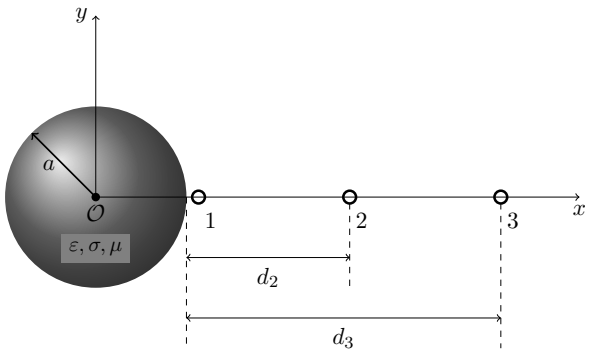

Figure 5.1: Free induction decay signal measurement setup. A homogeneous ball with a radius a, centered at the origin has a permittivity ε, conductivity σ, and permeability μ. Relaxation times T_1 and T_2.

Table 5.1: Dielectric medium parameters of white matter for different background fields [18, 19].

B_0 [T]	1.5	3	7	11.2
σ [S/m]	0.3	0.3	0.4	0.5
ε_r	68	53	44	41

surface area with a radius of 2 cm. When we carry out a magnetic field measurement (emf), the loop is oriented in the x-direction ($\boldsymbol{\nu} = \hat{\boldsymbol{\imath}}_x$), while for an electric field measurement (mmf) we orient the loop in the z-direction ($\boldsymbol{\nu} = \hat{\boldsymbol{\imath}}_z$). The signal models will be evaluated for background fields of 1.5 T, 3 T, 7 T and 11.2 T. The ball that we consider consists of white matter and its conductivity and relative permittivity values at the Larmor frequencies that correspond to these background fields are listed in Table 5.1. In all cases, the relative permeability is taken to be equal to one. For the relaxation times of white matter we take those of a 3 T background field, $T_1 = 900$ ms and $T_2 = 75$ ms [17], and we use these values for all background fields under consideration.

The signals that we receive are free induction decay (FID) signals as generated by the time-varying magnetization

$$M_x(t) = \quad M^{\text{eq}} e^{-t/T_2} \cos(\omega_0 t) \tag{5.50}$$

$$M_y(t) = -M^{\text{eq}} e^{-t/T_2} \sin(\omega_0 t) \tag{5.51}$$

and

$$M_z(t) = M^{\text{eq}}(1 - e^{-t/T_1}), \tag{5.52}$$

where $\omega_0 = \gamma B_0$ is the Larmor frequency, T_1 and T_2 are the longitudinal and transverse relaxation times, respectively, and M^{eq} is the equilibrium magnetization. For a proton spin density $\rho = 6.69 \times 10^{28}$ m^{-3} (water) and at $T = 310.15$ K, the equilibrium magnetization evaluates to $M^{\text{eq}} \approx 0.0031 B_0$. The above components of the magnetization form the solution of the Bloch equation with initial condition $\boldsymbol{M}(0) = M^{\text{eq}} \hat{\boldsymbol{\imath}}_x$.

For $t > 0$, the above solution describes how the magnetization relaxes back to its equilibrium $\boldsymbol{M} = M^{\text{eq}}\hat{\boldsymbol{\imath}}_z$ as time increases.

5.3.1. Validating the Born approximation

Before we carry out our signal analysis, we first validate the Born approximation for all background fields under consideration, since our signal models are based on this approximation. Specifically, we compute the time-domain electromagnetic field due to the magnetization given by Equations (5.50) to (5.52) using an in-house uniaxial perfectly matched layer (UPML)-FDTD code. In our FDTD model, the conductivity and permittivity values of the ball at the various Larmor frequencies are selected according to Table 5.1. Subsequently, we use the computed FDTD field responses to determine the electromotive force V_{emf} as measured by a receiver located at $\boldsymbol{x}_{\text{R}} = [3.2\,\text{cm}, 0, 0]$. The dashed lines in Figure 5.2 show the resulting signals for various background fields. The solid lines in this figure depict the signal model of (5.37) at the same receiver location and for the same background fields. This latter model is based on the quasi-static Born approximation (5.30) and (5.31), while obviously no such approximation has been applied in our FDTD simulations. From Figure 5.2 we observe that the signals based on FDTD modeling and the signals based on the quasi-static Born approximation overlap thereby validating that for this configuration and for all background fields of interest, the Born approximation indeed provides us with an accurate signal description.

5

5.3.2. Quasi-Static Signal Analysis

In the Laplace-domain, the quasi-static signal models hold provided that the condition $|s|\,\tau \ll 1$ is satisfied for all $\boldsymbol{x}' \in \mathbb{D}_{\text{obj}}$ and all frequencies s of interest. For the FID signals as generated by the magnetization of Equations (5.50) to (5.52), the Larmor frequency is the only non-vanishing oscillation frequency, and we can set $s = \text{j}\omega_0$ in the above condition to obtain the quasi-static requirement that $2\pi\lambda_0^{-1}\mathcal{R} \ll 1$ should hold for all $\boldsymbol{x}' \in \mathbb{D}_{\text{obj}}$, where λ_0 is the wavelength in free space.

Introducing the maximum distance $d_{\text{max}} = \max_{\boldsymbol{x}' \in \mathbb{D}_{\text{obj}}} \mathcal{R}$, the quasi-static condition is satisfied if $2\pi d_{\text{max}}/\lambda_0 \ll 1$. Table 5.2 lists $2\pi d_{\text{max}}/\lambda_0$ for the three receivers mentioned above and for different background fields. From this table, we expect the quasi-static approximation to hold for Receiver 1 and essentially all background fields under consideration. For Receiver 2, the quasi-static signal models are expected to hold for 1.5 T and possibly 3 T background fields, while for Receiver 3 the quasi-static field approximation possibly holds at 1.5 T only. Figures 5.3 and 5.5 show the full wave signal model of (5.37) (solid line) and the quasi-static signal model of (5.46) (dashed line) for the electromotive force V_{emf} at the three receivers of Figure 5.1. Since a quasi-static electromotive or magnetomotive force signal analysis leads to the same conclusions, we present results for the electromotive force only.

From Figures 5.3 to 5.5 we observe that the quasi-static parameters of Table 5.2 quite accurately predict when a quasi-static signal model can be used. Specifically, for Receiver 1 the value of $2\pi d_{\text{max}}/\lambda_0$ is at or below 0.5 for all background fields and Figure 5.3 shows that the full and quasi-static signals essentially overlap. For Receiver 2, however, we observe that the quasi-static model overlaps with the full-

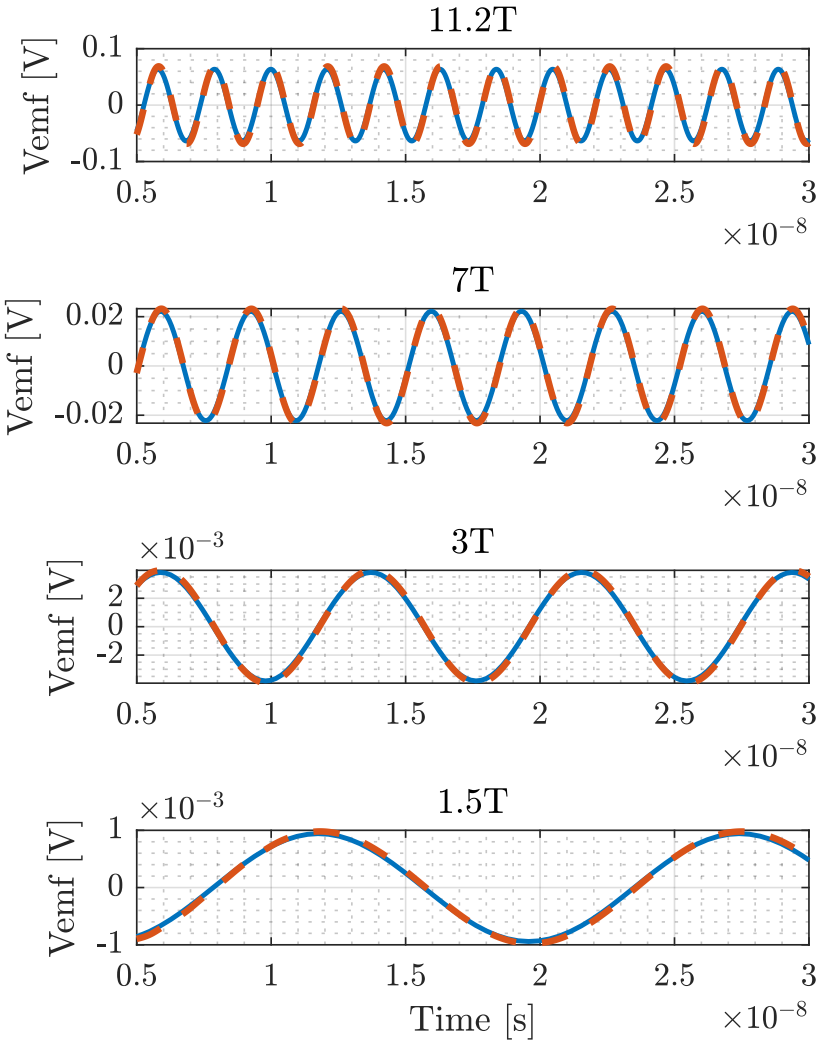

Figure 5.2: Validation of the Born approximation for various background fields. Dashed (red) lines: V_{emf} as determined from the magnetic field of the FDTD simulation. Solid (blue) line: the signal model of Equation (5.37). The receiver is located at $x_{\text{R}} = [3.2\,\text{cm}, 0, 0]$ and the medium parameters of the ball are listed in Table 5.1.

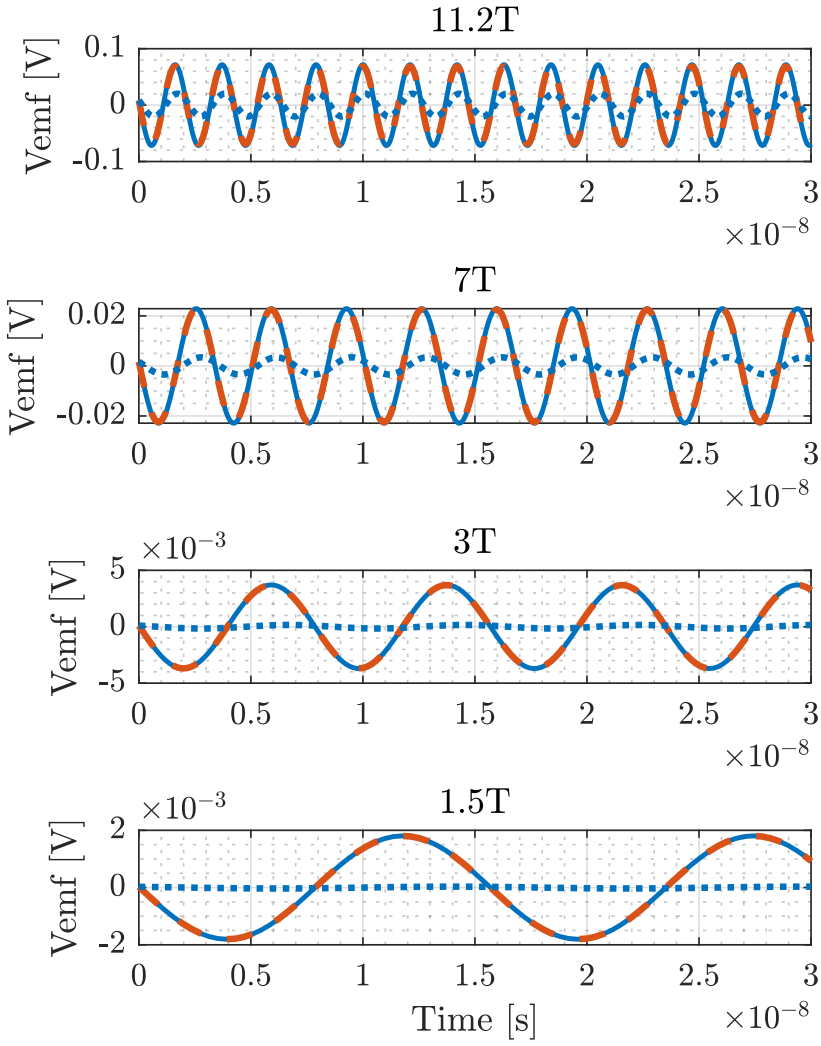

Figure 5.3: Electromotive force at Receiver 1 for various background field strengths and a ball of white matter. The dielectric parameters are listed in Table 5.1. Solid line: full wave signal model of Equation (5.37); dashed line: quasi-static signal model of Equation (5.46); dotted line: sum of the last two terms on the right-hand side of Equation (5.46).

Table 5.2: Background fields and normalized distances.

B_0 [T]	1.5	3	7	11.2
λ_0 [m]	4.69	2.35	1.01	0.63
$2a/\lambda_0$	0.01	0.02	0.05	0.08
Rec. 1: $2\pi d_{\max}/\lambda_0$	0.07	0.13	0.31	0.5
Rec. 2: $2\pi d_{\max}/\lambda_0$	0.40	0.80	1.87	3.00
Rec. 3: $2\pi d_{\max}/\lambda_0$	0.74	1.47	3.44	5.50

wave model for a background field of 1.5 T, but starts to deviate from the full-wave model for a background field of 3 T. For even higher background fields the quasi-static model is no longer valid, which is consistent with Table 5.2, since $2\pi d_{\max}/\lambda_0$ is larger than one in this case. These results indicate that the quasi-static signal model coincides with the full-wave model as long as $2\pi d_{\max}/\lambda_0 \leq 0.5$. This observation is consistent with the full-wave and quasi-static signal models for Receiver 3 shown in Figure 5.5. In this case, the quasi-static signal model already deviates from the full-wave model for a background field of 1.5 T for which we have $2\pi d_{\max}/\lambda_0 \approx 0.74$. For higher background fields the quasi-static signal approximation definitely does not hold at Receiver 3, and we have to resort to the full-wave model of Equation (5.46) in this case.

Finally, the dotted lines in Figures 5.3 to 5.5 show the contribution of the conductivity and permittivity terms (the last two terms on the right-hand side of Equation (5.46)) to the total quasi-static signal Equation (5.46). We also observe that the contribution of these terms is small for lower background fields, but increases as the background field strength increases. Consequently, the conductivity and permittivity of the ball can be retrieved from a quasi-static electromotive force measurement, provided the SNR of the signals and the background field strengths are sufficiently large and the quasi-static field approximation holds. Another option is, of course, to use an electric field measurement (magnetomotive force measurement) as a basis for conductivity and permittivity retrieval, since for such a measurement these quantities contribute to the signal via the near-field as opposed to an electromotive force measurement, where the medium parameters contribute to the signal via the intermediate field.

5.3.3. Conductivity and Permittivity Retrieval

Since the quasi-static signal models under the Born approximation are all valid for measurements carried out with Receiver 1 (surface measurement) and all background fields of interest, we now use these models at this receiver location to retrieve the conductivity and permittivity of the ball (white matter).

Let us start with the signal model for a magnetic field measurement given by Equation (5.48). Introducing the functions $d_1^{\mathrm{h}}(t) = \partial_t \boldsymbol{M} \cdot \boldsymbol{a}_1^{\mathrm{h}}(\boldsymbol{x}_{\mathrm{R}})$, $d_2^{\mathrm{h}}(t) = \mu_0 \partial_t^2 \boldsymbol{M} \cdot \boldsymbol{a}_2^{\mathrm{h}}(\boldsymbol{x}_{\mathrm{R}})$,

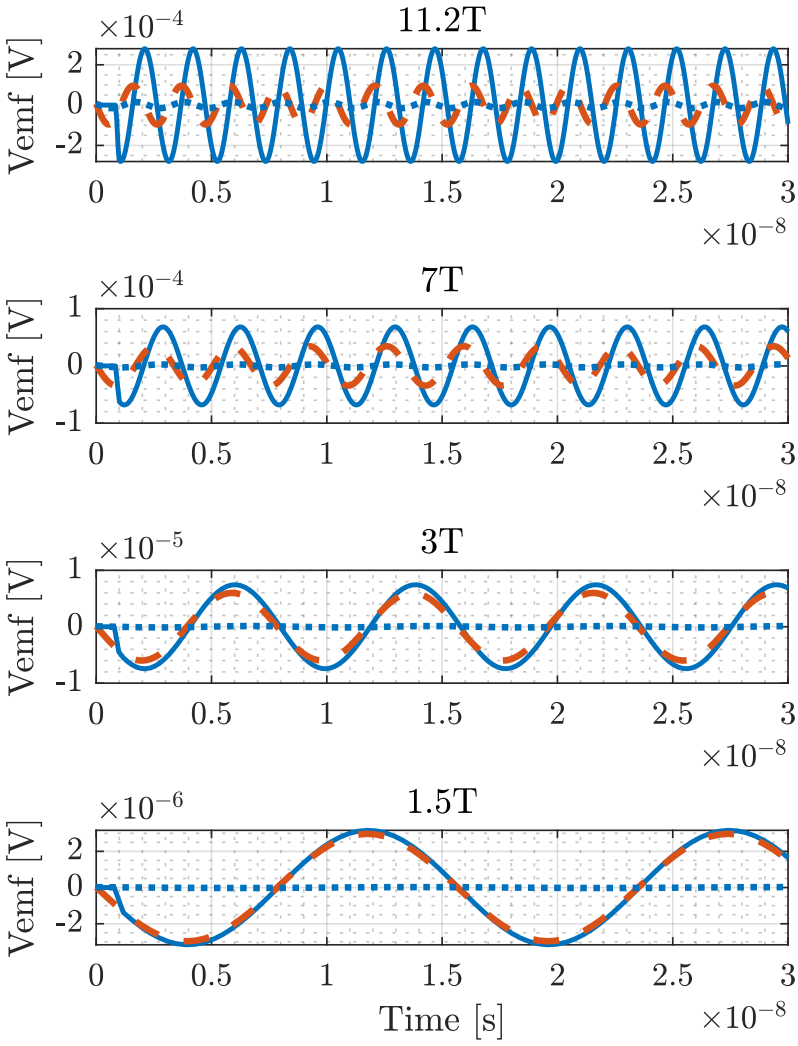

Figure 5.4: Electromotive force at Receiver 2 for various background field strengths and a ball of white matter. The dielectric parameters are listed in Table 5.1. Solid line: full wave signal model of (5.37); dashed line: quasi-static signal model of Equation (5.46); dotted line: sum of the last two terms on the right-hand side of Equation (5.46).

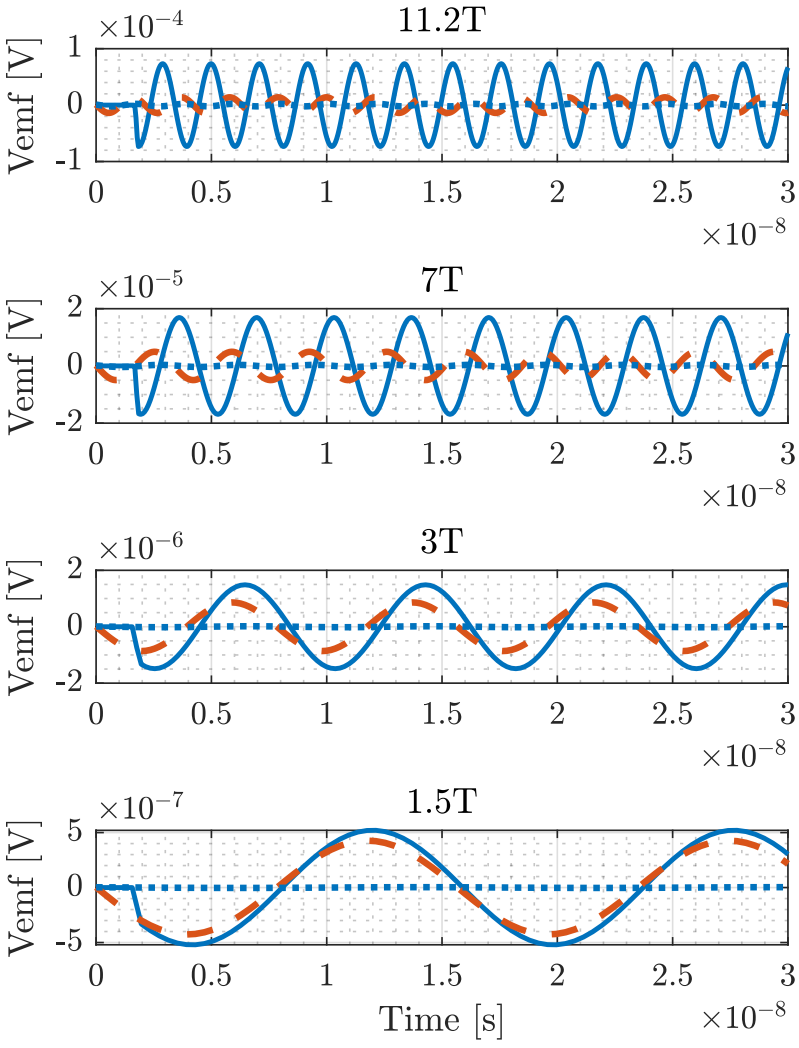

Figure 5.5: Electromotive force at Receiver 3 for various background field strengths. The dielectric parameters are listed in Table 5.1. Solid line: full wave signal model of Equation (5.37); dashed line: quasi-static signal model of Equation (5.46); dotted line: sum of the last two terms on the right-hand side of Equation (5.46).

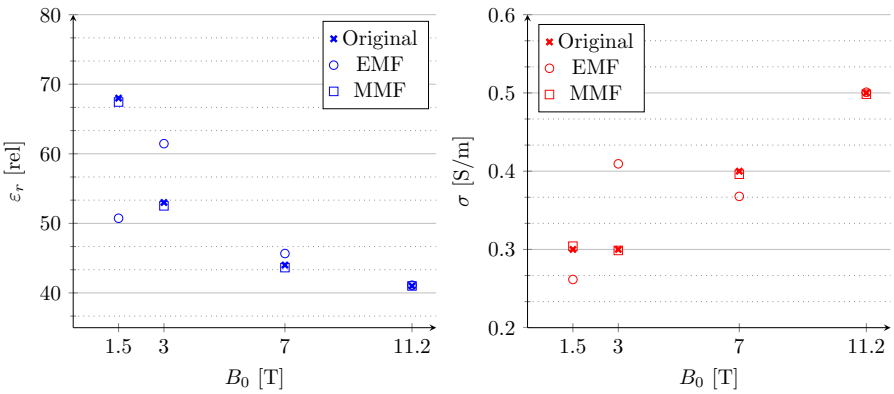

Figure 5.6: Reconstructed permittivity (left) and conductivity (right) values using an EMF or MMF measurement for various field strengths.

5

and $d_3^{\mathsf{h}}(t) = c_0^{-2}\partial_t^3 \boldsymbol{M} \cdot \boldsymbol{a}_2^{\mathsf{h}}(\boldsymbol{x}_{\mathsf{R}})$, we have

$$d_{\mathsf{h;QS}}^{\mathsf{Born}}(t) = d_1^{\mathsf{h}}(t) + \frac{\sigma}{3} d_2^{\mathsf{h}}(t) + \frac{\varepsilon_{\mathrm{r}} - 1}{3} d_3^{\mathsf{h}}(t), \tag{5.53}$$

for $t > 0$. Similarly, for the electric field signal model we have

$$d_{\mathsf{e;QS}}^{\mathsf{Born}}(t) = \frac{\sigma}{3} d_1^{\mathsf{e}}(t) + \frac{\varepsilon_{\mathrm{r}} - 1}{3} d_2^{\mathsf{e}}(t) + d_3^{\mathsf{e}}(t), \tag{5.54}$$

for $t > 0$ with $d_1^{\mathsf{e}}(t) = \partial_t \boldsymbol{M} \cdot \boldsymbol{a}_1^{\mathsf{e}}(\boldsymbol{x}_{\mathsf{R}})$, $d_2^{\mathsf{e}}(t) = \varepsilon_0 \partial_t^2 \boldsymbol{M} \cdot \boldsymbol{a}_1^{\mathsf{e}}(\boldsymbol{x}_{\mathsf{R}})$, and $d_3^{\mathsf{e}}(t) = \varepsilon_0 \partial_t^2 \boldsymbol{M} \cdot \boldsymbol{a}_2^{\mathsf{e}}(\boldsymbol{x}_{\mathsf{R}})$.

Subsequently, we introduce the time instances $t_n = (n-1)\Delta t$ for sample numbers $n = 1, 2, \ldots, N$ with $(N-1)\Delta t = T_{\mathsf{obs}}$, where T_{obs} is the length of the observation interval, and consider the above signals at these time instances to obtain

$$\boldsymbol{d}^{\mathsf{h}} = \boldsymbol{d}_1^{\mathsf{h}} + \frac{\sigma}{3} \boldsymbol{d}_2^{\mathsf{h}} + \frac{\varepsilon_{\mathrm{r}} - 1}{3} \boldsymbol{d}_3^{\mathsf{h}} \qquad \text{and} \qquad \boldsymbol{d}^{\mathsf{e}} = \frac{\sigma}{3} \boldsymbol{d}_1^{\mathsf{e}} + \frac{\varepsilon_{\mathrm{r}} - 1}{3} \boldsymbol{d}_2^{\mathsf{e}} + \boldsymbol{d}_3^{\mathsf{e}}, \tag{5.55}$$

where $\boldsymbol{d}^{\mathsf{h}} = [d_{\mathsf{h;QS}}^{\mathsf{Born}}(t_1), d_{\mathsf{h;QS}}^{\mathsf{Born}}(t_2), \ldots, d_{\mathsf{h;QS}}^{\mathsf{Born}}(t_N)]^T$ is an N-by-1 column vector and all other vectors in the above equation are defined similarly.

Since we consider FID signals as generated by the magnetisation as described by the Bloch equation of Equations (5.50) and (5.52), it immediately follows that the vectors $\boldsymbol{d}_1^{\mathsf{h}}$ and $\boldsymbol{d}_3^{\mathsf{h}}$ and the vectors $\boldsymbol{d}_2^{\mathsf{e}}$ and $\boldsymbol{d}_3^{\mathsf{e}}$ are linearly dependent. Therefore, we consider the modified (scattered) data equations

$$\tilde{\boldsymbol{d}}^{\mathsf{h}} = \boldsymbol{a}^{\mathsf{h}} \boldsymbol{c} \quad \text{and} \quad \tilde{\boldsymbol{d}}^{\mathsf{e}} = \boldsymbol{a}^{\mathsf{e}} \boldsymbol{c} \tag{5.56}$$

with $\boldsymbol{c} = \frac{1}{3}[\sigma, \varepsilon_{\mathrm{r}} - 1]^T$, $\tilde{\boldsymbol{d}}^{\mathsf{h}} = \boldsymbol{d}^{\mathsf{h}} - \boldsymbol{d}_1^{\mathsf{h}}$, $\tilde{\boldsymbol{d}}^{\mathsf{e}} = \boldsymbol{d}^{\mathsf{e}} - \boldsymbol{d}_3^{\mathsf{e}}$ and the matrices $\boldsymbol{a}^{\mathsf{h}}$ and $\boldsymbol{a}^{\mathsf{e}}$ have the column partitioning $\boldsymbol{a}^{\mathsf{h}} = (\boldsymbol{d}_2^{\mathsf{h}}, \boldsymbol{d}_3^{\mathsf{h}})$ and $\boldsymbol{a}^{\mathsf{e}} = (\boldsymbol{d}_1^{\mathsf{e}}, \boldsymbol{d}_2^{\mathsf{e}})$. Finally, noise is added to the data, and we attempt to reconstruct the medium parameters as

$$\boldsymbol{c}^* = \operatorname*{argmin}_{\boldsymbol{c}} \left\| \tilde{\boldsymbol{d}}_{\mathrm{n}}^{\mathsf{h,e}} - \boldsymbol{a}^{\mathsf{h,e}} \boldsymbol{c} \right\|_2^2 \tag{5.57}$$

where $\tilde{\boldsymbol{d}}_{\mathrm{n}}^{\mathrm{h,e}} = \tilde{\boldsymbol{d}}^{\mathrm{h,e}} + \boldsymbol{n}$ is the noisy data vector with $\boldsymbol{n}$ the noise vector. With $T_0 = 2\pi/\omega_0$, we first take $T_{\mathrm{obs}} = 3T_0 \approx [10^{-9}, 10^{-8}]$ s in our minimization problem. Clearly, the exponential decay of the FID signal can be neglected in this case. With an SNR of 20 dB the conductivity and permittivity are determined by solving the corresponding least-squares problem Equation (5.57) and the retrieved parameters are depicted in Figure 5.6 along with the exact conductivity and permittivity values of white matter and for various background fields as listed in Table 5.1. From this figure, we observe that for a magnetic field (emf) measurement, the error in the retrieved medium parameters decreases as the background field strength increases. At 1.5 T and 3 T, the medium parameters cannot be retrieved, but accurate medium parameters are obtained only at 11.2 T. Since the dielectric medium parameters contribute via the near field to a signal that is based on an electric field (mmf) measurement, we expect that these parameters can be reliably recovered for low and high background fields. From Figure 5.6 we observe that this is indeed the case and similar to a magnetic field measurement, the reconstruction results improve as the strength of the background field increases. Finally, we mention that we have repeated this experiment on an observation interval $T_{\mathrm{obs}} = 3T_2 \approx 10^{-2}$ s and found similar results, showing that the electrical properties can also be recovered on a $\sim 10^{-2}$ time scale.

5.4. Discussion and Conclusions

In this paper, we have presented full wave-signal models for MRI field measurements. The models show that the magnetization and the induced electric scattering currents contribute to the measured signals, both weighted by their respective receive fields that are determined by the antenna that is used for reception. We have shown that to evaluate the models, the Green's tensors of the background medium must be known, along with the dielectric properties of the object and the magnetization within the excited part of the object must be known as well. For inhomogeneous background media, the Green's tensors can only be evaluated numerically in general, which may be a formidable task especially if electrically large objects are of interest. Moreover, for given dielectric medium profiles and a given magnetization, the electric field strength within the object must be computed, since it is required to determine the electric scattering source. In other words, apart from numerically computing the Green's tensors of the background medium, a forward problem for the electric field strength must be solved as well. Despite these computational bottlenecks, direct evaluation is possible in principle. Moreover, the models can be easily extended to include contrasts in permeability, but at the expense of having to solve a coupled forward problem for the electric and magnetic field within the object of interest.

We would like to emphasise that the model is the first (to our knowledge) to explicitly take the contribution of scattering from dielectric tissue into account for the signal model in MRI. The fact that fields are not quasi-static anymore for high frequency MR is well understood and has been used to develop new antenna design concepts such as dipole and loop antenna combinations. However, these novel antenna design concepts only take the non-scattering signal contribution into account (described here through the background electric field) as opposed to our comprehensive signal

model. This model should therefore be more accurate when considering complex effects such as local SAR, and can potentially be used to improve antenna design for electrical properties imaging specifically.

To obtain explicit closed-form signal representations for electric and magnetic field measurements, we have considered a homogeneous ball that is embedded in free-space. Obviously, the Green's tensors of the background medium are now known and if the dielectric parameters and radius of the ball are "sufficiently small", the quasi-static Born approximation applies meaning that the electric field within the ball may be approximated by the quasi-static background field, which is explicitly known. Obviously, there is now no need to solve a forward problem and the medium parameters show up explicitly in the resulting signal models. Travel time effects are still included in these models, since the quasi-static Born approximation applies to the electric field within the ball only. Quasi-static signal models may be obtained, however, for receiver locations for which travel time effects can be neglected. These signal models directly generalise the standard quasi-static models as normally used in MRI and clearly show how the dielectric parameters of the ball influence the measured signals. In fact, for FID signals obtained from an electric or magnetic field measurement, we demonstrated that the dependence of the signals on the medium parameters can even be used to retrieve these parameters. Specifically, we showed that for high background fields (7 T and 11.2 T), electric (mmf) and magnetic (emf) field measurements allow for reliable parameter reconstructions, while at lower field strengths only electric field measurements can be used essentially because the dielectric parameters show up in the near-field of an electric field measurement and not in the near-field of a magnetic field measurement.

Future work consists of experimental validation of the full-wave and simplified quasi-static signal models, and its derived reconstruction method. The simplified quasi-static models have their limitations, of course, and care should be taken when applying these models, since they are valid for a ball and under very special circumstances only (quasi-static field and Born approximation applies). However, the simplified models can be used to find the dielectric parameters of various tissue types and other materials using easily obtained FID signals or using other MRI signal acquisition schemes. Also, combining the above formulation with a robust framework for SNR optimisation and the ultimate intrinsic snr definition are interesting avenues for future research.

Obviously, the full-wave models do not suffer from these limitations and allow us to determine how inhomogeneous dielectric tissue profiles influence the measured signals. Large-scale computations are required to determine the effects of the conductivity and permittivity profiles on the measured signals, but the models can potentially be used in a wide variety of applications ranging from for RF coil/antenna optimalisation to reduce local SAR and optimize the SNR in specific imaging applications to the design of antenna arrays that maximize the sensitivity of the signals to the electrical properties as opposed to the magnetisation.

References

[1] D.I Hoult and Paul C Lauterbur. The sensitivity of the zeugmatographic experiment involving human samples. *Journal of Magnetic Resonance (1969)*, 34(2):425 – 433, 1979.

[2] H D W Hill and R E Richards. Limits of measurement in magnetic resonance. *Journal of Physics E: Scientific Instruments*, 1(10):977–983, oct 1968.

[3] P A Bottomley and E R Andrew. RF magnetic field penetration, phase shift and power dissipation in biological tissue: implications for NMR imaging. *Physics in Medicine and Biology*, 23(4):630–643, jul 1978.

[4] Riccardo Lattanzi and Daniel K. Sodickson. Ideal current patterns yielding optimal signal-to-noise ratio and specific absorption rate in magnetic resonance imaging: computational methods and physical insights. *Magnetic resonance in medicine*, 68(1):286–304, Jul 2012. 22127735[pmid].

[5] Boris Keil and Lawrence L. Wald. Massively parallel MRI detector arrays. *Journal of Magnetic Resonance*, 229:75 – 89, 2013. Frontiers of In Vivo and Materials MRI Research.

[6] A. J. E. Raaijmakers, P. R. Luijten, and C. A. T. van den Berg. Dipole antennas for ultrahigh-field body imaging: a comparison with loop coils. *NMR in Biomedicine*, 29(9):1122–1130, 2016.

[7] M. Arcan Ertürk, Alexander J.E. Raaijmakers, Gregor Adriany, Kâmil Uğurbil, and Gregory J. Metzger. A 16-channel combined loop-dipole transceiver array for 7 Tesla body MRI. *Magnetic Resonance in Medicine*, 77(2):884–894, 2017.

[8] Riccardo Lattanzi, Graham C. Wiggins, Bei Zhang, Qi Duan, Ryan Brown, and Daniel K. Sodickson. Approaching ultimate intrinsic signal-to-noise ratio with loop and dipole antennas. *Magnetic Resonance in Medicine*, 79(3):1789–1803, 2018.

[9] Alexander J.E. Raaijmakers, Michel Italiaander, Ingmar J. Voogt, Peter R. Luijten, Johannes M. Hoogduin, Dennis W.J. Klomp, and Cornelis A.T. van den Berg. The fractionated dipole antenna: A new antenna for body imaging at 7 Tesla. *Magnetic Resonance in Medicine*, 75(3):1366–1374, 2016.

[10] Ogan Ocali and Ergin Atalar. Ultimate intrinsic signal-to-noise ratio in MRI. *Magnetic Resonance in Medicine*, 39(3):462–473, 1998.

[11] Michael A. Ohliger, Aaron K. Grant, and Daniel K. Sodickson. Ultimate intrinsic signal-to-noise ratio for parallel MRI: Electromagnetic field considerations. *Magnetic Resonance in Medicine*, 50(5):1018–1030, 2003.

[12] E. Kopanoglu, V. B. Erturk, and E. Atalar. Analytic expressions for the ultimate intrinsic signal-to-noise ratio and ultimate intrinsic specific absorption rate in MRI. *Magnetic Resonance in Medicine*, 66(3):846–858, 2011.

[13] Wyger M. Brink and Andrew G. Webb. High permittivity pads reduce specific absorption rate, improve B1 homogeneity, and increase contrast-to-noise ratio for functional cardiac MRI at 3 T. *Magnetic Resonance in Medicine*, 71(4):1632–1640, 2014.

[14] Adrianus T de Hoop. *Handbook of Radiation and Scattering of Waves*. Academic Press, 1995.

[15] Adrianus T. de Hoop. Convergence criterion for the time-domain iterative Born approximation to scattering by an inhomogeneous, dispersive object. *J. Opt. Soc. Am. A*, 8(8):1256–1260, Aug 1991.

[16] Weng Cho Chew. *Waves and fields in inhomogeneous media*. IEEE press, 1995.

[17] Jorge Zavala Bojorquez, Stéphanie Bricq, Clement Acquitter, François Brunotte, Paul M. Walker, and Alain Lalande. What are normal relaxation times of tissues at 3 T? *Magnetic Resonance Imaging*, 35:69 – 80, 2017.

[18] Institute for Applied Physics "Nello Carrara" Florence (Italy). Calculation of the dielectric properties of body tissues in the frequency range 10 Hz - 100 GHz. http://niremf.ifac.cnr.it/tissprop/htmlclie/htmlclie.php, 2020. visited february 2020.

[19] Sami Gabriel, RW Lau, and Camelia Gabriel. The dielectric properties of biological tissues: Ii. measurements in the frequency range 10 Hz to 20 GHz. *Physics in medicine & biology*, 41(11):2251, 1996.

6

Proximal Gradient Machine Learning Approach to Quantitative Susceptibility Mapping

Patrick Fuchs
Ruud van Sloun

ABSTRACT– *Quantitative susceptibility mapping (QSM) is a specific type of magnetic resonance imaging (MRI), used to image the magnetic susceptibility or magnetic permeability of tissue. This imaging method requires the inversion of a dipole convolution. We describe a new method to perform this inversion using a data-driven neural proximal gradient algorithm. The method combines a known physics model with machine learning tools for regularisation. This way of regularisation may help in recovering information that is lost in a structured way through the forward model operation. Our results show good agreement with model-based methods and provide a very robust, efficient and flexible way to perform the dipole deconvolution.*

6.1. Introduction

In quantitative susceptibility mapping (QSM) the goal is to reconstruct the magnetic susceptibility from magnetic resonance imaging (MRI) data. This is done using the phase shift in the measured signal due to variations in the magnetic field. These phase perturbations in turn can be related to changes in the susceptibility of the object (with respect to a background (free-space) susceptibility) [1, 2].

Change in susceptibility is predominantly caused by metals in tissue, for example iron and calcium, which can be manifestations of various pathological processes or diseases. Important examples of these are neuro-degenerative diseases like early onset dementia or Alzheimer's, haemorrhages or pathological calcification. Therefore QSM can play an important role in diagnosing and researching these diseases. Since the pathologies of interest are often small with respect to the field of view and their contribution to the measured signal is naturally smoothed over the image through their point spread function, it is imperative to have reconstruction methods that can counteract this and pinpoint the sources accurately.

Other challenges for QSM are the removal of a substantial unwanted background signal, and, since the signal of interest is a phase quantity, robust phase unwrapping. Phase unwrapping is a problem encountered in many disciplines with a number of excellent algorithms developed for it, i.e. Laplacian based, region growing, best path or graph-cut [3–5]. For the background removal also a number of great tools have been developed [6–10]. In this research we consider the last step of each QSM algorithm, the dipole inversion. This step can be easily isolated and is well described using an anlytical forward model.

There are currently a number of dipole inversion algorithms, from the straightforward direct (thresholded) deconvolution [11], to least squares based methods [12, 13], and even deep neural network based methods [14, 15]. Typically the least squares based methods require tuning of a (regularisation) parameter and have a high computational cost. The neural network based methods on the other hand are more efficient (after having been trained) but require large amount of training time and data. In terms of training data it was shown that synthetic data can be leveraged for standard convolutional encoder-decoder networks [14]. Yet, robustness to distribution shift is hard to warrant and these black-box networks can be hard to analyze.

In this chapter we describe an approach where we try to combine the flexibility of a learned network with the robustness of our analytical model. We present a learned unrolled iterative proximal gradient scheme, which allows us to learn the regularisation of our least squares problem through the use of a proximal mapping based on the QSM data. We also attempt to gain insight into the "best" trained regularisation method for this dipole inversion problem.

This approach is similar to [15, 16], which use a variational network relying on subgradient methods, whereas in this work we use proximal gradient operators. Proximal gradient operators theoretically have a better convergence, and have shown very good results in other areas such as ultrasound imaging [17]. Additionally, Polak and Hammernik use magnitude weighting in their work to further simplify the inversion problem, which we do not consider in this study.

6.2. Theory

6.2.1. Signal Model

We specifically consider *single orientation* reconstruction of the tissue susceptibility. In this, we follow the framework of the 2016 reconstruction challenge [18], and use susceptibility tensor imaging (STI) [19] as our reference model. According to the STI signal formulation, the phase in the Fourier domain can be described as

$$\tilde{\phi}(\boldsymbol{k}) = \frac{1}{3}\tilde{\boldsymbol{H}}^T(\boldsymbol{k}) \cdot \underline{\tilde{\chi}}(\boldsymbol{k}) \cdot \tilde{\boldsymbol{H}}(\boldsymbol{k}) - \tilde{\boldsymbol{H}}(\boldsymbol{k}) \cdot \boldsymbol{k} \frac{\boldsymbol{k}^T \cdot \underline{\tilde{\chi}}(\boldsymbol{k}) \cdot \tilde{\boldsymbol{H}}(\boldsymbol{k})}{\|\boldsymbol{k}\|^2}, \tag{6.1}$$

where all quantities with a tilde are in the Fourier domain, $\underline{\tilde{\chi}}(\boldsymbol{k})$ is the susceptibility tensor (3×3), $\tilde{\boldsymbol{H}}(\boldsymbol{k}) = [\tilde{H}_x(\boldsymbol{k}), \tilde{H}_y(\boldsymbol{k}), \tilde{H}_z(\boldsymbol{k})]^T$ is the magnetic field, and $\boldsymbol{k} = [k_x, k_y, k_z]^T$ collects the spatial Fourier coordinates. We will assume that the measurement is performed in the transverse plane with respect to our data orientation, so $\tilde{\boldsymbol{H}} = [0, 0, 1]^T$, and the signal equation simplifies to

$$\tilde{\phi}(\boldsymbol{k}) = \left(\frac{1}{3} - \frac{k_z^2}{\|\boldsymbol{k}\|^2}\right)\tilde{\chi}_{33} - \frac{k_z}{\|\boldsymbol{k}\|^2}\left(k_x\tilde{\chi}_{13} + k_y\tilde{\chi}_{23}\right). \tag{6.2}$$

And, as often is assumed in single orientation QSM, the off diagonal tensor elements $\tilde{\chi}_{13}$ and $\tilde{\chi}_{23}$ are assumed negligible, so we are left with

$$\tilde{\phi}(\boldsymbol{k}) = \left(\frac{1}{3} - \frac{k_z^2}{\|\boldsymbol{k}\|^2}\right)\tilde{\chi}_{33}(\boldsymbol{k}) = \tilde{D}(\boldsymbol{k})\tilde{\chi}(\boldsymbol{k}), \tag{6.3}$$

with $\tilde{D}(\boldsymbol{k}) = \left(\frac{1}{3} - \frac{k_z^2}{\|\boldsymbol{k}\|^2}\right)$ as our dipole kernel, and we have used $\tilde{\chi}$ to denote the $\tilde{\chi}_{33}$ element. This translates to a dipole convolution in the spatial domain, which is commonly implemented using Fourier transformations as

$$\phi(\boldsymbol{x}) = \mathcal{F}^{-1}\left\{\tilde{D}(\boldsymbol{k})\mathcal{F}\left\{\chi(\boldsymbol{x})\right\}\right\}, \tag{6.4}$$

where $\mathcal{F}\{\cdot\}$ is the forward and $\mathcal{F}^{-1}\{\cdot\}$ the inverse Fourier transform, and $\chi(\boldsymbol{x})$ the susceptibility.

Discretised problem

We discretise Equation (6.4) to solve the inverse problem numerically. In short, the discretised problem is given by

$$\boldsymbol{\phi} = \mathsf{F}^H\mathsf{D}\mathsf{F}\boldsymbol{\chi}. \tag{6.5}$$

Here the susceptibilities and measured phase are given in x-lexicographic ordering as

$$\boldsymbol{\phi} = [\phi(\boldsymbol{x}_1), \phi(\boldsymbol{x}_2), \phi(\boldsymbol{x}_3), \ldots]^T, \text{ and}$$
$$\boldsymbol{\chi} = [\chi(\boldsymbol{x}_1), \chi(\boldsymbol{x}_2), \chi(\boldsymbol{x}_3), \ldots]^T,$$

with $\boldsymbol{x}_i$ the spatial coordinates. To approximate the dipole kernel in a discretized space, the model of [20] will be used, which is given by

$$\tilde{D}(\boldsymbol{k}) = \frac{1}{3} - \frac{1 - c(k_x)}{3 - c(k_x) - c(k_y) - c(k_z)}, \tag{6.6}$$

with

$$c(k_i) = \cos\left(\frac{2\pi k_i}{N_i}\right) \quad \text{for } i = x, y, z. \tag{6.7}$$

Our dipole matrix then becomes a diagonal matrix

$$\mathsf{D} = \text{diag}\left[\tilde{D}(\boldsymbol{k}^1), \tilde{D}(\boldsymbol{k}^2), \tilde{D}(\boldsymbol{k}^3), \ldots\right], \tag{6.8}$$

where $\boldsymbol{k}^i$ are the x-lexicographic ordened Fourier space coefficients (more specifically $\boldsymbol{k}^i = [k_x^i, k_y^i, k_z^i]$). Lastly, the Fourier transformations are given here in the form of discrete Fourier transformation (DFT) matrices (as F and F^H for the forward and inverse transformations respectively).

6.2.2. Learning Framework

To design our deep network, we build on the above QSM signal model given in Equation (6.5), and structure its architecture to solve the folowing regularised least squares problem:

$$\hat{\boldsymbol{\chi}} = \min_{\boldsymbol{\chi}} \left[\left\|\mathsf{F}^H\mathsf{D}\mathsf{F}\boldsymbol{\chi} - \boldsymbol{\phi}\right\|_2 + \lambda R(\boldsymbol{\chi})\right], \tag{6.9}$$

in which $R(\boldsymbol{\chi})$ denotes a regularizer. Examples of such regularizers are the ℓ_1 and ℓ_2 norms of the solution, or total variation penalties, which are used throughout the QSM literature. Appropriate selection of the regularizer dictates the fidelity of the recovered estimate $\hat{\boldsymbol{\chi}}$, and is a challenge on its own.

Drawing inspiration from iterative proximal-gradient schemes [21], which are dedicated to solve (6.9), we unfold L such iterations, learning an adequate image-domain proximal mapping $\mathcal{P}_\theta^{(l)}$ and step size $\alpha^{(l)}$ at each fold:

$$\hat{\boldsymbol{\chi}}^{(l+1)} = \mathcal{P}_\theta^{(l)}\left[\hat{\boldsymbol{\chi}}^{(l)} - \alpha^{(l)}\mathsf{F}^H\mathsf{D}\left(\mathsf{D}\mathsf{F}\hat{\boldsymbol{\chi}}^{(l)} - \mathsf{F}\boldsymbol{\phi}\right)\right]. \tag{6.10}$$

In the above formulation, at each fold a gradient step is taken towards the sampling-consistent subspace that adequately represents the physical measurement of $\boldsymbol{\chi}$. The trained proximal operator $\mathcal{P}_\theta^{(l)}$, a convolutional network on which we detail in Section 6.3.1, then projects this onto the manifold of visually plausible images [22], removing noise and blurring artifacts. One single fold of this iterative scheme can be found in Figure 6.1, and an example unrolling can be found in Figure 6.2.

6.3. Methods

There are two ways to approach this problem, one is in the spatial domain (as described in the theory above) and another would be in the frequency domain, solving the following problem

$$\tilde{\boldsymbol{\phi}} = \mathsf{D}\tilde{\boldsymbol{\chi}}. \tag{6.11}$$

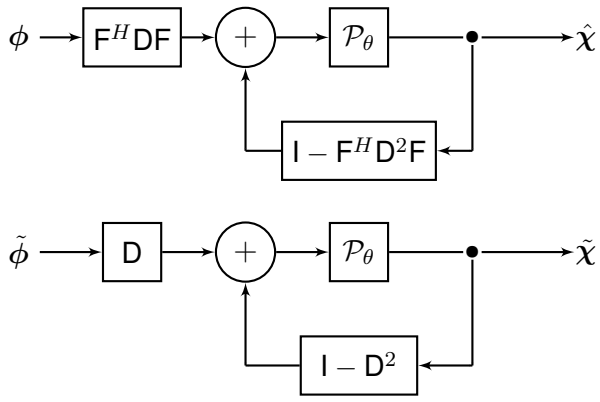

Figure 6.1: A schematic representation of the iterative scheme of (6.10) (top) and (6.12) (bottom). Each unfolding adds an extra loop to the network in this sense.

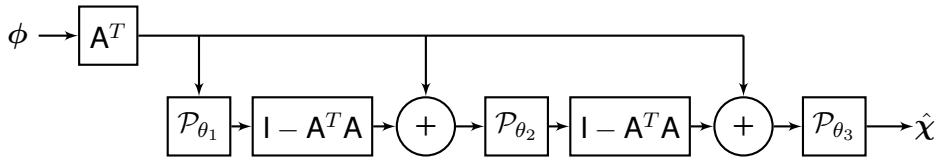

Figure 6.2: An unrolled version representing three iterations of the update schemes.

This gives rise to the following update scheme (following the notation from Equation (6.10))

$$\tilde{\chi}^{(l+1)} = \mathcal{P}_\theta^{(l)} \left[\tilde{\chi}^{(l)} - \alpha^{(l)} D \left(D\tilde{\chi}^{(l)} - \tilde{\phi} \right) \right]. \tag{6.12}$$

A single fold of this update scheme can also be found in Figure 6.1.

In a fully sampled noiseless scenario these would essentially be solving the same problem, however in the machine learning framework it can still lead to differences in convergence and end result. We will therefore compare both approaches and their differences.

6.3.1. Network Topology

The machine learning network is characterised by the number of unfoldings (comparable to the number of iterations of the iterative shrinkage- thresholding algorithm (ISTA)) and the structure of the proximal mapping network (learned at each different fold).

The proximal mapping is an elementwise soft thresholding in a learned (convolutional) dictionary. In this learning framework the soft thresholding parameter is learnable. Also, a convolutional network is applied before and after the proximal mapping to create a learnable “dictionary” mapping allowing the regularisation to be applied across spatial (or frequency) dimensions. This network topology will be identical for each unfolding, however the (learned) weights are separately determined, essentially allowing each layer to learn its own dictionary of local relationships. The kernel for

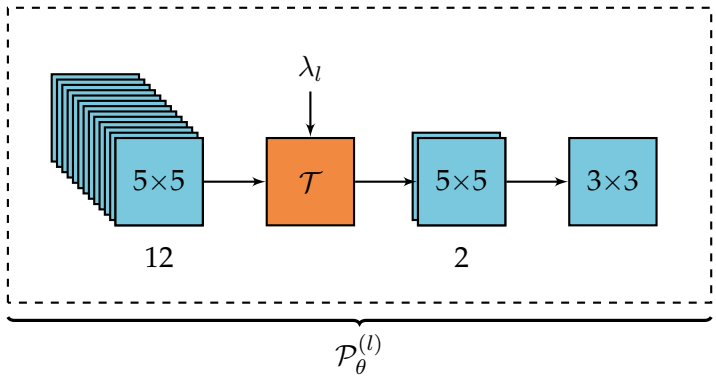

Figure 6.3: Block diagram of the proximal mapping operator, light blue are the convolutional layers and orange denotes the soft thresholding operation ($\mathcal{T}$). The final convolutional mapping is used to map the result to the image space (back to a single layer).

the convolutions is set to 5×5 pixels to allow the dictionaries to capture the local relationships. And the filter depth of the dictionary prior to the proximal mapping is 12, with a filter depth of 2 after the proximal mapping. After these dictionaries a convolutional mapping with kernel size 3×3 (and filter depth 1) is used to map the result back into measurement space. A graphical representation of this can be found in Figure 6.3

These convolutional layers use a "relu" activation, and are followed by a mapping back to the measurement space (for filter depths larger than the input dimensionality). Lastly, an "adam" optimiser is used to learn the network parameters with a learning rate of 0.001, and the Fourier transformations are implemented through the fast Fourier transformation (FFT) in the algorithm. For the frequency domain implementation the real and imaginary parts of input and output are stacked and the same filter banks applied to both. In both cases this leads to a network with almost 19 000 weights.

6.3.2. Training and validation Data

For training the model synthetic datasets are used. The synthetic data is generated similar to the data used in the the DeepQSM method [14]. However, in our simulations we have used rectangels instead of squares, also allowing for rectangular boxes, and we decreased the number of objects used to between 2 and 12 objects ($[1, \ldots, 6]$ circles and $[1, \ldots, 6]$ rectangles both drawn from a uniform distribution). An example of one of these can be found in Figure 6.4. In total we use 500 datasets for training. These are split into 450 training and 50 test datasets at each training epoch during the training process, so that all datasets are used in both training and testing during this time.

To validate the method we use a brain image from the fast algorithm for nonlinear susceptibility inversion (FANSI) toolbox[1], as well as a synthetic phantom consisting

[1] https://gitlab.com/cmilovic/FANSI-toolbox

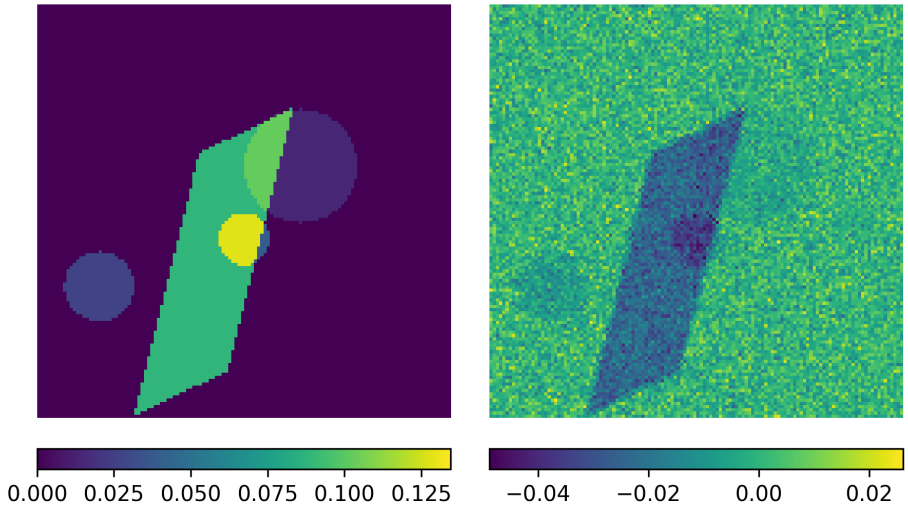

Figure 6.4: Randomly generated synthetic training dataset. Left is the susceptibility (unitless) and right the computed phase image (measurement, in radians).

of eight spheres of varying susceptibility. Lastly, all data sets were re-sampled at a resolution of 2.5×2.5 mm from 0.9375×0.9375 mm and a matrix size of 128×128 pixels from 256×256 pixels (including zero padding the domain to get the required field of view).

6.3.3. Experiment description

The network was trained on noisy phase measurements. For the noise complex Gaussian distributed noise at a signal to noise ratio (SNR) of 30 dB was added to the measurements. Important to note is that it was not added directly to the phase information but rather to the actual measurement from which the phase is extracted as,

$$\phi = 2 \arctan\left(\frac{\mathrm{Im}(\mathrm{meas} + \mathrm{noise})}{\mathrm{Re}(\mathrm{meas} + \mathrm{noise})}\right).$$

The noise level is chosen to still allow the use of truncated (or thresholded) k-space division, in which the measured phase is directly (pointwise) divided by the dipole kernel. This method directly increases the influence of noise for small values of the dipole kernel, and would require low pass filtering of the measured phase in low SNR situations.

Furthermore the experiment consisted of 100 epochs of training after which the predictions were taken, with an early stopping criterion based on the validation loss to stop after 4 epochs without decreasing loss. This stopping criterion stopped the training after 78 epochs for the image domain based network and 93 epochs for the frequency domain based one. The predictions are then compared to the ground truth, a thresholded k-space division (TKD) reconstruction [11], and a reference least

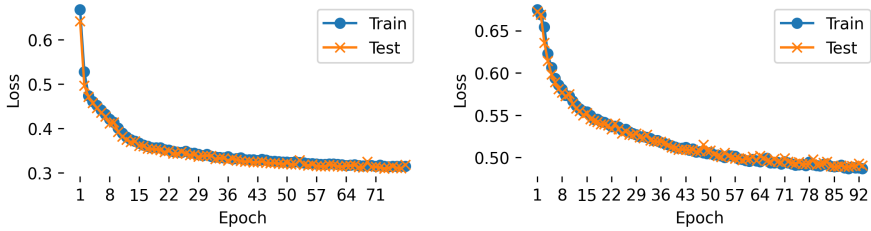

Figure 6.5: Training loss and validation loss of the image domain approach (left) and frequency domain approach (right).

squares (LSQR) and ISTA reconstruction. The thresholding of the TKD method was set at 0.1, which showed the best result from a range of thresholds at the given SNR. The ISTA reconstruction consisted of 100 iterations with alpha of 0.5, again found through trial and error.

6.4. Results

The resulting reconstructions can be found in Figures 6.6 and 6.7. For the first image, the spherical phantom, at the given SNR, both regular ISTA and LSQR reconstructions perform relatively well. Most clearly the noise can be seen as abberations in the reconstructed susceptibility. This can be improved slightly by smoothing the input data using a Gaussian filter or regularising the LSQR reconstruction by decreasing the nubmer of iterations. Both of these approaches will however also smooth the edges of the reconstruction. One important thing to note is that the LSQR approach seems to overestimate the susceptibility slightly (as can be seen specifically in the three highest susceptibility spheres of the spherical phantom). Also, all three reference reconstructions struggle with reconstructing the lowest susceptibility value (bottom right sphere).

Both learned proximal mapping approaches are better at filtering the background noise and also reconstructing the homogenous spheres without aberrations. The image domain reconstructions seems to be better at reducing background noise but also struggles with the lowest susceptibility sphere, whereas the frequency domain implementation is the only one to reconstruct this sphere in the most pronounced manner.

In terms of learning rate and convergence the networks performed relatively similar, with the image domain network having a slightly faster initial convergence and also ending up with a lower validation loss than the frequency domain network. The learning curves of both networks can be found in Figure 6.5.

In the anatomical reconstruction, which can be seen in Figure 6.7 the difference between image and frequency domain implementations becomes more apparent as a distinct smearing can be observed in the image domain implementation. The frequency domain implementation also has slight blurring but better resolves small anatomical details while also succesfully suppressing noise effects.

Both machine learned approaches are much faster than the LSQR implementation

Method	Recon. time		Normalised MSE
TKD	3.24	ms	83.58
LSQR	61	s	48.74
ISTA	117	ms	43.18
Prox-Image space	45.2	ms	21.83
Prox-Freq space	49.1	ms	13.68

Table 6.1: Comparison of reconstruction times and normalised mean squared errors of all different methods on the spheres contrast. The reconstruction times have been computed over 10 repetitions on a Google Colab sheet with GPU support. Note that the LSQR and ISTA reconstruction times are dependent on the convergence rate for the given dataset (noisy data often results in more iterations which leads to longer reconstruction times) whereas for the other methods the number of iterations is fixed and thus the reconstruction times as well.

and match the speed of the ISTA implementation. Simple TKD is still faster, but the reconstruction speed is less than a second with all but the LSQR method (which takes upwards of a minute to reconstruct a (noisy) 2 dimensional slice). A comparison of normalised mean square errors and reconstruction times of all 5 algorithms can be found in Table 6.1 for a more in depth look.

6.5. Conclusions

A novel learned proximal gradient method was applied to the QSM dipole inversion problem. With this approach a network with a very small number of weights can be used to solve an inverse problem very efficiently. Conventional convolutional neural networks such as used in e.g. DeepQSM [14] require millions of weights to be trained and often rely on large training datasets to find these weights. The proposed method on the other hand relies on less than 19 000 weights.

The decrease in network complexity is made possible foremost because of the forward model, which is incorporated directly within the machine learning network. This means only the regularisation needs to be learned, which we do through a proximal gradient method here. This proximal gradient operation is more efficient than a sub-gradient approach as for example presented in [15] (variational networks dipole inversion (VaNDI)).

The proximal mapping gives us less control over the regularisation, but compared to conventional gradient based methods like the streaking artefact reduction (STAR) method [13] we offload finding a good tuning value for the regularisation parameters to the training phase which makes our method “parameter free” afterwards during reconstruction or regular imaging use. Also, the dictionary based proximal mapping allows us to learn how to deal with the zeroes in the dipole convolution, which lead to the non-invertibility of the operation. The smoothing is most likely related to the cost function, as an improvement of the image based model is observed when switching to a Fourier domain cost function to compare to the Fourier model based method. Additionally a generative adversarial network (GAN) cost could be used for example to promote edges or sharpness of the reconstruction.

(a) Original contrast

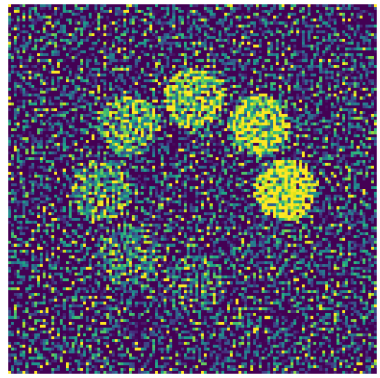

(b) TKD reconstruction

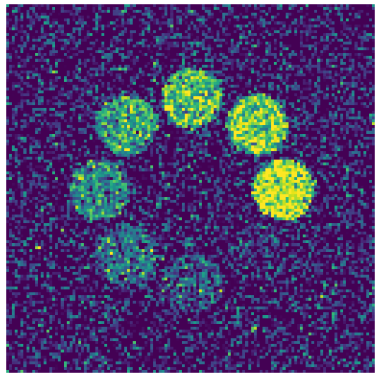

(c) ISTA reconstruction

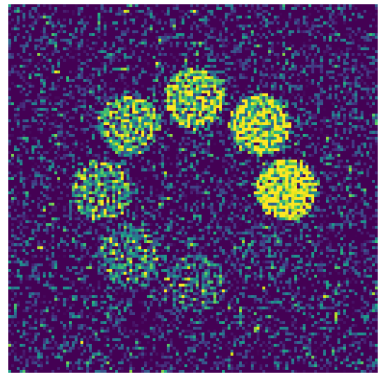

(d) LSQR reconstruction

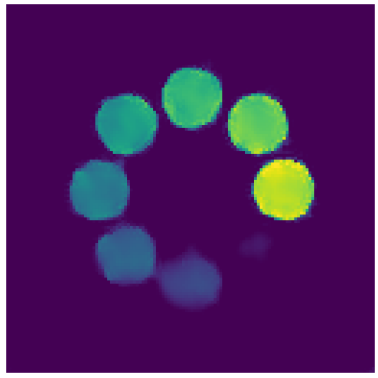

(e) ProxQSM reconstruction
(Image domain)

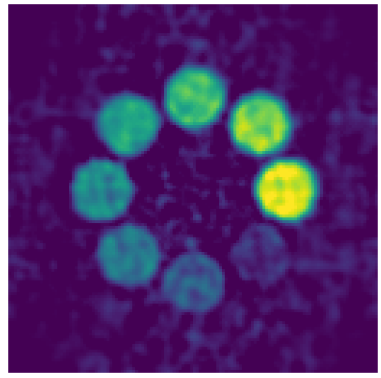

(f) ProxQSM reconstruction
(Frequency domain)

Figure 6.6: Normalised original susceptibility distributions and reconstructions of spherical phantom.

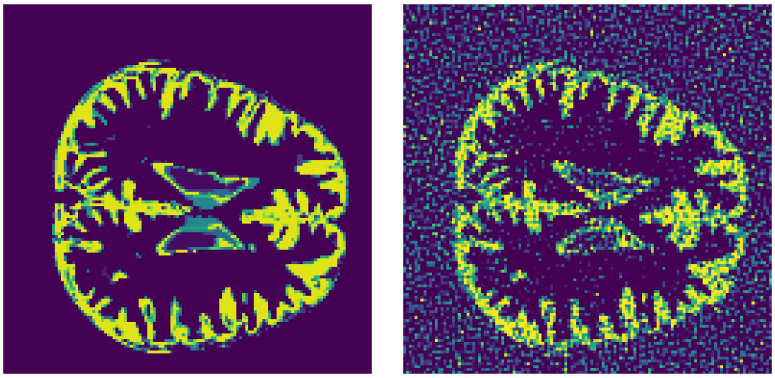

(a) Original contrast

(b) TKD reconstruction

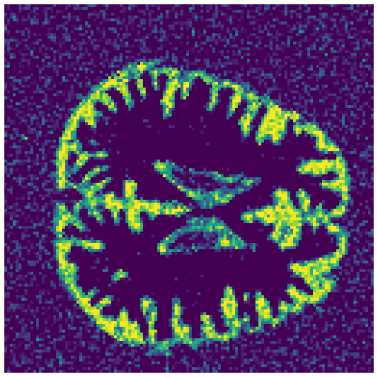

(c) ISTA reconstruction

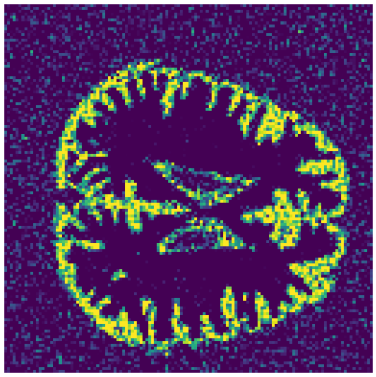

(d) LSQR reconstruction

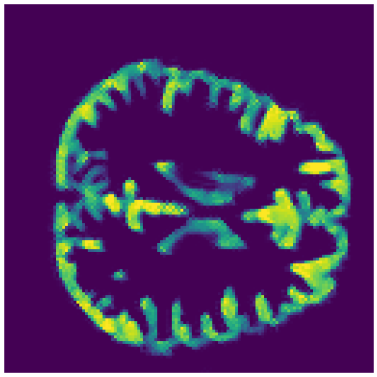

(e) ProxQSM reconstruction
(Image domain)

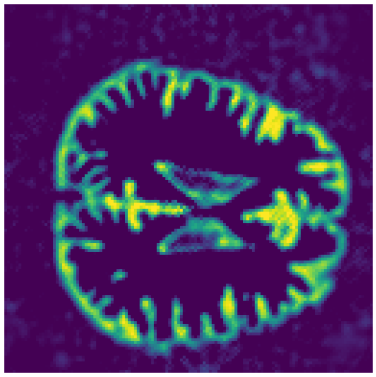

(f) ProxQSM reconstruction
(Frequency domain)

Figure 6.7: Normalised original susceptibility distributions and reconstructions of anatomical dataset.

Future work includes investigating an inversion based on the actual measured signal (amplitude and phase) to see if this can provide additional information (regarding the spatial position of the object) as well as noise robustness. The role of the (colored) noise on the convergence of our training, as well as on the reference reconstructions will also be compared to other more elaborate (accurate) forward simulation approaches for QSM to verify whether the forward model used is an accurate representation of these signals. A more accurate forward model should lead to faster learning of the network, and better reference datasets will be necessary to apply this method to real measured data.

In future work we will look at whether the trained proximal mapping can generalise across different spatial discretisations, i.e. whether training the proximal mapping on a very fine grid will still allow us to use it on a more coarse measurement of the phase (given the right dipole kernel for that gridding of course).

Finally, our method is faster from a computational point of view when compared to conventional iterative methods (after being trained), as the reconstruction essentially becomes a forward operation of the network. Future work will include expanding the method to multiple angle measurements and comparing it to the gold standard calculation of susceptibility through multiple orientation sampling (COSMOS) reconstructions [23], as well as looking at amplitude weighting of the inverse problem, i.e. changing from the phase formulation to the full measured signal.

References

[1] Rares Salomir, Baudouin Denis de Senneville, and Chrit TW Moonen. A fast calculation method for magnetic field inhomogeneity due to an arbitrary distribution of bulk susceptibility. *Concepts in Magnetic Resonance Part B: Magnetic Resonance Engineering*, 19B(1):26–34, 2003.

[2] J.P. Marques and R. Bowtell. Application of a fourier-based method for rapid calculation of field inhomogeneity due to spatial variation of magnetic susceptibility. *Concepts in Magnetic Resonance Part B: Magnetic Resonance Engineering*, 25B(1):65–78, 2005.

[3] Wei Li, Bing Wu, and Chunlei Liu. Quantitative susceptibility mapping of human brain reflects spatial variation in tissue composition. *NeuroImage*, 55(4):1645 – 1656, 2011.

[4] Hussein S. Abdul-Rahman, Munther A. Gdeisat, David R. Burton, Michael J. Lalor, Francis Lilley, and Christopher J. Moore. Fast and robust three-dimensional best path phase unwrapping algorithm. *Appl. Opt.*, 46(26):6623–6635, Sep 2007.

[5] J. Dong, T. Liu, F. Chen, D. Zhou, A. Dimov, A. Raj, Q. Cheng, P. Spincemaille, and Y. Wang. Simultaneous phase unwrapping and removal of chemical shift (SPURS) using graph cuts: Application in quantitative susceptibility mapping. *IEEE Transactions on Medical Imaging*, 34(2):531–540, 2015.

[6] Wei Li, Alexandru V. Avram, Bing Wu, Xue Xiao, and Chunlei Liu. Integrated laplacian-based phase unwrapping and background phase removal for quantitative susceptibility mapping. *NMR in Biomedicine*, 27(2):219–227, 2014.

[7] Dong Zhou, Tian Liu, Pascal Spincemaille, and Yi Wang. Background field removal by solving the laplacian boundary value problem. *NMR in Biomedicine*, 27(3):312–319, 2014.

[8] Tian Liu, Ildar Khalidov, Ludovic de Rochefort, Pascal Spincemaille, Jing Liu, A. John Tsiouris, and Yi Wang. A novel background field removal method for MRI using projection onto dipole fields (PDF). *NMR in Biomedicine*, 24(9):1129–1136, 2011.

[9] Hongfu Sun and Alan H. Wilman. Background field removal using spherical mean value filtering and Tikhonov regularization. *Magnetic Resonance in Medicine*, 71(3):1151–1157, 2014.

[10] Wei Li, Bing Wu, and Chunlei Liu. Quantitative susceptibility mapping of human brain reflects spatial variation in tissue composition. *NeuroImage*, 55(4):1645 – 1656, 2011.

[11] Sam Wharton, Andreas Schäfer, and Richard Bowtell. Susceptibility mapping in the human brain using threshold-based k-space division. *Magnetic Resonance in Medicine*, 63(5):1292–1304, 2010.

[12] Berkin Bilgic, Itthi Chatnuntawech, Audrey P. Fan, Kawin Setsompop, Stephen F. Cauley, Lawrence L. Wald, and Elfar Adalsteinsson. Fast image reconstruction with L2-regularization. *Journal of Magnetic Resonance Imaging*, 40(1):181–191, 2014.

[13] Hongjiang Wei, Russell Dibb, Yan Zhou, Yawen Sun, Jianrong Xu, Nian Wang, and Chunlei Liu. Streaking artifact reduction for quantitative susceptibility mapping of sources with large dynamic range. *NMR in Biomedicine*, 28(10):1294–1303, 2015.

[14] Steffen Bollmann, Kasper Gade Bøtker Rasmussen, Mads Kristensen, Rasmus Guldhammer Blendal, Lasse Riis Østergaard, Maciej Plocharski, Kieran O'Brien, Christian Langkammer, Andrew Janke, and Markus Barth. DeepQSM - using deep learning to solve the dipole inversion for quantitative susceptibility mapping. *NeuroImage*, 195:373 – 383, 2019.

[15] Daniel Polak, Itthi Chatnuntawech, Jaeyeon Yoon, Siddharth Srinivasan Iyer, Carlos Milovic, Jongho Lee, Peter Bachert, Elfar Adalsteinsson, Kawin Setsompop, and Berkin Bilgic. Nonlinear dipole inversion (NDI) enables robust quantitative susceptibility mapping (QSM). *NMR in Biomedicine*, n/a(n/a):e4271, 2010. e4271 NBM-19-0164.R2.

[16] Kerstin Hammernik, Teresa Klatzer, Erich Kobler, Michael P. Recht, Daniel K. Sodickson, Thomas Pock, and Florian Knoll. Learning a variational network

for reconstruction of accelerated MRI data. *Magnetic Resonance in Medicine*, 79(6):3055–3071, 2018.

[17] Ruud JG van Sloun, Regev Cohen, and Yonina C Eldar. Deep learning in ultrasound imaging. *Proceedings of the IEEE*, 108(1):11–29, 2019.

[18] Christian Langkammer, Ferdinand Schweser, Karin Shmueli, Christian Kames, Xu Li, Li Guo, Carlos Milovic, Jinsuh Kim, Hongjiang Wei, Kristian Bredies, Sagar Buch, Yihao Guo, Zhe Liu, Jakob Meineke, Alexander Rauscher, José P. Marques, and Berkin Bilgic. Quantitative susceptibility mapping: Report from the 2016 reconstruction challenge. *Magnetic Resonance in Medicine*, 79(3):1661–1673, 2018.

[19] Chunlei Liu. Susceptibility tensor imaging. *Magnetic Resonance in Medicine*, 63(6):1471–1477, 2010.

[20] Carlos Milovic, Julio Acosta-Cabronero, José Miguel Pinto, Hendrik Mattern, Marcelo Andia, Sergio Uribe, and Cristian Tejos. A new discrete dipole kernel for quantitative susceptibility mapping. *Magnetic Resonance Imaging*, 51:7 – 13, 2018.

[21] Neal Parikh and Stephen Boyd. Proximal algorithms. *Foundations and Trends® in Optimization*, 1(3):127–239, 2014.

[22] Morteza Mardani, Qingyun Sun, David Donoho, Vardan Papyan, Hatef Monajemi, Shreyas Vasanawala, and John Pauly. Neural proximal gradient descent for compressive imaging. In S. Bengio, H. Wallach, H. Larochelle, K. Grauman, N. Cesa-Bianchi, and R. Garnett, editors, *Advances in Neural Information Processing Systems 31*, pages 9573–9583. Curran Associates, Inc., 2018.

[23] Tian Liu, Pascal Spincemaille, Ludovic de Rochefort, Bryan Kressler, and Yi Wang. Calculation of susceptibility through multiple orientation sampling (COSMOS): A method for conditioning the inverse problem from measured magnetic field map to susceptibility source image in MRI. *Magnetic Resonance in Medicine*, 61(1):196–204, 2009.

7

Conclusion

Binnen de perken zijn de mogelijkheden even onbeperkt als daarbuiten.

Jules Deelder

Electromagnetic fields are an integral part of nuclear magnetic resonance experiments and magnetic resonance imaging in particular. Careful consideration of their interaction with the magnetisation present in matter has led to the development of fast Fourier imaging and more advanced concepts such as magnetic resonance fingerprinting. In this work the focus was on the interaction with dielectric (and magnetic) tissue properties. These interactions are governed by the Maxwell equations instead of the Bloch equations (which describe the time evolution of the magnetisation).

Investigating these interactions, we have seen that carefully chosen approximations can lead to very efficient imaging methods, but also that all these approximations come at a cost. More specifically, the key contributions of this thesis are

1. the introduction of a direct induced current imaging method for $\tilde{B}_1^+$ measurements performed in the midplane of a birdcage coil as well as electrical properties imaging method based on these measurements,

2. a thorough investigation of the errors introduced in electrical properties methods by assuming a two-dimensional field structure in the midplane of a birdcage coil,

3. the extension of the target field method to a transverse oriented background field,

4. development of a new comprehensive signal model for MRI including scattering contributions, and application of a closed-form approximation of this model to electrical properties reconstruction,

5. the application of a proximal gradient descend approach to quantitative susceptibility mapping.

The following conclusions can be drawn regarding these contributions:

First-order current imaging By using the two-dimensional field structure present in the midplane of a birdcage coil we could directly relate the induced currents to the measured field without any assumptions on the homogeneity of the object (which is necessary in Helmholtz equation based electrical properties methods for example). This means only a first order differential operation is required, as opposed to a second order differentiation, resulting in less noise sensitivity of the method. Additionally, since the currents can be reconstructed directly, the electrical properties follow from what is essentially a forward operation. Unfortunately, the method still requires the incident or background fields to be known to perform this operation. This reconstruction method provides a very straightforward way to investigate error sources in electrical properties tomography methods by giving direct insight into the induced currents, and therefore the influence of the dielectric properties on the measured field, reflecting local changes in signal intensity for example.

Two dimensionality assumption As the first-order current imaging method relies on the fields inside a birdcage coil being two-dimensional, that is, they can be decoupled into TE and TM polarised waves, which allows for the direct relation between currents and field, we decided to thoroughly investigate this assumption. This was done in the context of contrast source inversion, since this inversion methodology provides a straightforward extension from two- to three-dimensional fields, and can be related to first-order current imaging when the two-dimensional assumption holds. We observe that even in the midplane of a birdcage coil the two-dimensional assumption does not hold when the object is not sufficiently translationally invariant in the longitudinal (out of plane) direction. We did manage to show that the error on the amplitude of the field is less of an issue than the error in the phase. Additionally, at the field strenghts considered, the error of conductivity reconstruction was less pronounced than the error of the permittivity reconstructions, where it seems that the out of plane contributions of the fields (and currents), which are not considered in the two-dimensional approximation, completely offsets the reconstruction.

Target field method for transverse background fields Applying the target field method to a different orientation showcases the great power and flexibility of this approach. Though the relation between the currents on a cylindrical sheet and the transverse magnetic field inside this cylinder is less straightforward than with a longitudinally oriented field, the method still works very well. This difference can be attributed mainly to the fact that the longitudinal direction is an invariant direction with respect to the current-carrying geometry whereas the transverse direction will always have to be represented by two of the axes of this given cylindrical geometry (the radius and angle). Similar to the original target field formulation the longitudinally directed gradient is the most difficult orientation to design due to the inherent relationship between the proximity to the current sheet and the field strength generated, leading to a much smaller linear region for this orientation. It is encouraging to see how after almost 40 years these analytic methods still provide a great tool for providing insight into the physics and it potentially provides a means of quickly evaluating designs for iterative optimisation methods.

Generalised signal models To wrap up our investigation of the electric tissue properties, we present the derivation for a full-wave measurement model for an magnetic resonance imaging (MRI) examination. Such a model be used to simulate the perturbations in a loop or dipole MRI measurement caused by dielectric tissue. The models are computationally complex, therefore we also present closed-form simplifications for a spherical homogeneous object. These simplified models are then used to present a reconstruction method based on a free induced decay (FID) signal. This directly proves the application and necessity of more complex signal models, for example for electrical properties tomography. Additionally, the model could also be used for antenna optimisation or sequence design.

Proximal gradient approach to QSM Combining machine learning with model based inversion methods can lead to the best of both worlds. Fast and reliable convergence from the model and easy tuning of regularisation parameters using machine learning tools. We have shown an application of these to the QSM dipole inversion problem, where the model is known accurately but choosing a regularisation is not straighforward. Generally QSM images combine sparse high intensity areas with a low rank background image, but this is not sufficient to create a robust regulariser. This approach allows for the correct regularisation to be learned for these types of images.

7.1. Dielectric Properties

There are different ways to perform electrical properties imaging, direct and iterative inversion methods in particular are presented. Under specific conditions the relationships between electric fields and properties can be significantly simplified which is exploited by direct current imaging. In reality, however, the matter is much more complex than that and accurately assessing the image quality and artefacts is not an easy feat. Therefore, we point towards three-dimensional methods and fully understanding the measured signal as potential solutions. Though those problems are much more complex than the simplified reconstruction methods, they are the only way we can guarantee accurate reconstruction of the *actual* electrical properties. As we have seen using the full wave signal model, the influence of the electrical properties on a measurement is very difficult to distinguish from for example the proton density or permeability, which can cause over and underestimates of either value giving the same results, or in other words the inverse problem does not have a unique solution without additional constraints.

This is of critical importance if we want electrical properties imaging to become a clinically relevant tool for diagnostics. If there is no reliable measure of “healthy” and “pathological” tissue properties for specific tissue types and organs at the measured frequencies, there is no way to reliably diagnose diseases based on electrical properties alone. If we do manage to get these *in-vivo* measures, however, they can provide an entirely new dimension to diagnostic tools and for example machine learning approaches to medical diagnostics. In this way, the accuracy and possibly generalisability of tools and pathologies is increased, as well as greatly increasing

safety of MRI examinations through accurate specific absorption rate (SAR) predictions.

7.2. Electromagnetic Fields in MRI

Through the generalised signal model that we have presented in this thesis, we have shown that for sufficiently high magnetic background fields the interaction between electrical properties and (electro-) magnetic fields in MRI is more complicated than usually assumed. The complication comes from two different sources. First of all, the antennas are usually operating in the near field, since the antenna is located as closely as possible to the tissue. Second, and more importantly, scattering from dielectric tissue is not considered. In other words, standard signal modeling is based on a quasi-static field assumption in which dielectric scattering is not taken into account, since in static electromagnetic fields we would not observe scattering. However, we show that given an electric field measurement (that is, a dipole antenna) these effects are present even at relatively low, clinical, MRI field strengths. This can then be exploited, for example, to measure the electrical properties of an object under consideration even from a simple free induction decay signal. Additionally, it provides insight into antenna geometry optimisation and could even lead to sequence design improvements for conventional imaging applications.

All these observations point to opportunities for a more complex signal model, unfortunately these are not without their challenges. Before investigating all the various ways in which the not-yet considered signal components can play a role, it is imperative to *validate* this model. We believe this to be the most important step at this point in the investigation, and there are a number of ways to go about it. For example, constructing a spherical phantom such as the one considered in the simplified closed-form signal model allows us to compare measurements with simulation, and attempting to reconstruct electrical properties from an FID measurement of the sphere to validate this approach. Additionally, a finite difference time domain (FDTD) method could be used to compare short time measurements (where the oscillations of the magnetic precession can be observed) for various phantom types where the phase change due to conductivity could be investigated.

A

Target Field Method

Well if you gotta read directions,
baby let me tell you, it's bad engineering,
cause the UI should explain what it does,
and if you have experience with other devices
you should be able to figure it out.

Reggie Watts

To make the target field method accessible and share our findings with respect to the design for a transverse magnetic field a Python based design tool was developed. This chapter serves as a brief description of the tool, the details of the transverse field derivation, as well as an investigation of the inductance computation which is performed.

A.1. Details of the Modified Target Field Method

We denote the domain inside the cylinder Region I, while the domain outside the cylinder is called Region II. Field quantities having their support in these domains carry a corresponding superscript.

The magnetic field in both domains is governed by the field equations $\nabla \cdot \boldsymbol{B} = 0$ and $\nabla \times \boldsymbol{B} = \boldsymbol{0}$. The latter equation is satisfied if we write $\boldsymbol{B} = -\nabla\Phi$, where Φ is the scalar magnetic potential. Substitution in the first field equation gives $\nabla^2\Phi = 0$. In other words, the potential satisfies Laplace's equation inside and outside the cylinder. Writing this equation in cylindrical coordinates, we have

$$\frac{\partial^2\Phi^{\mathrm{I,II}}}{\partial r^2} + \frac{1}{r}\frac{\partial\Phi^{\mathrm{I,II}}}{\partial r} + \frac{1}{r^2}\frac{\partial^2\Phi^{\mathrm{I,II}}}{\partial\phi^2} + \frac{\partial^2\Phi^{\mathrm{I,II}}}{\partial z^2} = 0. \tag{A.1}$$

Furthermore, at the current-carrying surface $r = a$ we have the boundary conditions

$$\lim_{r\uparrow a}\frac{\partial\Phi^{\mathrm{I}}}{\partial r} = \lim_{r\downarrow a}\frac{\partial\Phi^{\mathrm{II}}}{\partial r}, \tag{A.2}$$

A

$$\lim_{r\uparrow a}\frac{1}{r}\frac{\partial\Phi^{\mathrm{I}}}{\partial\phi}-\lim_{r\downarrow a}\frac{1}{r}\frac{\partial\Phi^{\mathrm{II}}}{\partial\phi}=\mu_0 J_z, \tag{A.3}$$

and

$$\lim_{r\downarrow a}\frac{\partial\Phi^{\mathrm{II}}}{\partial z}-\lim_{r\uparrow a}\frac{\partial\Phi^{\mathrm{I}}}{\partial z}=\mu_0 J_\phi, \tag{A.4}$$

and, finally, the surface current must satisfy the continuity equation:

$$\frac{\partial J_z}{\partial z}+\frac{1}{a}\frac{\partial J_\phi}{\partial\phi}=0. \tag{A.5}$$

Applying the Fourier transformation (4.3, which transforms with respect to ϕ and z) to Laplace's equation, the boundary conditions, and the continuity equation, we obtain the spectral domain equations

$$r^2\frac{\partial^2\tilde{\Phi}^{[m]}}{\partial r^2}+r\frac{\partial\tilde{\Phi}^{[m]}}{\partial r}-(m^2+k^2r^2)\tilde{\Phi}^{[m]}=0, \tag{A.6}$$

$$\lim_{r\uparrow a}\frac{\partial\tilde{\Phi}^{\mathrm{I};[m]}}{\partial r}=\lim_{r\downarrow a}\frac{\partial\tilde{\Phi}^{\mathrm{II};[m]}}{\partial r}, \tag{A.7}$$

$$\mathrm{j}m\left(\lim_{r\uparrow a}\frac{1}{r}\tilde{\Phi}^{\mathrm{I};[m]}-\lim_{r\downarrow a}\frac{1}{r}\tilde{\Phi}^{\mathrm{II};[m]}\right)=\mu_0\tilde{J}_z^{[m]}, \tag{A.8}$$

and

$$\mathrm{j}k\left(\lim_{r\downarrow a}\tilde{\Phi}^{\mathrm{II};[m]}-\lim_{r\uparrow a}\tilde{\Phi}^{\mathrm{I};[m]}\right)=\mu_0\tilde{J}_\phi^{[m]} \tag{A.9}$$

and

$$ka\tilde{J}_z^{[m]}+m\tilde{J}_\phi^{[m]}=0. \tag{A.10}$$

Here m and k are the fourier transforms of $\partial_p hi$ and ∂_z respectively. As is well-known [1], the solution of (A.6) in Region I that is bounded at the origin is given by $\tilde{\Phi}^{\mathrm{I};[m]}(r,k)=\alpha_m(k)I_m(|k|\,r)$, where the coefficient $\alpha_m(k)$ is independent of r, while the solution in Region II that remains bounded as $r\to\infty$ is given by $\tilde{\Phi}^{\mathrm{II};[m]}(r,k)=\beta_m(k)K_m(|k|\,r)$ with $\beta_m(k)$ independent of r. Substituting these solutions in the boundary conditions, the coefficients are found as

$$\alpha_m(k)=-\mathrm{j}a\mu_0\frac{|k|}{k}K_m'(|k|\,a)\tilde{J}_\phi^{[m]} \tag{A.11}$$

and

$$\beta_m(k)=-\mathrm{j}a\mu_0\frac{|k|}{k}I_m'(|k|\,a)\tilde{J}_\phi^{[m]}. \tag{A.12}$$

Having the spectral domain potential at our disposal, the corresponding spectral domain magnetic field can be determined. Of particular interest is the magnetic field inside the cylinder (Region I), since the target field is prescribed in this region. Explicitly, for the magnetic field in Region I, we have

$$\begin{aligned}\tilde{B}_r^{\mathrm{I};[m]} &= -\frac{\partial \tilde{\Phi}^{\mathrm{I};[m]}}{\partial r} \\ &= \mathrm{j} a \mu_0 k I_m'(|k|\, r) K_m'(|k|\, a) \tilde{J}_\phi^{[m]},\end{aligned} \tag{A.13}$$

$$\begin{aligned}\tilde{B}_\phi^{\mathrm{I};[m]} &= -\frac{\mathrm{j}m}{r} \tilde{\Phi}^{\mathrm{I};[m]} \\ &= -\frac{a\mu_0}{r} m \frac{|k|}{k} I_m(|k|\, r) K_m'(|k|\, a) \tilde{J}_\phi^{[m]},\end{aligned} \tag{A.14}$$

and

$$\begin{aligned}\tilde{B}_z^{\mathrm{I};[m]} &= -\mathrm{j} k \tilde{\Phi}^{\mathrm{I};[m]} \\ &= -a\mu_0\, |k|\, I_m(|k|\, r) K_m'(|k|\, a) \tilde{J}_\phi^{[m]}.\end{aligned} \tag{A.15}$$

Now the target field is in the x-direction and is prescribed on the inner cylinder $r = b$. Writing this field in terms of its cylindrical components, we have

$$B_x(b, \phi, z) = B_r^{\mathrm{I}}(b, \phi, z) \cos(\phi) - B_\phi^{\mathrm{I}}(b, \phi, z) \sin(\phi) \tag{A.16}$$

and applying the Fourier transformation to the above equation gives:

$$\begin{aligned}\tilde{B}_x^{[m]}(b, k) = &\frac{1}{2} \left[\tilde{B}_r^{\mathrm{I};[m-1]}(b, k) + \tilde{B}_r^{\mathrm{I};[m+1]}(b, k) \right] \\ &- \frac{1}{2\mathrm{j}} \left[\tilde{B}_\phi^{\mathrm{I};[m-1]}(b, k) - \tilde{B}_\phi^{\mathrm{I};[m+1]}(b, k) \right].\end{aligned} \tag{A.17}$$

Substituting (A.13) and (A.14) in the above expression we arrive at (4.5).

A.1.1. Surface current density for a z-gradient coil

We show how we obtain the surface current from the prescribed target field for the design of a z-gradient coil. The analysis for an x- or y-gradient coil runs along similar lines. For a z-gradient coil, the Fourier transform of the target field is given by $\tilde{B}_x^{[m]}(b, k) = 2\pi g_z \tilde{\Gamma}_{\mathrm{In}}(k) \delta_{m,0}$, where the delta symbol denotes the Kronecker delta and

$$\tilde{\Gamma}_{\mathrm{In}}(k) = \int_{z=-\infty}^{\infty} \Gamma_{\mathrm{In}}(z) e^{-\mathrm{j}kz}\, \mathrm{d}z. \tag{A.18}$$

A

Note that $\tilde{\Gamma}_{\text{In}}(k)$ is imaginary and an odd function of k. Substitution of the Fourier transform of the target field in (4.5) gives

$$\begin{aligned} &2\pi g_z \tilde{\Gamma}_{\text{In}}(k)\delta_{m,0} = \\ &\frac{\mathrm{j}}{2}\left[\tilde{P}^{[m-1]}(b,k) - \tilde{Q}^{[m-1]}(b,k)\right]\tilde{J}_\phi^{[m-1]}(k) \\ &+ \frac{\mathrm{j}}{2}\left[\tilde{P}^{[m+1]}(b,k) + \tilde{Q}^{[m+1]}(b,k)\right]\tilde{J}_\phi^{[m+1]}(k). \end{aligned} \tag{A.19}$$

Since the left-hand side of this equation vanishes for m odd, we take a surface current for which all even numbered angular modes of its ϕ-component vanish, that is, we take $\tilde{J}_\phi^{[m]}(k) = 0$ for m even and $k \in \mathbb{R}$. Furthermore, for $m = 0$ we obtain

$$2\pi g_z \tilde{\Gamma}_{\text{In}}(k) = \frac{\mathrm{j}}{2}\left[\tilde{P}^{[1]}(b,k) + \tilde{Q}^{[1]}(b,k)\right]\left[\tilde{J}_\phi^{[-1]}(k) + \tilde{J}_\phi^{[1]}(k)\right],$$

where we have taken the symmetry of $\tilde{P}^{[m]}$ and $\tilde{Q}^{[m]}$ with respect to m into account. For the surface current we now take $\tilde{J}_\phi^{[-1]}(k) = \tilde{J}_\phi^{[1]}(k)$ and we obtain

$$\tilde{J}_\phi^{[1]}(k) = -\mathrm{j}\frac{2\pi g_z \tilde{\Gamma}_{\text{In}}(k)}{\tilde{P}^{[1]}(b,k) + \tilde{Q}^{[1]}(b,k)} = \tilde{J}_\phi^{[-1]}(k). \tag{A.20}$$

Similarly, for m even and not equal to zero ($m = 2n$, $n = \pm 1, \pm 2, \ldots$) the left-hand side vanishes and if we take a surface current for which all odd numbered angular modes are even with respect to m, that is,

$$\tilde{J}_\phi^{[-2n+1]}(k) = \tilde{J}_\phi^{[2n-1]}(k), \quad n = 1, 2, \ldots, \tag{A.21}$$

then we satisfy (A.19) if

$$\tilde{J}_\phi^{[2n+1]}(k) = -\frac{\tilde{P}^{[2n-1]}(b,k) - \tilde{Q}^{[2n-1]}(b,k)}{\tilde{P}^{[2n+1]}(b,k) + \tilde{Q}^{[2n+1]}(b,k)}\tilde{J}_\phi^{[2n-1]}(k), \tag{A.22}$$

for $n = 1, 2, \ldots$. In other words, all odd-numbered higher-order modes can be determined recursively starting from $\tilde{J}_\phi^{[1]}(k)$ as given by (A.20).

To obtain the ϕ-component of the surface current in the spatial domain, we substitute the modes in the Fourier inversion formula and include apodisation to obtain

$$\begin{aligned} J_\phi^z(\phi, z) &= \frac{1}{4\pi^2}\int_{k=-\infty}^{\infty}\sum_{m=-\infty}^{\infty}\tilde{J}_\phi^{[m]}(k)\tilde{T}(k)e^{\mathrm{j}m\phi}e^{\mathrm{j}kz}\,\mathrm{d}k \\ &= \frac{1}{2\pi^2}\sum_{\substack{m=1 \\ m\ \text{odd}}}^{\infty}\cos(m\phi)\int_{k=-\infty}^{\infty}\tilde{J}_\phi^{[m]}(k)\tilde{T}(k)e^{\mathrm{j}kz}\,\mathrm{d}k. \end{aligned} \tag{A.23}$$

The current consists of an infinite summation of odd-numbered angular modes. Each term in this series represents the ϕ-component of a surface current that produces its

own magnetic field. The total magnetic field consists of a superposition of these individual fields due to the linearity of the field equations. Since we want to realize a z-gradient coil in practice, we have to truncate the series and to keep the construction of the coil as simple as possible, we keep the first current term in the series only. Our final expression for the ϕ-component of the surface current becomes

$$\begin{aligned} J_\phi^z(\phi, z) &= \frac{1}{2\pi^2}\cos(\phi)\int_{k=-\infty}^{\infty} \tilde{J}_\phi^{[1]}(k)\tilde{T}(k)e^{\mathrm{j}kz}\,\mathrm{d}k \\ &= -\mathrm{j}\frac{g_z}{\pi}\cos(\phi)\int_{k=-\infty}^{\infty} \frac{\tilde{\Gamma}_{\mathsf{ln}}(k)\tilde{T}(k)}{\tilde{P}^{[1]}(b,k)+\tilde{Q}^{[1]}(b,k)}e^{\mathrm{j}kz}\,\mathrm{d}k. \end{aligned} \tag{A.24}$$

The z-component of the surface current that corresponds to (A.24) follows from the continuity equation for the surface current.

A.2. Inductance Computation

The inductance of a thin cylinder with given current density is given by [2] and [3] as

$$L = -\frac{\mu_0 a^2}{I^2}\sum_{m=-\infty}^{\infty}\int_{-\infty}^{\infty}\left|\tilde{J}_\phi^m(k)\right|^2 I'_m K'_m\,\mathrm{d}k. \tag{A.25}$$

Here a is the radius of the cylinder, I the current applied, μ_0 the vacuum permeability, $\tilde{J}^m$ the current density in the spatial frequency domain and I'_m and K'_m are the derivatives of the Bessel functions of order m. Unfortunately I couldn't find a rigorous derivation of this equation, but since it seemed to be common knowledge at the time I present a proof (or derivation) of this equation here for good measure.

Most of these notes are based on work by Turner and the doctoral thesis of Qin Liu. They describe in detail the derivation of the inductance based due to a current density on a thin cylinder. The energy of steady state currents can be written in terms of the vector potential $\boldsymbol{A}$ as

$$U = \frac{1}{2}\int \boldsymbol{J}\cdot\boldsymbol{A}\,\mathrm{d}V, \tag{A.26}$$

assuming steady currents in static magnetic fields[1]. Here $\boldsymbol{A}$ is the vector potential, and the integration is over $\mathbb{R}^3$. For a cylindrical coil, where the currents are confined to the surface of a cylinder of radius $r = a$, this simplifies in cylindrical coordinates to

$$U = \frac{a}{2}\int_{-\pi}^{\pi}\int_{\infty}^{\infty}\left(J_\phi A_\phi + J_z A_z\right)\,\mathrm{d}z\,\mathrm{d}\phi. \tag{A.27}$$

Now, we also know that for a coil of inductance L, the magnetic energy due to a current I flowing into this coil is given by[2].

$$U = \frac{1}{2}LI^2. \tag{A.28}$$

[1] This equation and a derivation for it can be found e.g. in Feynman's Lectures on Physics [4] (15–6, eq. 15.20) http://www.feynmanlectures.caltech.edu/II_15.html#mjx-eqn-EqII1520

[2] https://www.feynmanlectures.caltech.edu/II_17.html#mjx-eqn-EqII1737

A

Combining Equation (A.28) and Equation (A.27) gives us the following expression for the inductance of a cylindrical coil in terms of its current distribution

$$L = \frac{a}{I^2} \int_{-\pi}^{\pi} \int_{\infty}^{\infty} \left(J_\phi A_\phi + J_z A_z \right) \, \mathrm{d}z \, \mathrm{d}\phi. \tag{A.29}$$

To compute this expression we describe the currents in terms of the inverse Fourier transformed frequency domain currents

$$J_\phi(\phi, z) = \frac{1}{2\pi} \sum_{m=-\infty}^{\infty} \int_{-\infty}^{\infty} \tilde{J}_\phi(m, k) e^{\mathrm{j}m\phi} e^{\mathrm{j}kz} \, \mathrm{d}k, \tag{A.30}$$

$$J_z(\phi, z) = \frac{1}{2\pi} \sum_{m=-\infty}^{\infty} \int_{-\infty}^{\infty} \tilde{J}_z(m, k) e^{\mathrm{j}m\phi} e^{\mathrm{j}kz} \, \mathrm{d}k, \tag{A.31}$$

and the components of the vector potential are[3]

$$A_\phi(\phi, z) = \frac{\mu_0 a}{4\pi} \sum_{m=-\infty}^{\infty} \int_{-\infty}^{\infty} \tilde{J}_\phi(m, k) e^{\mathrm{j}m\phi} e^{\mathrm{j}kz} \tilde{G}_\phi \, \mathrm{d}k, \tag{A.32}$$

$$A_z(\phi, z) = \frac{\mu_0 a}{2\pi} \sum_{m=-\infty}^{\infty} \int_{-\infty}^{\infty} \tilde{J}_z(m, k) e^{\mathrm{j}m\phi} e^{\mathrm{j}kz} \tilde{G}_z \, \mathrm{d}k, \tag{A.33}$$

where we have used

$$\tilde{G}_\phi = I_{m-1}(|k|\, a) K_{m-1}(|k|\, a) + I_{m+1}(|k|\, a) K_{m+1}(|k|\, a). \tag{A.34}$$

and

$$\tilde{G}_z = I_m(|k|\, a) K_m(|k|\, a). \tag{A.35}$$

to ease the notation. Substituting these into Equation (A.29) we get

$$\begin{aligned} L = \frac{s}{2} \int_{-\pi}^{\pi} \int_{\infty}^{\infty} \sum_{m=-\infty}^{\infty} \int_{-\infty}^{\infty} \tilde{J}_\phi^m(k) e^{\mathrm{j}m\phi} e^{\mathrm{j}kz} \tilde{G}_\phi \, \mathrm{d}k \sum_{m'=-\infty}^{\infty} \int_{-\infty}^{\infty} \tilde{J}_\phi^{m'}(k') e^{\mathrm{j}m'\phi} e^{\mathrm{j}k'z} \, \mathrm{d}k' \, \mathrm{d}z \, \mathrm{d}\phi \\ + s \int_{-\pi}^{\pi} \int_{\infty}^{\infty} \sum_{m=-\infty}^{\infty} \int_{-\infty}^{\infty} \tilde{J}_z^m(k) e^{\mathrm{j}m\phi} e^{\mathrm{j}kz} \tilde{G}_z \, \mathrm{d}k \sum_{m'=-\infty}^{\infty} \int_{-\infty}^{\infty} \tilde{J}_z^{m'}(k') e^{\mathrm{j}m'\phi} e^{\mathrm{j}k'z} \, \mathrm{d}k' \, \mathrm{d}z \, \mathrm{d}\phi, \end{aligned}$$

[3] From "Shielded transverse gradient coil for in vivo nmr" by Qin Liu, 1991 [3]. Can also be found in "Passive screening of switched magnetic field gradients" by Turner and Bowley, 1986 [5].

with $s = \left(\mu_0 a^2\right)/\left(4\pi^2 I^2\right)$. The next step is to combine the inverse transforms of the vector potential and the current density according to

$$\int f(x)\mathrm{d}x \int g(x')\mathrm{d}x' = \iint g(x')f(x)\mathrm{d}x'\mathrm{d}x, \tag{A.36}$$

which holds for any converging integral. We can have the product of the functions inside the innermost integral because $f(x)$ does not change on integration w.r.t. x' and can therefore be considered a constant in regard to $\mathrm{d}x'$.

$$\begin{aligned} L = \frac{s}{2} &\int_{-\pi}^{\pi}\int_{\infty}^{\infty}\sum_{m=-\infty}^{\infty}\int_{-\infty}^{\infty}\sum_{m'=-\infty}^{\infty}\int_{-\infty}^{\infty} \tilde{J}_\phi^m(k)\tilde{J}_\phi^{m'}(k')e^{\mathrm{j}(m+m')\phi}e^{\mathrm{j}(k+k')z}\tilde{G}_\phi \,\mathrm{d}k'\,\mathrm{d}k\,\mathrm{d}z\,\mathrm{d}\phi \\ + s &\int_{-\pi}^{\pi}\int_{\infty}^{\infty}\sum_{m=-\infty}^{\infty}\int_{-\infty}^{\infty}\sum_{m'=-\infty}^{\infty}\int_{-\infty}^{\infty} \tilde{J}_z^m(k)\tilde{J}_z^{m'}(k')e^{\mathrm{j}(m+m')\phi}e^{\mathrm{j}(k+k')z}\tilde{G}_z \,\mathrm{d}k'\,\mathrm{d}k\,\mathrm{d}z\,\mathrm{d}\phi. \end{aligned}$$

Now we change the order of integration, and we integrate first over ϕ and z, on which it turns out only the exponentials inside the Fourier transformation depend. The following identities hold for these integral[4]

$$\int_{-\pi}^{\pi} e^{\mathrm{j}(m+m')\phi}\,\mathrm{d}\phi = 2\pi\delta_{m',-m} \quad \text{and} \quad \int_{-\infty}^{\infty} e^{\mathrm{j}(k+k')z}\,\mathrm{d}z = 2\pi\delta(k'+k), \tag{A.37}$$

which simplifies the expression to

$$\begin{aligned} L = &\frac{\mu_0 a^2}{2I^2}\sum_{m=-\infty}^{\infty}\int_{-\infty}^{\infty}\sum_{m'=-\infty}^{\infty}\int_{-\infty}^{\infty} \tilde{J}_\phi^m(k)\tilde{J}_\phi^{m'}(k')\delta_{m',-m}\delta(k'+k)\tilde{G}_\phi \,\mathrm{d}k'\,\mathrm{d}k \\ + &\frac{\mu_0 a^2}{I^2}\sum_{m=-\infty}^{\infty}\int_{-\infty}^{\infty}\sum_{m'=-\infty}^{\infty}\int_{-\infty}^{\infty} \tilde{J}_z^m(k)\tilde{J}_z^{m'}(k')\delta_{m',-m}\delta(k'+k)\tilde{G}_z \,\mathrm{d}k'\,\mathrm{d}k. \end{aligned}$$

Since $\delta_{m',-m} = 1$ for $m' = -m$ and $\delta(k'+k)$ is the Dirac delta, we can further simplify the integration and summation over k' and m' to

$$L = \frac{\mu_0 a^2}{2I^2}\sum_{m=-\infty}^{\infty}\int_{-\infty}^{\infty} \tilde{J}_\phi^m(k)\tilde{J}_\phi^{-m}(-k)\tilde{G}_\phi \,\mathrm{d}k + \frac{\mu_0 a^2}{I^2}\sum_{m=-\infty}^{\infty}\int_{-\infty}^{\infty} \tilde{J}_z^m(k)\tilde{J}_z^{-m}(-k)\tilde{G}_z \,\mathrm{d}k.$$

By definition $\tilde{J}_\phi^{-m}(-k)$ and $\tilde{J}_z^{-m}(-k)$ are the complex conjugates of $\tilde{J}_\phi^m(k)$ and $\tilde{J}_z^m(k)$

[4] http://mathworld.wolfram.com/DeltaFunction.html eq. (31), and http://functions.wolfram.com/IntegerFunctions/DiscreteDelta/introductions/TensorFunctions/ShowAll.html under Integral representations

A

respectively, therefore $\tilde{J}_\phi^{-m}(-k)\tilde{J}_\phi^m(k) = \left|\tilde{J}_\phi^m(k)\right|^2$. Furthermore, since[5]

$$\tilde{J}_\phi^m(k) = -\frac{ka}{m}\tilde{J}_z^m(k), \tag{A.38}$$

it follows that $\left|\tilde{J}_z^m(k)\right|^2 = \frac{m^2}{k^2a^2}\left|\tilde{J}_\phi^m(k)\right|^2$, and

$$L = \frac{\mu_0 a^2}{I^2}\sum_{m=-\infty}^{\infty}\int_{-\infty}^{\infty}\frac{1}{2}\left|\tilde{J}_\phi^m(k)\right|^2\tilde{G}_\phi + \frac{m^2}{k^2a^2}\left|\tilde{J}_\phi^m(k)\right|^2\tilde{G}_z\,\mathrm{d}k.$$

Finally we use the Bessel function identity

$$\begin{aligned} I_{m-1}(|k|\,a)K_{m-1}(|k|\,a) + I_{m+1}(|k|\,a)K_{m+1}(|k|\,a) = \\ -2\Big(I'_m(|k|\,a)K'_m(|k|\,a) + \frac{m^2}{k^2a^2}I_m(|k|\,a)K_m(|k|\,a)\Big), \end{aligned} \tag{A.39}$$

to rewrite $\tilde{G}_\phi$ as

$$\tilde{G}_\phi = -2\Big(I'_m(|k|\,a)K'_m(|k|\,a) + \frac{m^2}{k^2a^2}\tilde{G}_z\Big). \tag{A.40}$$

And the inductance follows as

$$\begin{aligned} L &= -\frac{\mu_0 a^2}{I^2}\sum_{m=-\infty}^{\infty}\int_{-\infty}^{\infty}\left|\tilde{J}_\phi^m(k)\right|^2\left(I'_mK'_m + \frac{m^2}{k^2a^2}I_mK_m - \frac{m^2}{k^2a^2}I_mK_m\right)\mathrm{d}k \\ &= -\frac{\mu_0 a^2}{I^2}\sum_{m=-\infty}^{\infty}\int_{-\infty}^{\infty}\left|\tilde{J}_\phi^m(k)\right|^2 I'_mK'_m\,\mathrm{d}k. \end{aligned} \tag{A.41}$$

This is in good agreement with the results found in e.g. Turner 1993. □

A.3. Open Source Gradient Design Tool

To facility open access research and open source tools the equations and numerical implementation of the gradient field method (for transverse electric fields) has been made into an open source tool as well. Major credits for refactoring the code into readable python go to Thomas O'Reilly, who has also made a user-friendly graphical user interface (GUI) for others to use. This tool can be found at `https://github.com/LUMC-LowFieldMRI/GradientDesignTool` including all the python code, and the graphical user interface is shown in Figure A.1.

[5] see "Gradient Coil Design: A Review of Method" by Turner 1993 (eq. 26), or B. de Vos "Gradient Coil Design and Construction for a Halbach Based MRI system" (eq. 2.39)

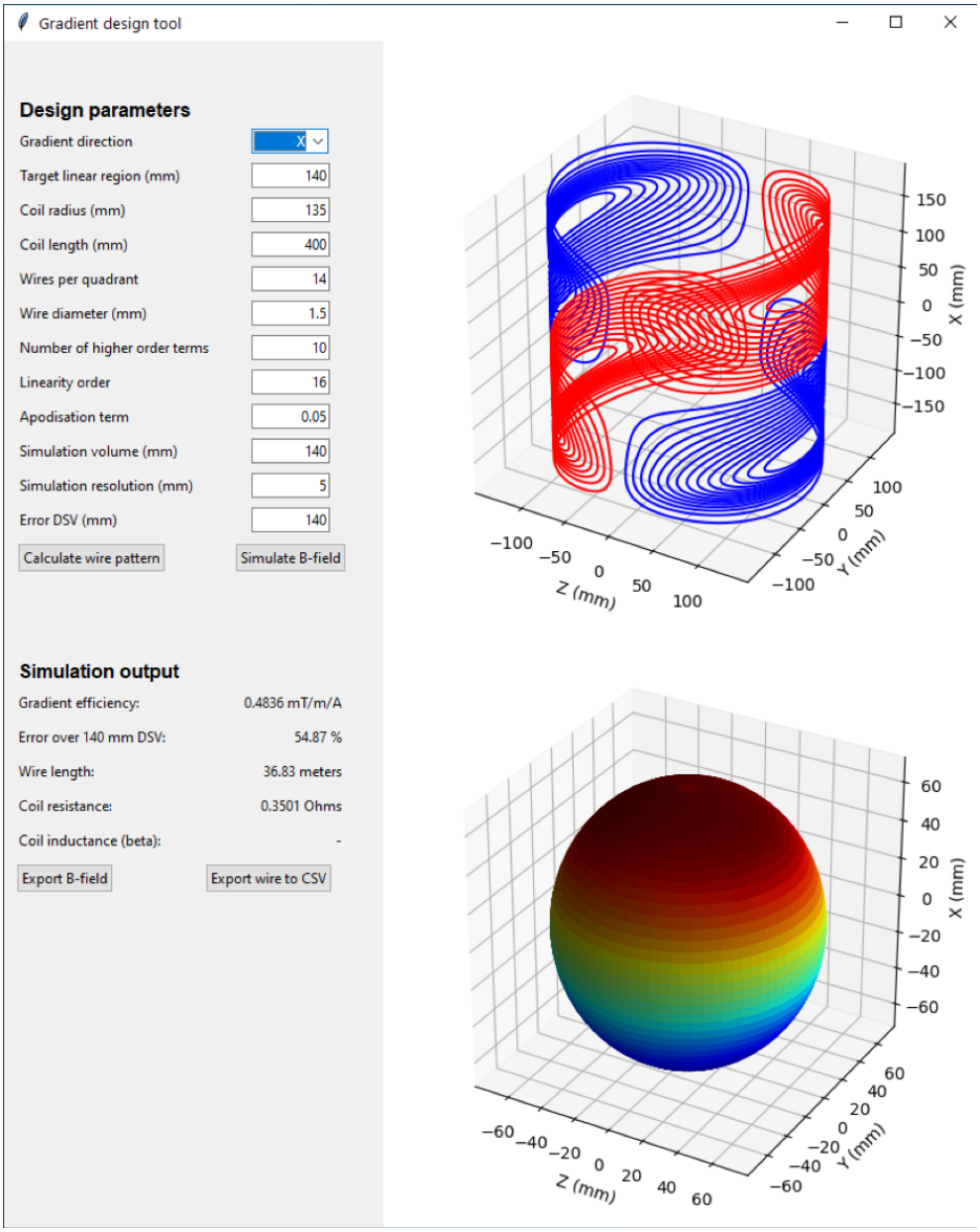

Figure A.1: The graphical user interface of the gradient design tool, which allows easy simulation of the target field method for transverse oriented magnetic field configurations. The full tool can be found at `https://github.com/LUMC-LowFieldMRI/GradientDesignTool`.

A

References

[1] Jianming Jin. *Electromagnetic Analysis and Design in Magnetic Resonance Imaging*. CRC Press, 1999.

[2] Robert Turner. Gradient coil design: A review of methods. *Magnetic Resonance Imaging*, 11(7):903 – 920, 1993.

[3] Qin Liu. Design of gradient and shim coil systems for in vivo NMR. In *PhD Thesis*, 1996.

[4] Richard P Feynman, Robert B Leighton, and Matthew Sands. *The Feynman lectures on physics, Vol. II: The new millennium edition: Mainly Electromagnetism and Matter*, volume 2. California Institute of Technology, 2011.

[5] R Turner. A target field approach to optimal coil design. *Journal of Physics D: Applied Physics*, 19(8):L147–L151, aug 1986.

B

Expansion vectors for time-domain signal models

The expansion vectors for a magnetic field measurement are given by

$$\boldsymbol{r}_0^{\mathsf{mg}} = \boldsymbol{p}_1, \tag{B.1}$$

$$\boldsymbol{r}_1^{\mathsf{mg}} = \boldsymbol{p}_1 + \frac{1}{3} Z_0 \sigma \left[(\boldsymbol{x}' \cdot \boldsymbol{\nu}) \boldsymbol{n} - (\boldsymbol{x}' \cdot \boldsymbol{n}) \boldsymbol{\nu} \right], \tag{B.2}$$

$$\begin{aligned} \boldsymbol{r}_2^{\mathsf{mg}} = \boldsymbol{p}_2 &+ \frac{1}{3} Z_0 \sigma \left[(\boldsymbol{x}' \cdot \boldsymbol{\nu}) \boldsymbol{n} - (\boldsymbol{x}' \cdot \boldsymbol{n}) \boldsymbol{\nu} \right] \\ &+ \frac{1}{3} (\varepsilon_{\mathsf{r}} - 1) \frac{(\boldsymbol{x}' \cdot \boldsymbol{\nu}) \boldsymbol{n} - (\boldsymbol{x}' \cdot \boldsymbol{n}) \boldsymbol{\nu}}{|\boldsymbol{x}' - \boldsymbol{x}_{\mathsf{R}}|}, \end{aligned} \tag{B.3}$$

$$\boldsymbol{r}_3^{\mathsf{mg}} = \frac{1}{3} (\varepsilon_{\mathsf{r}} - 1) \frac{(\boldsymbol{x}' \cdot \boldsymbol{\nu}) \boldsymbol{n} - (\boldsymbol{x}' \cdot \boldsymbol{n}) \boldsymbol{\nu}}{|\boldsymbol{x}' - \boldsymbol{x}_{\mathsf{R}}|}, \tag{B.4}$$

where Z_0 is the impedance of vacuum and ε_{r} the relative permittivity of the ball. The expansion vectors for an electric field measurement are given by with

$$\boldsymbol{r}_0^{\mathsf{el}} = \frac{\sigma}{3} \boldsymbol{x}' \times \boldsymbol{p}_1, \tag{B.5}$$

$$\boldsymbol{r}_1^{\mathsf{el}} = Y_0 \boldsymbol{q} + \frac{\sigma}{3} \boldsymbol{x}' \times \boldsymbol{p}_1, \tag{B.6}$$

$$\boldsymbol{r}_2^{\mathsf{el}} = Y_0 \boldsymbol{q} + \frac{\sigma}{3} \boldsymbol{x}' \times \boldsymbol{p}_2, \tag{B.7}$$

$$\boldsymbol{r}_3^{\mathsf{el}} = \frac{1}{3} Y_0 (\varepsilon_{\mathsf{r}} - 1) \frac{\boldsymbol{x}' \times \boldsymbol{p}_2}{|\boldsymbol{x}' - \boldsymbol{x}_{\mathsf{R}}|}, \tag{B.8}$$

where $Y_0 = (\varepsilon_0 / \mu_0)^{1/2}$ is the admittance of vacuum, and

$$\boldsymbol{q} = \boldsymbol{\nu} \times \boldsymbol{n} + \frac{1}{3} (\varepsilon_{\mathsf{r}} - 1) \frac{\boldsymbol{x}' \times \boldsymbol{p}_1}{|\boldsymbol{x}' - \boldsymbol{x}_{\mathsf{R}}|}. \tag{B.9}$$

Note that these expansion vectors are independent of s, but do depend on the distance $|\boldsymbol{x}' - \boldsymbol{x}_{\mathsf{R}}|$.

C

Finite Difference Time Domain implementation with Uni-axial Perfectly Matched Layer

The full equations used in the finite difference time domain (FDTD) simulation are described and derived from the Maxwell equations here. First the normal update equations are shown and then the uniaxial perfectly matched layer (UPML) formulation used in the actual simulations is described.

C.1. The Maxwell equations

The FDTD method is used to solve Maxwell's equations by time stepping the fields. In all of our scenarios we are dealing with an object that is in free space, which means that the fields propagate outwards without reflections from a boundary. To perform this operation in our discretised space we require a perfectly matched layer (PML) which will essentially absorb the waves travelling out of our discrete domain. To describe the relationships between the field and incorporate our perfectly matched layer we use the Maxwell equations

$$\nabla \times \boldsymbol{E}(t, \boldsymbol{r}) + \partial_t \boldsymbol{B}(t, \boldsymbol{r}) = -\boldsymbol{K}(t, \boldsymbol{r}), \tag{C.1}$$

$$-\nabla \times \boldsymbol{H}(t, \boldsymbol{r}) + \partial_t \boldsymbol{D}(t, \boldsymbol{r}) + \boldsymbol{J}_c(t, \boldsymbol{r}) = -\boldsymbol{J}(t, \boldsymbol{r}). \tag{C.2}$$

Here $\boldsymbol{K}$ and $\boldsymbol{J}$ describe magnetic and electric source densities, the field quantities $\boldsymbol{E}, \boldsymbol{D}, \boldsymbol{J}_c$ describe electric fields and $\boldsymbol{B}$ and $\boldsymbol{H}$ describe the magnetic fields. The magnetic and dielectric properties μ, σ, ε are incorporated in the field quantities through the constitutive equations

$$\boldsymbol{D} = \varepsilon \boldsymbol{E}, \qquad \boldsymbol{J}_c = \sigma \boldsymbol{E} \qquad \text{and} \qquad \boldsymbol{B} = \mu \boldsymbol{H}. \tag{C.3}$$

Furthermore, $\boldsymbol{r}$ is used to denote the position of the fields and t is the time.

To get to the FDTD formulation we discretise these equations spatially as well as temporally and perform several approximations to get a system of matrix equations that can easily be solved by a computer.

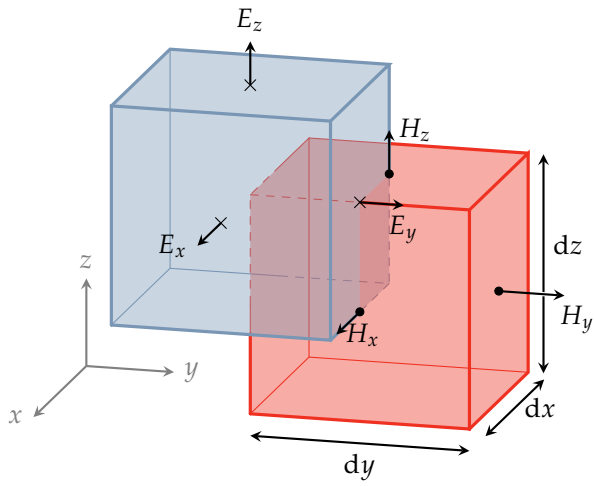

Figure C.1: A staggered Yee grid for three dimensional electromagnetic fields. The blue and red cubes denote the grid cells for electric and magnetic field respectively. Both consist of isotropic voxels with dimensions $\mathrm{d}x = \mathrm{d}y = \mathrm{d}z$.

C.2. Discretisation Procedure

Both for the temporal and the spatial discretisations staggered grids will be used. Why we offset the electric and magnetic fields by half a grid distance will become clear when we arrive at the final update equations. This approach was first introduced by Yee [1], and is nowadays implemented in all conventional FDTD solvers. For the rest of this section and the UPML implementation the notation and derivation of [2] will be followed.

C.2.1. Yee (Staggered) Grid

The gridding is staggered such that each magnetic field component is half a grid cell away from the respective electric field component. Furthermore, the field components themselves (x, y, z) are distributed on the Yee cell at the various cell faces. This configuration can be found in Figure C.1. As can be seen from this illustration there will be one grid which has cells half a voxel outside of the other grid. We denote this as primary and secondary grid, where the primary grid will contain the outermost voxels and the secondary grid will necessarily contain 2 voxels less in each dimension.

In our implementation the primary grid is the magnetic field gridding, and the secondary grid the electric field grid. This grid does not necessarily have to be isotropic (that is x, y, z discretisations are equal) but in all simulations performed in this thesis an isotropic gridding is used, since spherical objects are considered which take up the same amount of space in each dimension.

Lastly, for implementing the operators as matrix vector products the different field components (F_x, F_y and F_z) are concatenated, and the coordinates are ordered in a

$x-$lexicographic fashion. That is

$$\mathbf{f} = \left[\mathbf{f}_x, \mathbf{f}_y, \mathbf{f}_z\right]^T, \tag{C.4}$$

and

$$\mathbf{f}_r = \left[F_r(x_0, y_0, z_0), F_r(x_1, y_0, z_0), \ldots, F_r(x_0, y_1, z_0), F_r(x_1, y_1, z_0), \ldots\right]^T. \tag{C.5}$$

Here $\mathbf{f}$ is used to denote a discretised field vector and $F_r(x, y, z)$ a continuous field quantity r component of the yee cell with center at position (x, y, z).

The discrete curl of a field can then simply be described by a differencing matrix operation on the field vector as

$$\nabla \times \boldsymbol{F} \rightarrow \mathrm{D}_f \mathbf{f}, \tag{C.6}$$

where the subscript denotes the specific grid on which the curl operation takes place (the grid on which the specific discretised field lives).

C.2.2. Temporal Discretisation

For the temporal discretisation we again split up the fields and discretise them on different time steps. Here we discretise (for notation' sake) the electric field on the "whole" time steps and the magnetic field on the "half" time steps, so exactly between the electric field time instances.

For approximating fields at a different time point than which they are defined at, so for example to approximate the electric field at time step $i + 1/2$ we make use of the semi implicit approximation

$$\mathsf{f}^{i+1/2} = \frac{\mathsf{f}^i + \mathsf{f}^{i+1}}{2}, \tag{C.7}$$

where the superscript denotes the (discrete) time step at which the field value f is evaluated. Furthermore, to discretise the temporal derivative a centralised differencing approach is taken, which leads to

$$\partial_t \mathsf{f}^i = \frac{\mathsf{f}^{i+1/2} - \mathsf{f}^{i-1/2}}{\Delta \mathsf{t}} \tag{C.8}$$

where $\Delta \mathsf{t}$ is the time step used.

C.2.3. Medium Discretisation

Since the field components and fields are offset from one another the medium parameters need to be computed at the correct positions, as well as averaged over the different voxels depending on their application. For the permeability the harmonic average is used and the permittivity and conductivity the mean is used for the cells which contain medium boundaries.

C.2.4. Discrete Maxwell Equations

Now we have all the tools necessary to discretise the Maxwell equations as they are given in (C.1) and (C.2). The source densities are discretised in the same fashion as the field quantities (K source on the magnetic field gridding and J sources on the electric field grid). Also, we will first consider the regular equations without constitutive PML tensor $\underline{s}$, this tensor will be considered in Section C.3. This leads to the following discretised equations

C

$$\mathsf{D}_e \mathbf{e}^i + \frac{\mu}{\Delta \mathrm{t}} \left(\mathbf{h}^{i+1/2} - \mathbf{h}^{i-1/2} \right) = -\mathbf{k}^i, \tag{C.9}$$

$$-\mathsf{D}_h \mathbf{h}^{i+1/2} + \frac{\varepsilon}{\Delta \mathrm{t}} \left(\mathbf{e}^{i+1} - \mathbf{e}^i \right) + \frac{\sigma}{2} \left(\mathbf{e}^i + \mathbf{e}^{i+1} \right) = -\mathbf{j}^{i+1/2}, \tag{C.10}$$

where we have substituted the constitutive relationships. These equations can be rewritten into update equations by collecting all the future terms on one side, and all past or current terms on the other.

$$\mathbf{h}^{i+1/2} = \mathbf{h}^{i-1/2} - \frac{\Delta \mathrm{t}}{\mu} \left(\mathsf{D}_e \mathbf{e}^i + \mathbf{k}^i \right), \tag{C.11}$$

$$\mathbf{e}^{i+1} = \frac{(2\varepsilon - \sigma \Delta \mathrm{t})}{(2\varepsilon + \sigma \Delta \mathrm{t})} \mathbf{e}^{i-1} + \frac{2\Delta \mathrm{t}}{(2\varepsilon + \sigma \Delta \mathrm{t})} \left(\mathsf{D}_h \mathbf{h}^{i+1/2} - \mathbf{j}^{i+1/2} \right). \tag{C.12}$$

C.3. Uni-axial Perfectly Matched Layer

To describe the perfectly matched layer which is required to prevent reflections from the boundary of the simulation space a general constitutive tensor $\underline{s}$ is introduced. The Maxwell equations with this added tensor are

$$\nabla \times \boldsymbol{E}(t, \boldsymbol{r}) + \partial_t \underline{s} \boldsymbol{B}(t, \boldsymbol{r}) = -\boldsymbol{K}(t, \boldsymbol{r}), \tag{C.13}$$

$$-\nabla \times \boldsymbol{H}(t, \boldsymbol{r}) + \partial_t \underline{s} \boldsymbol{D}(t, \boldsymbol{r}) + \underline{s} \boldsymbol{J}_c(t, \boldsymbol{r}) = -\boldsymbol{J}(t, \boldsymbol{r}). \tag{C.14}$$

With constitutive tensor

$$\underline{s} = \begin{bmatrix} \frac{s_y s_z}{s_x} & 0 & 0 \\ 0 & \frac{s_z s_x}{s_y} & 0 \\ 0 & 0 & \frac{s_x s_y}{s_z} \end{bmatrix} = \operatorname{diag} \left(s_y s_z s_x^{-1}, s_z s_x s_y^{-1}, s_x s_y s_z^{-1} \right), \tag{C.15}$$

where $\tilde{s}_i = \kappa_i + \sigma_i / (\mathrm{j} \omega \varepsilon_0)$ in the frequency domain (note the integrating factor from the $1/(\mathrm{j}\omega)$ term). For ease of reading the following shorthand notation will be used

$$s_{i,j,k} \equiv \operatorname{diag} \left(s_i, s_j, s_k \right),$$

and likewise for $\kappa_{i,j,k}$ or $\sigma_{i,j,k}$. In this notation the original tensor can be written as $\underline{s} = s_{y,z,x} s_{z,x,y} s_{x,y,z}^{-1}$. Following the same procedure as before with the normal Maxwell

equations we arrive at the update equations for the FDTD method with UPML

$$\mathbf{b}^{i+1/2} = \frac{2\varepsilon_0\kappa_{y,z,x} - \Delta t\sigma_{y,z,x}}{2\varepsilon_0\kappa_{y,z,x} + \Delta t\sigma_{y,z,x}}\mathbf{b}^{i-1/2} - \frac{2\varepsilon_0}{2\varepsilon_0\kappa_{y,z,x} + \Delta t\sigma_{y,z,x}} \left[\Delta t \mathsf{D}_e \mathbf{e}^i + \mu_0(\mathbf{m}^{i+1/2} - \mathbf{m}^{i-1/2})\right] \tag{C.16}$$

$$\mathbf{h}^{i+1/2} = \frac{2\varepsilon_0\kappa_{z,x,y} - \Delta t\sigma_{z,x,y}}{2\varepsilon_0\kappa_{z,x,y} + \Delta t\sigma_{z,x,y}}\mathbf{h}^{i-1/2} + \frac{1}{\mu(2\varepsilon_0\kappa_{z,x,y} + \Delta t\sigma_{z,x,y})} \left[(2\varepsilon_0\kappa_{x,y,z} + \Delta t\sigma_{x,y,z})\mathbf{b}^{i+1/2} - (2\varepsilon_0\kappa_{x,y,z} - \Delta t\sigma_{x,y,z})\mathbf{b}^{i-1/2}\right] \tag{C.17}$$

$$\mathbf{p}^{i+1} = \frac{(2\varepsilon - \sigma\Delta t)}{(2\varepsilon + \sigma\Delta t)}\mathbf{p}^{i-1} + \frac{2\Delta t}{(2\varepsilon + \sigma\Delta t)}\mathsf{D}_h\mathbf{h}^{i+1/2}. \tag{C.18}$$

$$\mathbf{d}^{i+1} = \frac{2\varepsilon_0\kappa_{y,z,x} - \Delta t\sigma_{y,z,x}}{2\varepsilon_0\kappa_{y,z,x} + \Delta t\sigma_{y,z,x}}\mathbf{d}^{i} - \frac{2\varepsilon_0}{2\varepsilon_0\kappa_{y,z,x} + \Delta t\sigma_{y,z,x}}(\mathbf{p}^{i+1} - \mathbf{p}^{i}) \tag{C.19}$$

$$\mathbf{e}^{i+1} = \frac{2\varepsilon_0\kappa_{z,x,y} + \Delta t\sigma_{z,x,y}}{2\varepsilon_0\kappa_{z,x,y} + \Delta t\sigma_{z,x,y}}\mathbf{e}^{i} - \frac{1}{2\varepsilon_0\kappa_{z,x,y} + \Delta t\sigma_{z,x,y}} \left[(2\varepsilon_0\kappa_{x,y,z} + \Delta t\sigma_{x,y,z})\mathbf{d}^{i+1} - (2\varepsilon_0\kappa_{x,y,z} - \Delta t\sigma_{x,y,z})\mathbf{d}^{i}\right]. \tag{C.20}$$

Note that in this case we cannot get around substituting the constitutive relationships directly and simplifying the situation to just two fields (E and H) due to the added time derivatives from the constitutive tensor, we are even forced to introduce a new field $\boldsymbol{P}$ which is defined as

$$\boldsymbol{P} = s_{y,z,x}s_{z,x,y}s^{-1}_{x,y,z}\boldsymbol{E}. \tag{C.21}$$

C.3.1. Tensor Coefficients

To make the PML we have implemented in our simulation space actually attenuate the signal we add a loss (through the σ parameter). This loss has to be graded, and slowly increased throughout the PML space since a jump in conductivity would lead again to unwanted reflections. There are a number of different ways to do this grading but in this implementation the choice was made to use a polynomial grading

$$\sigma(\boldsymbol{r}) = \left(\frac{\boldsymbol{r}}{d}\right)^n \sigma_{\max}, \tag{C.22}$$

where d is the length of the PML in the direction $\boldsymbol{r}$ starting from $\boldsymbol{r} = 0$ at the start of the PML to $\boldsymbol{r} = d$ at the edge, $\sigma_{\max}$ is the maximum conductivity and n the order of the polynomial grading.

We do not use the permittive UPML coefficient since our PML always starts in free space around our object so there is no need to match it to the permittivity of this medium. For a polynomial grading the parameters can be estimated given an estimate of the acceptable error. This is done through specifying a maximum reflection coefficient of the layer specified as $R(0)$ the reflection on normal incidence.

It has been demonstrated that for a broad range of applications with a 10 cell thick polynomial graded PML the optimal reflection coefficient is $R(0) \approx \exp(-16)$ [3]. We

can use this value to determine our σ_{max} through

$$\sigma_{\text{max}} = -\frac{(n+1)\,R(0)}{2\eta d}, \tag{C.23}$$

with η the impedance of the PML ($\sqrt{\frac{\mu}{\varepsilon}}$), which is free space impedance for our scenario. Typically, values for the order n are chosen between 3 and 4, and we have found that 4 works very well for our simulations.

C

C.4. Computational Implementation

Here we describe the matrix structure of the update equations as they are implemented and normalised within the MATLAB programming language in which the FDTD code is written.

In our computation implementation the vectors are stacked field vectors in x-lexicographic fashion, and the matrices describe the action of the voxelwise scaling. The update equations then follow as

$$\mathbf{b}^{i+1/2} = \mathsf{N}_b \left(\mathsf{O}_b \mathbf{b}^{i-1/2}\right) - \mathsf{O}_b \left[\Delta t \mathsf{D}_e \mathbf{e}^i + \mu_0 \left(\mathbf{m}^{i+1/2} - \mathbf{m}^{i-1/2}\right)\right], \tag{C.24}$$

$$\mathbf{h}^{i+1/2} = \mathsf{N}_h \left(\mathsf{O}_h \mathbf{h}^{i-1/2}\right) + \mathsf{O}_h \left[\mathsf{M}_\mu^{-1} \left(\mathsf{L}_b \mathbf{b}^{i+1/2} - \mathsf{R}_b \mathbf{b}^{i-1/2}\right)\right], \tag{C.25}$$

$$\mathbf{p}^{i+1} = \mathsf{M}_\varepsilon^{-1} \left(\mathsf{M}_\varepsilon \mathbf{p}^i\right) - \left(\Delta t \mathsf{D}_h \mathbf{h}^{i+1/2} - \mathbf{j}^{i+1/2}\right), \tag{C.26}$$

$$\mathbf{d}^{i+1} = \mathsf{N}_d \left(\mathsf{O}_d \mathbf{d}^i\right) + \mathsf{O}_d \left(\mathsf{L}_p \mathbf{p}^i + 1 - \mathsf{R}_p \mathbf{p}^i\right), \tag{C.27}$$

$$\mathbf{e}^{i+1} = \mathsf{N}_e \left(\mathsf{O}_e \mathbf{e}^i\right) + \mathsf{O}_e \left(\mathsf{L}_d \mathbf{d}^i + 1 - \mathsf{R}_d \mathbf{d}^i\right), \tag{C.28}$$

where the matrices N, O are numerator and denominator of the fractions given in Equations (C.16) to (C.20), R and L also follow from these equations straightforward, and M, D, the medium and differencing matrices, as well as the normalisation procedure used can be found described in [4].

References

[1] Kane Yee. Numerical solution of initial boundary value problems involving Maxwell's equations in isotropic media. *IEEE Transactions on antennas and propagation*, 14(3):302–307, 1966.

[2] Allen Taflove and Susan C Hagness. *Computational electrodynamics: the finite-difference time-domain method*. Artech house, 2005.

[3] Stephen D Gedney and A Taflove. The perfectly matched layer absorbing medium. *Advances in Computational Electrodynamics: The Finite-Difference Time-Domain Method*, pages 263–344, 1998.

[4] Rob F. Remis. *Computational Electromagnetics Part 2, Finite-Difference Techniques*. Laboratory of Electromagnetic Research, Delft University of Technology, 2006.

D

Transceive Phase Correction

An assumption underlying the contrast source inversion (CSI) inversion methods [1] as well as most other electrical properties tomography (EPT) methods (such as the Helmholtz based magnetic resonance (MR)-EPT[2]) is the transceive phase assumption (TPA) assumption [3].

This assumption states that the receive phase (ϕ^-)—which cannot be measured directly—is equal to the transmit phase (ϕ^+). Then, the actually measured transceive phase, which is

$$\phi^\pm = \phi^+ + \phi^- \tag{D.1}$$

can be used to determine the transmit phase as

$$\phi^- = \frac{\phi^\pm}{2}. \tag{D.2}$$

Unfortunately, it turns out that—especially at high frequencies—this assumption does not hold [4]. Therefore, we propose an updated contrast source inversion scheme with added transcieve phase correction (TPC) updates.

D.1. Theory

To perform a phase correction we consider the measured $\tilde{B}_1^+$ field in polar form and rewrite it to include the measured transceive phase and a receive phase correction term as

$$\tilde{B}_1^+ = \left|\tilde{B}_1^+\right| e^{\mathrm{j}\phi^+} = \left|\tilde{B}_1^+\right| e^{\mathrm{j}\phi^\pm} e^{-\mathrm{j}\phi^-}. \tag{D.3}$$

Combining this with the original cost functional Equation (3.12) (more specifically the data residual Equation (3.9)) results in a new data residual

$$\tilde{r}_d^{\mathrm{TPC}}(\boldsymbol{x}) = \left|\tilde{B}_1^{+;sc}(\boldsymbol{x})\right| e^{\mathrm{j}\phi^\pm(\boldsymbol{x})} e^{-\mathrm{j}\hat{\phi}^-(\boldsymbol{x})} - \mathcal{G}_{\mathrm{data}}\{\hat{w}\}(\boldsymbol{x}) \quad \text{for} \quad \boldsymbol{x} \in \mathbb{D}_{\mathrm{body}}, \tag{D.4}$$

Published in:
Magnetic Resonance in Medicine
doi: arXiv:1907.13451
This work was performed together with Peter Stijnman as a master's student under supervision of Patrick Fuchs and Stefano Mandija (University Medical Center Utrecht).

where we have added a new approximant $\hat{\phi}^-$ to represent the estimated recieve phase. The rest of the notation is as presented in Chapter 3. To update this estimate during the regular CSI iterations a phase update step is added to the algorithm. In this step the receive phase is updated using the current estimates of the contrast and electric field strength.

We use the estimated contrast and electric field to compute a scattered receive field $\tilde{B}_1^{-;sc}$ by using the integral field equation Equation (3.2), and computing it in the same way as the $\tilde{B}_1^{+;sc}$ field but with changed sign between x and y components, as

$$\tilde{B}_1^{-;\mathrm{sc}}(\boldsymbol{x}) = \frac{\tilde{B}_x^{\mathrm{sc}} - \mathrm{j}\tilde{B}_y^{\mathrm{sc}}}{2} = \frac{1}{2} \int_{\boldsymbol{x}' \in \mathbb{D}_{\mathrm{body}}} \sum_{k=x,y,z} \left[\tilde{G}_{xk}^{\mathrm{BJ}}(\boldsymbol{x}, \boldsymbol{x}') - \mathrm{j}\tilde{G}_{yk}^{\mathrm{BJ}}(\boldsymbol{x}, \boldsymbol{x}') \right] \tilde{w}_k(\boldsymbol{x}') \, \mathrm{d}V. \quad \text{(D.5)}$$

D

Following the computation, the new estimate for the receive phase is the phase of this receive field.

Computationally this means there is an added fourier-type integral to be computed at each CSI iteration. This increases computation time and complexity, which is not a big issue for two-dimensional CSI-EPT, but may be prohibitive when dealing with fully three-dimensional fields. In those cases the phase update could be performed only every 10 or 100 iterations, since not including it would just result in the original scheme. However, no assumptions on the phase are necessary to reconstruct the contrast from the B_1^+ data. The new two-dimensional procedure is shown below in Algorithm 4.

D.2. Results

To check the improved algorithm and confirm that it can indeed correct the transcieve phase assumption two-dimensional validation simulations have been performed. Results from these experiments can be found on the next pages in Figures D.1 and D.2. From these reconstructions it can be seen that the transceive phase introduces a bigger error at higher frequencies, as already mentioned in the introduction. Additionally, our proposed algorithm seems to be able to correct for this assumption at both tested field strengths to the same degree, where only a minute phase error is present. This might be caused by phase wrapping errors where the phase is unwrapped along the wrong "branch" and contains phase jumps of approximately 2π which should not be present. There are different ways to approach phase unwrapping, which can be very robust in two dimensions, but in that case generalising to three dimensions is a more complicated.

In addition to these in-silico validations an in-vivo experiment was also performed using a spherical phantom. The full results for this can be found in [5].

References

[1] Reijer Leijsen, Patrick Fuchs, Wyger Brink, Andrew Webb, and Rob Remis. Developments in electrical-property tomography based on the contrast-source inversion method. *Journal of Imaging*, 5(2):25, 2019.

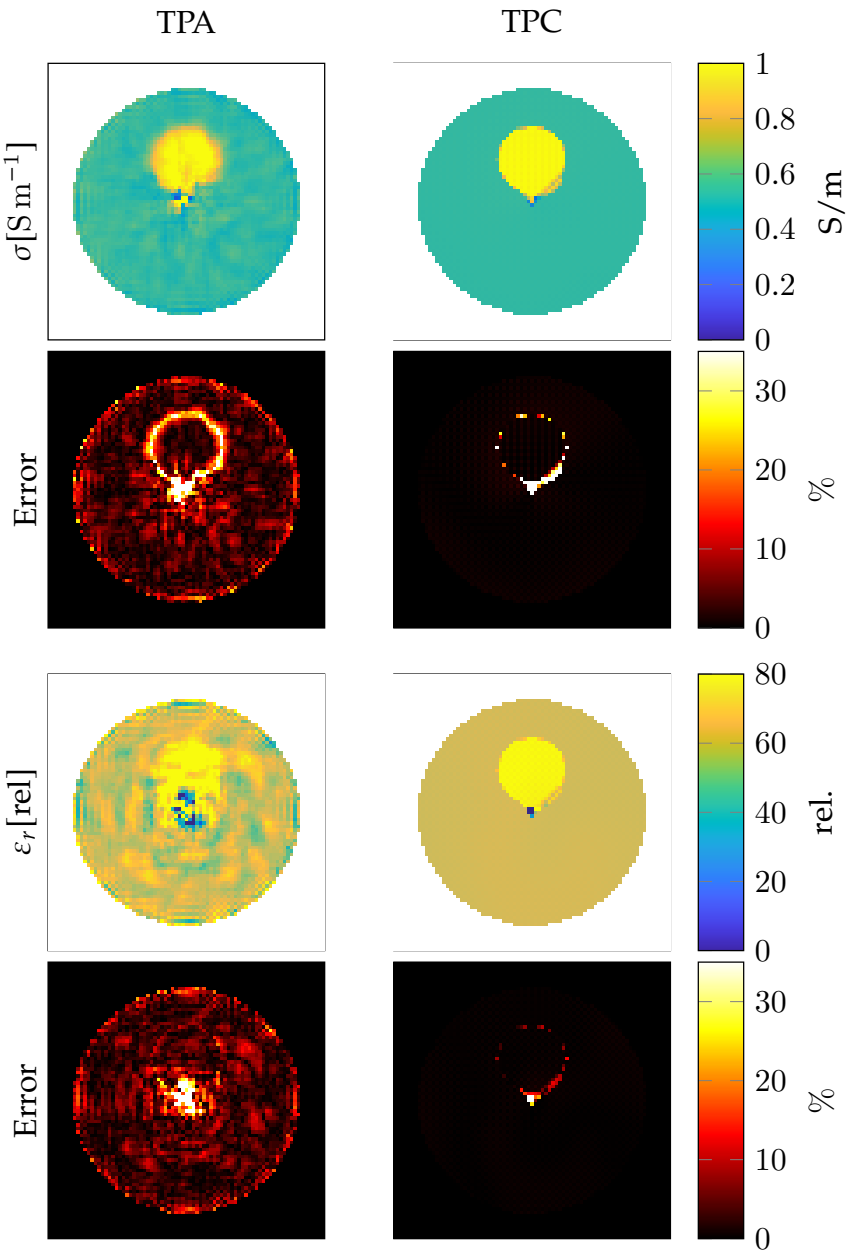

Figure D.1: Reconstruction results using transceive phase correction compared to the original CSI method in a 3 T background field scanner. Left the original method and right the transieve phase corrected results. Top is conductivity and bottom permittivity reconstructions.

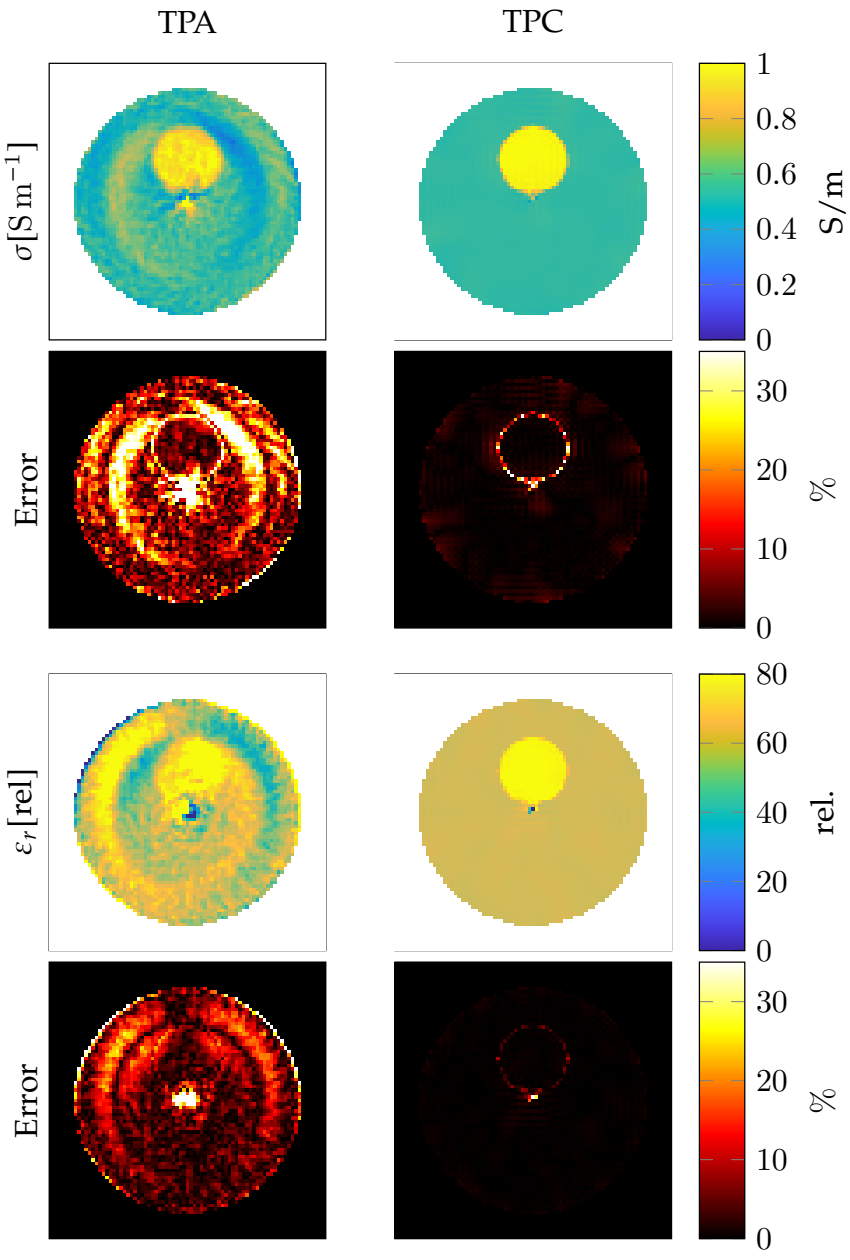

Figure D.2: Reconstruction results using transceive phase correction compared to the original CSI method in a 7 T background field scanner. Left the original method and right the transieve phase corrected results. Top is conductivity and bottom permittivity reconstructions.

Algorithm 4 Transceive phase corrected (2D) CSI-EPT.

- Compute $\hat{w}^{[0]}$, $\hat{\chi}^{[0]}$ and the incident RF-fields
- For $k = 1, 2, \ldots$
  1. Update the contrast sources according to
  $$\hat{w}^{[k]} = \hat{w}^{[k-1]} + \alpha^{[k]} \boldsymbol{v}^{[k]}.$$
  2. Compute the corresponding electric field strength $\hat{\boldsymbol{E}}^{[k]}$ according to (cf. Equation (3.6)).
  $$\hat{E}^{[k]} = \tilde{E}^{b} + \mathcal{G}_{\text{body}}\{\hat{w}^{[k]}\}.$$
  3. Knowing the contrast source and the corresponding electric field strength, determine the contrast using the constitutive relationship.
  4. Update the receive phase by computing the receive field from Equation (D.5) and updating the phase estimate as
  $$\hat{\phi}^{-} = \angle \hat{B}_1^{-;sc}.$$
  5. Stop if objective function is smaller than user specified tolerance level, or if maximum number of iterations has been reached.
- Return $\hat{\chi}^{[k]}$, $\hat{w}^{[k]}$, $\hat{B}_1^{-;sc}$, and $\hat{E}_z$.

[2] Jiaen Liu, Yicun Wang, Ulrich Katscher, and Bin He. Electrical properties tomography based on B_1 maps in MRI: Principles, applications, and challenges. *IEEE Transactions on Biomedical Engineering*, 64(11):2515–2530, 2017.

[3] Astrid LHMW Van Lier, David O Brunner, Klaas P Pruessmann, Dennis WJ Klomp, Peter R Luijten, Jan JW Lagendijk, and Cornelis AT van den Berg. B_1^+ phase mapping at 7 T and its application for in vivo electrical conductivity mapping. *Magnetic Resonance in Medicine*, 67(2):552–561, 2012.

[4] Astrid LHMW van Lier, Alexander Raaijmakers, Tobias Voigt, Jan JW Lagendijk, Peter R Luijten, Ulrich Katscher, and Cornelis AT van den Berg. Electrical properties tomography in the human brain at 1.5, 3, and 7T: a comparison study. *Magnetic resonance in medicine*, 71(1):354–363, 2014.

[5] Peter Stijnman, Stefano Mandija, Patrick Fuchs, Rob Remis, and Nico van den Berg. Transceive phase correced contrast source inversion-electrical properties tomography. In *International Society for Magnetic Resonance in Medicine 26th Annual Meeting and Exhibition (ISMRM18)*, page 5087, Paris (France), June 2018.

Acronyms

ACES international applied computational electromagnetics society.

AFI actual flip-angle imaging.

COSMOS calculation of susceptibility through multiple orientation sampling.

CSI contrast source inversion.

CT computerised tomography.

DFT discrete Fourier transformation.

EIT electrical impedance tomography.

EM electro magnetic.

EPT electrical properties tomography.

FANSI fast algorithm for nonlinear susceptibility inversion.

FDTD finite difference time domain.

FFT fast Fourier transformation.

FID free induced decay.

FoV field of view.

GMRES generalized minimal residual solver.

IEEE intitute of electrical and electronics engineers.

IISC Indian institute of science.

ISMRM International Society for Magnetic Resonance in Medicine.

ISTA iterative shrinkage- thresholding algorithm.

IT'IS foundation for research on information technologies in society.

LUMC Leiden university medical center.

MEDI morphology enabled dipole inversion.

MR magnetic resonance.

MRF magnetic resonance fingerprinting.

MRI magnetic resonance imaging.

MR-STAT magnetic resonance spin tomography in time-domain.

NMR nuclear magnetic resonance.

NWO Dutch research council.

PML perfectly matched layer.

QSM quantitative susceptibility mapping.

RF radio frequency.

ROI region of interest.

SAR specific absorption rate.

SE spin echo.

SNR signal to noise ratio.

STAR streaking artefact reduction.

STI susceptibility tensor imaging.

TE echo time.

TKD thresholded k-space division.

TPA transceive phase assumption.

TPC transcieve phase correction.

TR repetition time.

TSE turbo spin echo.

TU Delft Delft university of technology.

UHF ultra high field.

UISNR ultimate intrinsic signal to noise ratio.

UPML uniaxial perfectly matched layer.

VaNDI variational networks dipole inversion.

Notation

Symbol	Description	Unit
$\lvert\cdot\rvert$	absolute value	
B	the magnetic flux density	$\frac{\mathsf{V\,s}}{\mathsf{A\,m^2}} = \mathsf{T}$
B_0	background magnetic flux density (often referred to as field strength) of an MRI scanner	T
B_1^+	right rotating transmit magnetic field strength (defined as $\left(B_x + \mathrm{j}B_y\right)/2$)	T
I_ν	modified Bessel function of the first kind and order ν	
K_ν	modified Bessel function of the second kind and order ν	
$H_\nu^{(k)}$	Hankel function of the k-th kind and order ν	
c_0	lightspeed	$\frac{\mathsf{m}}{\mathsf{s}}$
χ	contrast function	
s	complex frequency	$\frac{1}{\mathsf{s}}$
$\cdot^*$	complex conjugation	
D	the electric displacement field	$\frac{\mathsf{C}}{\mathsf{m^2}} = \frac{\mathsf{A\,s}}{\mathsf{m^2}}$
∂_i	partial derivative along the i dimension	$\frac{1}{\mathsf{s}}$
U	capital sans serif—discrete matrix	
u	sans serif—discretised quantity	
E	the electric field	$\frac{\mathsf{V}}{\mathsf{m}}$
ε_0	vacuum permittivity	$\frac{\mathsf{F}}{\mathsf{m}}$
ε_r	relative permittivity	rel.
f	frequency	$\frac{1}{\mathsf{s}}$
γ_0	propagation coefficient of free space	
γ	proton gyromagnetic ratio ($2.675\,19 \times 10^8$)	$\frac{1}{\mathsf{s\,T}}$
H	the magnetic field	$\frac{\mathsf{A}}{\mathsf{m}}$

Symbol	Description	Unit
j	imaginary unit ($\sqrt{-1}$)	
Im	imaginary part	
Re	real part	
J	current density	$\frac{\mathrm{A}}{\mathrm{m}^2}$
K	magnetic current density	$\frac{\mathrm{V}}{\mathrm{m}^2}$
k_0	wavenumber of vacuum	$\frac{1}{\mathrm{m}}$
M	magnetisation	$\frac{\mathrm{A}}{\mathrm{m}}$
μ_0	vacuum permeability	$\frac{\mathrm{V\,s}}{\mathrm{m\,A}}$
μ_r	relative permeability	rel.
$\|\cdot\|$	ℓ_2 norm	
ω	(angular) frequency	$\frac{\mathrm{rad}}{\mathrm{s}}$
$\boldsymbol{\rho}$	position vector in two-dimensions	m
$\boldsymbol{x}$	position vector in three-dimensions	m
σ	conductivity	$\frac{\mathrm{V}}{\mathrm{m}}$
t	time	s
$\underline{\boldsymbol{u}}$	bold underline—tensor	
$\tilde{\cdot}$	Fourier domain quantity	
$\hat{\cdot}$	Laplace domain quantity	
$\hat{\boldsymbol{\imath}}$	unit vector	
$\boldsymbol{u}$	bold—vector quantity	
$\cdot_{x,y,z,\phi}$	subscript—component of a vector in the x, y, z, ϕ dimension respectively	
$\boldsymbol{A}$	vector potential	A or A s

Acknowledgements

Four years of hard work by oneself are enough to get a lot of things done, but not enough for the work you are holding in your hands. Therefore, it is my great pleasure to spend this last chapter thanking all the people that have helped make it possible, and those that have made my time in Delft a memorable and happy experience.

First off all I want to thank the backbone of our group, Antoon Frehe, who always made sure the problem wasn't my hardware but rather between the keyboard and the chair (unfortunately), even going so far as to installing packages on the server during the weekend (from his comfortable chair during a game of chess I hope). And of course all various the secretaries that have supported my travels and logistics at the faculty, Minaksie, Irma, and Brigitte, it would certainly have been a lot bigger hassle to finish this without you.

The rest of the floor, so many brilliant interesting and funny people, and such great memories. Barbecues, eating out, playing boardgames, visiting concerts, and most of all our profound coffee conversations. Some of you have moved away already, others have joined in the meantime, changing the subjects but never the tone of conversation, always keeping an open mind and open ear to others' research and cultural background. Alberto, Andreas, Aybüke, Aydin, Bahareh, David, Elvin, Feiyu, Fernando, Hanie, Jac, Jamal, Jiani, Jie, Manuel, Mario, Matt, Metin, Miao, Pim, Shahrzad, Sundeep, Tarik, Tom, Tuomas, Venkat, Wangyang, I cannot thank you all enough for making these the most memorable years of my life (so far), and I hope I can keep in touch as I move away!

Alle-Jan and Geert, thank you very much for your guidance, always having time for a short chat and keeping a critical outlook on all the physics I was doing and trying to point me back at signal processing whenever appropriate!

Of course, I have to mention my collaborators, who have directly contributed to most of this work through discussions, simulations, ideas, feedback, and motivation. Andrew, Bart, Nico, Peter, Reijer, Tom, Stefano, Ruud, and Wyger, thanks!

All my colleagues (and friends) from Leiden, thank you so much for accepting me and allowing me to be a part of your community especially during our annual ISMRM meetings but also my many visits to the LUMC. Not just Leiden, but also Bangalore has played an integral part in my development these last few years. Thank you Shubham for showing me around the IISC and especially for the snacks on arrival, they were always greatly appreciated. Also many thanks for making this collaboration possible, allowing me to work in and with your lab and being introduced to so many great researchers at the institute prof. Hari it was my pleasure!

My office mates Jeroen and Jörn deserve special mention, showing me the ropes, and giving me a flying start to my PhD. It's been a great pleasure to photoshop you guys and I really appreciate all the tips and discussions we've had both in and outside of the office, even though you never did explain to me how to get that iPad ;-).

Without music my life would have been a lot more mundane, and often when I felt frustrated with a problem I could find refuge in the many rehearsals, concerts and

performances that I have been fortunate to participate in. Everyone from Krashna, Ricciotti, RSO, Nesko, NSJO, Sorrindo, and Vocalzz, thank you so much for adorning (opluisteren) my time in Delft! In particular the “Eetclub”, in the words of Reinhard Mey I would like to thank you “Für den Platz an eurem Tisch, für jedes Glas, das ich trank / Für den Teller, den ihr mit zu den euren stellt / Als sei selbstverständlicher nichts auf der Welt”. Many a hard working day was finished with a shared dinner and rehearsal and of course many laughs!

Sarafina, as cliched as this may sound, you have been part of the foundation for this work, and one of the reasons I didn't outright quit when things got tough, or I didn't see the point of my research anymore. You inspire me to be more disciplined, and I am always awed by the diligent hours of practice you manage to put up with before getting tired. You've always listened to me with great interest even though most of the time I would drone on about some specifics in a simulation code without any context, so I'm very glad you stuck with me and know that this book is shaped by your input almost as much as mine.

Last, but certainly not least, Rob, thank you so much for the last 5 years, already during my masters' but more so since I started my PhD you have shown me what it means to be researcher and guided me into becoming one, I know no one that holds themselves to higher standards when it comes to academic integrity and fairness than you and it has certainly inspired me to strive for transparency, reproducability and honesty in my work. I am glad you sometimes protected me from my own eagerness to take on helping out in education during my first couple of years, so I didn't get caught up in grading tests while my research would have suffered, I've been more than able to catch up on that during my last years.

I have tried mentioning all those that have had a direct impact on this work and my progress over the last four years, but I am sure I have missed some. Even though I know I would it still felt better to mention those that I could come up with than leave this chapter out altogether, if you feel like you should have been in this list but are not I would like to propose a “Wiedergutmachungsschnitzel” and will buy you a beer if you drop me a line!

Curriculum Vitæ

Patrick Stefan Fuchs was born on top of a particle accelerator in the picturesque Meyrin on the 18th of May 1991. After moving to the Netherlands he finished his high school at the Rijnlands Lyceum in Oegstgeest in 2008, which was followed up by electrical engineering at the Delft University of Technology. Here he finished bachelor's in 2014 and master's degree in 2016 (cum laude). This paved the way for a PhD with Rob Remis (also his thesis advisor in the master) on signal processing and electromagnetics in MRI as part of a collaboration with the Indian Institute of Science and professor KVS Hari.

During his PhD he has spent two trimesters in India as part of this collaboration working with the statistical signal processing group of KVS Hari on signal processing methods in MRI diagnostics. In Delft, he has helped with the electromagnetics course in the Bachelors and collaborated with the Leiden University Medical Center on the low field project in various capacities.

In Delft Patrick has been very active in various associations. Besides numerous committees in his study and music associations he has been part of several student boards. He was the treasurer of the Electrotechnische Studievereeniging, Chair and vice-chair of the IEEE Student Chapter and commissary external relationships for SIAM student chapter. In the MRI community he has helped organise the ISMRM Benelux Conference of January 2020 in the role of sponsorship coordinator.

He is an avid amateur musician and profiently plays the cello and double bass in various ensembles, orchestras, and a Brazilian jazz band. In this capacity he has also joined the Dutch student chamber orchestra, the Dutch student jazz orchestra and the Ricciotti ensemble.

Magnetic resonance imaging (MRI) is a very versatile and powerful medical imaging and diagnostics tool. As the limits of the hardware are stretched with new developments the underlying models and imaging modalities are challenged. In this work quantitative imaging approaches using electrical properties are described, which use the unique knowledge we have on the electromagnetic fields in MRI to simplify the reconstruction and imaging algorithms.

Also, as field strengths increase there are more and more reasons to challenge the quasi-static field assumption used in the conventional signal model. Here we start from first principles and work our way up to a comprehensive signal model which gives great insights especially into the influence of electrical properties on a measurement as well as the deep connection between measurement (or antenna) type and coupling of the fields.